Current advances on nanostructured oxide photoelectrocatalysts for water splitting: A comprehensive review

Mohamed El Ouardi, Ayoub El Idrissi, Hassan Ait Ahsaine, Amal Baqais, Mohamed Saadi, Madjid Arab

Surfaces and Interfaces xxx (xxxx) 103850

Contents lists available at ScienceDirect

Surfaces and Interfaces

journal homepage: www.elsevier.com/locate/surfin

Current advances on nanostructured oxide photoelectrocatalysts for water splitting: A comprehensive review

M. El ouardi [a, b], A.El Idrissi [c], H.Ait Ahsaine [a, *], A. BaQais [d], M. Saadi [a], M. Arab [b, *]

[a] Laboratoire de Chimie Appliquée des Matériaux, Faculty of Sciences, Mohammed V University in Rabat, Morocco
[b] Université de Toulon, Aix Marseille Univ, CNRS, IM2NP, CS 60584, CEDEX 9, F-83041 Toulon, France
[c] Laboratory of Materials, Catalysis & Natural Resources Valorization, URAC 24, Faculty of Science and 9 Technology, Hassan II University, B.P. 146, Casablanca, Morocco
[d] Department of Chemistry, College of Science, Princess Nourah Bint Abdulrahman University, P.O. Box 84428, Riyadh 11671, Saudi Arabia

ARTICLE INFO

Keywords:
Water splitting
Hydrogen evolution reaction
Oxide electrocataysts
Electrocatalysis

ABSTRACT

Due to increasing environmental pollution and rising energy demand, the need for clean energy is increasingly urgent. As an example of sustainable and clean energy, hydrogen (H_2) has received a lot of interest in the last few years. Photoelectrochemical water splitting (PEC) represents one of the most advanced and promising technologies for generating hydrogen in an easy, inexpensive and durable way. The development and fabrication of metal oxides-based photocathodes and photoanodes have attracted a great interest for photoelectrochemical water splitting owing to their numerous benefits including enhanced light absorption capacity, outstanding photoelectrochemical stability, greater charge separation efficiencies, low cost. Over the last decades there have been considerable processes carried out to develop metal oxides for PEC water splitting. This review summarizes some of the recent progress in the use of metal oxides (Fe_2O_3, ZnO, CuO, Co_3O_4) as photoelectrodes for PEC water splitting, as well as strategies to improve their photoelectrocatalytic performances like morphological engineering, heterojunctions and doping techniques.

1. Introduction

The reduction in non-renewable resources like oil, coal and natural gas coupled with the imperative for a cleaner environment, underscores the pressing need for viable alternative and renewable energy sources for power generation [1–5]. Hydrogen is increasingly recognised as a promising replacement for fossil fuels in the future energy system. This is driven by its incredible energy density, its environmentally friendly and non-toxic properties, and its capability to be derived from a variety of renewable sources. [6–8]. Water splitting to produce hydrogen is an environmentally sustainable process that provides a carbon-free fuel and represents an attractive way to chemically store renewable energy [9–13]. From this point of view, hydrogen may be considered as the fuel of the next generation, capable of storing and transporting the natural (chemical) form of renewable energy. This technology may also contribute to solving the issue of global warming caused by the existence of greenhouse gases (CH_4, CO_2 and CO) [14–17]. Several methods have been used to achieve this goal to split the water molecule and generate hydrogen (H_2) and oxygen (O_2) such as photoelectrochemical (PEC) [18–21], photocatalytic [22–25], photobiological [26,27] and thermal decomposition [28,29]. Efficient and ecofriendly, simplest and clean technology for the generation of hydrogen are photoelectrochemical and photocatalytic water splitting [30–33]. In the last few years, there have been a number of semiconductors designed to be catalytically effective in photochemical reactions; these catalysts have to meet three key conditions for an efficient water splitting reaction. (1) appropriate band-edge potentials for water splitting reaction, (2) outstanding stability to the photochemical reaction and (3) appropriate band gap. Cleavage of pure water into hydrogen and oxygen in the presence of catalysts and under visible light is a highly appealing option for collecting solar energy as chemical energy. the Gibbs free energy of the water cleavage reaction (Eq (1)) is ($\Delta G^0 = 238$ kJ/mol) [34].

$$2\,H_2O \rightarrow 2H_2 + O_2 \quad (1)$$

The worldwide demand for hydrogen is satisfied by natural gas steam reforming with a percentage of 50 %, this technique is the most frequently used, resulting in the emission of greenhouse gases, 30 % from oil reforming, 18 % by coal gasification, 3.9 % through water electrolysis and 0.1 % from other sources [35]. To avoid the harmful consequences of fossil fuel burning on the atmosphere, as well as on human health, hydrogen must be generated using clean and renewable en-

* Corresponding authors.
E-mail addresses: h.aitahsaine@um5r.ac.ma (H.Ait Ahsaine), madjid.arab@univ-tln.fr (M. Arab).

https://doi.org/10.1016/j.surfin.2024.103850
Received 17 November 2023; Received in revised form 28 December 2023; Accepted 3 January 2024
2468-0230/

ergy sources in an environmentally friendly manner [36]. Due to its considerable and unlimited supply, solar energy is viewed as a valuable alternative energy source. The solar energy can supply about 173,000 TW in one year, which is about 9600 times more than the value of the annual world energy consumption (18.39 TW in 2018) [36]. At this stage solar energy can be used in several processes, such as solar thermal power plants, solar fuels and solar cells [37]. Generally, generation of hydrogen based on solar energy may be categorized into four main classes [37,38]. These are photovoltaic energy, solar thermal energy, photo-electrolysis and biophotolysis [37]. Photovoltaics, photoelectrolysis and biophotolysis are characterized by their usage in applications at low temperatures, whereas solar thermal may be employed in both low- and high-temperature applications [37,39,40]. Thermolysis, thermochemical cycles, gasification, reforming and cracking are applications that require the use of concentrated solar energy, the latter is used directly to generate electricity to power electrolysis and produce hydrogen [37]. The main ways to produce solar hydrogen are shown in Fig. 1. Photoelectrochemical (PEC) water splitting is considered to be an ideal method, it represents an environmentally friendly and sustainable process, moreover it is able to convert solar energy into chemical energy to oxidize or reduce substances to produce useful materials, of which hydrogen is one [41–43]. The splitting of water leads to the generation of hydrogen and oxygen, which are characterized by their stability and safety. Besides, hydrogen has a significantly greater energy density (141.9 MJ/kg) than conventional fossil fuels (55.5 MJ/kg for methane; 47.5 MJ/kg for gasoline; 20.0 MJ/kg for methanol) [44], and for the oxygen evolution reaction OER, it is stated that the produced during water splitting is required for environmental applications, in particular the decomposition of organic contaminants contained in polluted [45].

Due to their characteristics metal oxides and especially transition metal oxides have a high water splitting potential on account of their properties such as a suitable band gap for better incident light absorption, a low charge carrier recombination rate, a great chemical, thermal stability [46–48]. At this stage, the absorption of visible light is the main question asked, as most metal oxides have bandwidths that are too wide (>3 eV); this is the major drawback of these oxides which would consequently limit the oxidation performance of water among these oxides, TiO_2, Al_2O_3 and $SrTiO_3$, have a bandwidth greater than 3ev [49–52]. Generally, oxide-based semiconductors possess valence and conduction bands composed of O2p and transition metal character (d and f) respectively [49,53]. This wide distribution of the band gap due to the highly ionic character of O 2p and the orbital metal s leads to a decrease in the overlap of the orbits, this decrease is due to the large difference in electronegativity between the atoms as well as the difference in energy between the orbits of adjacent atoms, as an example ZnO (3.4 eV), Ga_2O_3 (4.5 eV) and Al_2O_3 (8.8 eV) [49]. In order to have a better absorption of visible light it is recommended to use semiconductors comprising transition metal cations having electronic configurations d^n as example WO_3 (~2.5 eV), Fe_2O_3 (~2.0 eV), Co_3O_4 (~1.3 eV) and Cu_2O (2.1 eV) [49,54]. Semiconductors containing post-transition metal cations remain an acceptable choice because they occupied s states with high bond energy, resulting in a smaller metal p-band gap O 2p, for example, PbO (2.1 eV.), SnO (2.4 eV), and Bi_2O_3 (2.5 eV). Fig. 2 depicts the distribution of band edge positions as well as the band gap from certain metal oxides which have drawn much interest during the last decade [55–58]. For effective usage of metal oxides as photoelectrode for PEC devices, both the valence band edge position or conduction band edge energy must astride on oxidation potential of water or redox potential of water respectively [55]. The positions of the band edges influence the effective separation of charge carriers (electrons and holes) generated by the absorption of light. On the other hand, the energy difference between the Fermi level (reference energy for the electrodes) and the band edges determines the photoactivation potential available for the reaction [59]. Sufficient energy is required to overcome the redox potentials of water [1,60]. In addition, an efficient photoelectrode for hydrogen production should have the valence and conduction band edges aligned to provide sufficient voltage for water reduction while promoting water oxidation [61]. This enables efficient charge separation and the production of H_2 from water. It is important to note that understanding these principles requires specific experimental data on the photoelectrochemical material under consideration. The electronic characteristics of the material, such as band energy levels, can be determined experimentally using techniques such as photoelectron spectroscopy (XPS). By understanding the positions of the strip edges, researchers can judiciously choose materials for the various components of the photoelectrochemical cell in order to optimise the overall efficiency of the system. In summary, determining the positions of the band edges in the photoelectrochemical water splitting reaction is essential for designing high-performance photoelectrochemical materials, maximising the efficiency of converting solar energy into hydrogen,

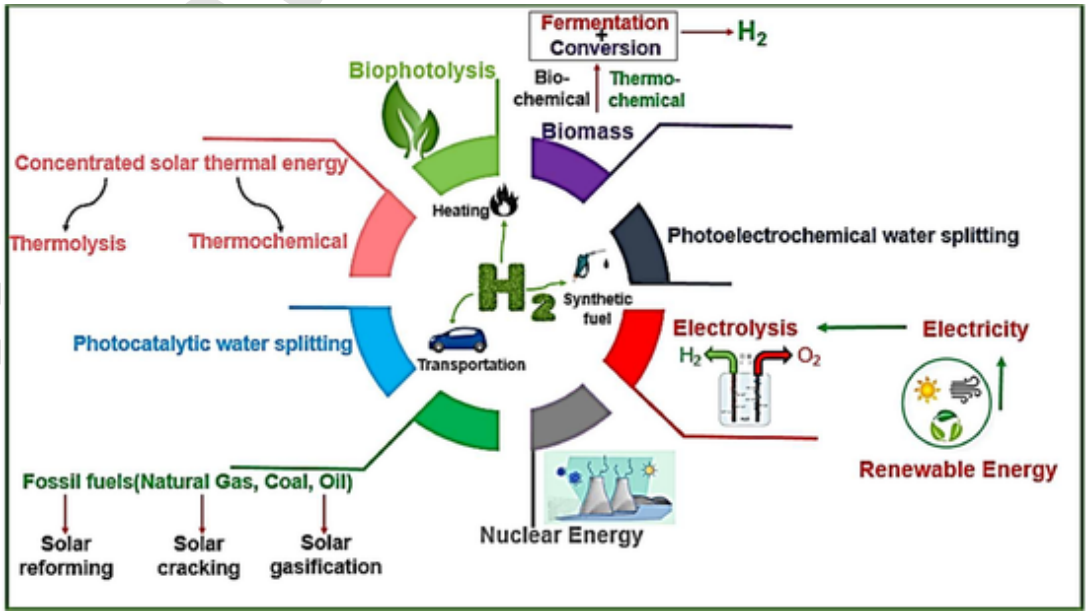

Fig. 1. The main ways to produce solar hydrogen.

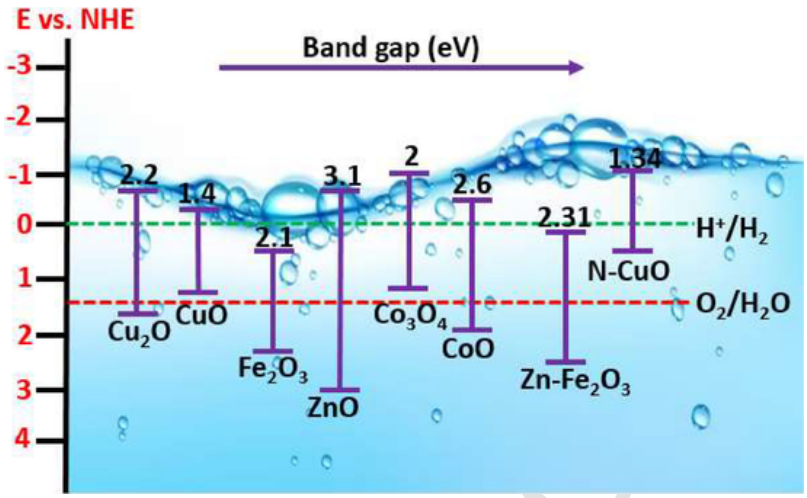

Fig.2. : Representation of the electronic states at the edges of the bands of various metal oxides. Reproduced from [55]. Copyright 2009 Royal Society of Chemistry.

and optimising the stability and durability of photoelectrochemical cells.

The importance of oxides is obvious from the increasing number of publications on oxides related to PEC water splitting applications as shown in Fig. 3. The journal papers that were used for bibliometric analyses have been collected by using a query search consisting of keywords through Web of Science database between 2010 and 2023.

So far, research has resulted in solar to hydrogen (STH) conversion efficacy in excess of 10 % using tandem PEC/photovoltaic (PV) and PEC cells using III-V light absorbers. For the PEC cell, the conversion efficiency is approximately 13.1 %, while for the PEC/photovoltaic (PV) cell it has reached 19.3 % [62,63]. On the other hand, III-V semiconductor materials have limitations: first of all, the manufacturing price is high and they are difficult to be scaled [64]. This opens the door to metal oxide based semiconductors which are characterized by low cost, excellent chemical stability and a wide distribution of bandgaps and edge positions [53]. By 2030 Energy consumption is anticipated to accelerate dramatically worldwide, due to rapid population growth and human development [30]. It is therefore necessary to develop sustainable alternative technologies that will cover the considerable shortfall caused by fossil fuels. Thus, in this review, we have focused on recent progress, concerning the production of fuel oil of the future which is Hydrogen, more specifically examines the water splitting by photoelectrochemical process from oxides based on (Fe, Cu, Co and Zn).

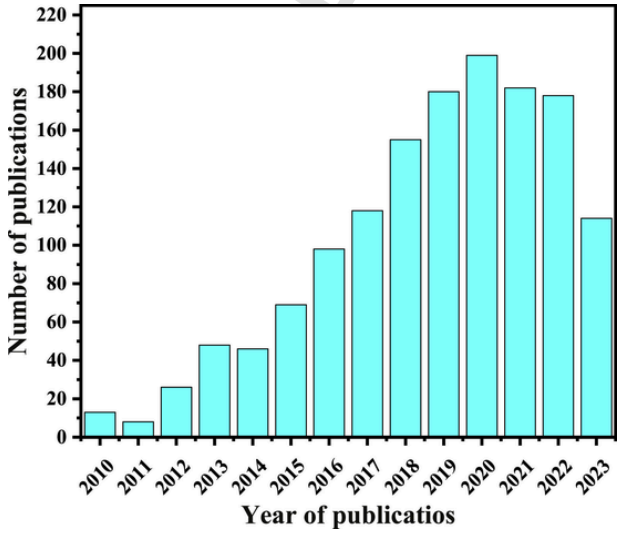

Fig. 3. Number of publications on oxides materials with the field of PEC water splitting from the journal Energy, Elsevier, source: Web of Science.

2. Metal oxide for photoelectrochemical (PEC) water splitting

2.1. Co-catalysts for water splitting

A large variety of noble metals including Pt [65], Pd [66], Ag [67], and Au [68] have been investigated. From these, Pt is the most preferred co-catalyst owing to its large work role and low overpotential for reducing protons to H_2 [69]. The incorporation of co-catalysts on semiconductors is a highly attractive way of accelerating the transport and charge separation of photo-excited electron-hole charges, inhibiting charge recombination and enhancing the photocatalytic and photoelectrocatalytic activity of solar water splitting [70,71]. Hong et al. [65] described that the H_2 evolution efficiency was improved by adding a Pt co-catalyst to a chestnut shell-like ZnO material. Photocurrent densities markedly increased with Pt contents, indicating that large quantities of active surface sites are conducive to photo-excited separation and charge transfer. A low-cost $NiFeO_x$ co-catalyst was coated onto the surface of the hematite (Fe_2O_3) photo-anode and examined as a surface catalytic promoter to enhance the kinetics of the OER reaction, as this reaction is the rate-controlling part of the whole process. The Ni-Fe oxide proved to be the most viable co-catalyst for oxygen evolution in the anionic medium in terms of improved PEC photocurrent and efficacy. The inclusion of $NiFeO_x$ in the hematite photo-anode improved the efficiency of the low-cost PECs in comparison with $IrRuO_x$ and ($La_{0.6}Sr_{0.4}Fe_{0.8}CoO_3$)LSFCO [72]. In other work, an efficient hematite decorated with $NiMnO_3$ co-catalyst photo-anode was studied for the first time using a simple two-step hydrothermal process. The inter-linked dynamic concurrence of various valence states of Mn and Ni in $NiMnO_3$, induced by the introduction of Ni into the Mn—O catalyst, promotes the photo-induced charge transfer in the hematite surface. This is the main reason why $NiMnO_3$—Fe_2O_3 exhibit higher photocurrent density than Fe_2O_3/MnO_2 and Fe_2O_3 [73] The synergistic catalytic action of Co_3O_4 as co-catalysts and carbon nanodots to improve the PEC water oxidation efficiency of the α-Fe_2O_3 photo-anode was reported by Zhang et al. [74] Wang et al. [75] have shown that the efficiency of CuO/Cu_2O may be significantly improved by incorporating a Pt co-catalyst layer. More excitingly, the stability of CuO with the Cu_2O and Pt co-catalyst displays only a 20 % decrease under irradiation for 3600 s, also the photocurrent density of $Cu_2O/CuO/Pt$ hybrids was 4.6 fold greater than native Cu_2O [75]. In another publication, NiO_x was investigated as a co-catalyst with FTO/CuO, the creation of a thin layer of NiO_x on CuO was advantageous for the

activity of PEC water splitting. The best NiO_x/CuO film showed a photocurrent density of −1.02 mA cm^{-2} at 0 V vs. RHE, that was superior to that of CuO (−.92 mA cm^{-2}). They have demonstrated that the visible light absorption by CuO results in the creation of electron-hole pairs. A proportion of the photo-generated electrons are captured by the oxyhydroxides contained in the NiO_x layer, reducing to metallic Ni and serving as a catalyst for the hydrogen evolution reaction [76]. Liu et al. [77] indicated that the Pt underlayer acts as an electron trapping layer to capture electrons from $CuWO_4$ to promote water reduction, whereas the p-type Co_3O_4 on $CuWO_4$ not only forms a p-n heterojunction, decreasing charge recombination at the Co_3O_4/$CuWO_4$ interface, but also that Co_3O_4 may be applied as a co-catalyst to enhance surface water oxidation [77]. Yu and his team [78] have found that the aligned and consistent energy band positions in the hierarchical Co_3O_4/P-C_3N_4/TiO_2 photo-anode facilitate the photoinduced holes to quickly diffuse from the 1-D TiO_2/P-C_3N_4 structure to the surface of the Co_3O_4 nanodots, whereas the produced electrons move from the photo-electrode to the counter electrode [78]. Recently, a novel hybrid ZnO/$Ti_3C_2T_X$ photo-anode has been prepared via facile spin coating of precipitated $Ti_3C_2T_X$ on the surface of ZnO as a co-catalyst for improved PEC water splitting. The $Ti_3C_2T_X$/ZnO photo-anode exhibited a photoconversion efficacy of 0.32 % and kept a stable photocurrent for more than 2000s. This improvement was explained by the presence of $Ti_3C_2T_X$, which acted as a co-catalyst able to facilitate charge transfer and enhance reaction kinetics in the ZnO/$Ti_3C_2T_X$ photo-anode [79]. The incorporation of co-catalysts in the field of photoelectrolysis of water is a commonly used strategy to enhance the overall efficiency of the process by assisting the oxidation and reduction reactions necessary for hydrogen production. But incorporating co-catalysts can also pose challenges and barriers such as the co-catalysts should be chemically compatible with the photoelectrochemical semiconductors, some co-catalysts may be long-term unstable, in particular when subjected to photo-electrolysis environments, resulting in a decrease in catalytic activity over time. This makes long-term stability a key issue for the durability of PEC devices and determining the optimal level of co-catalysts is a difficult challenge. Excessive levels may result in adverse impacts, whereas insufficient levels may not lead to meaningful enhancements in the PEC reaction. Finally, some co-catalysts may be expensive like Pt and Au resulting in economic implications for large-scale application. The following section of this review will report on Hematite, copper, cobalt and Zinc catalysts and the strategies used in using these materials.

2.2. Hematite-based photo-electrocatalysts

2.2.1. Morphological handling

The need to develop a cost-effective approach to increasing the efficiency of solar hydrogen conversion is a fundamental aspect of our research into renewable and sustainable energy sources. To achieve the US Department of energy's device efficacy goal of over 10 %, a new approach is needed to develop efficient and stable photocatalyst that work under solar irradiation [80]. One of the basic issues to be tackled in semiconductor is the dynamics of the photogenerated charges that perform the useful work in a regime where, in most cases, very rapid recombination is a dominant factor. It is understood that nanostructuring is a critical attribute of every catalytic material, but careful adjustment of the morphology, whether via texturing@1D alignment (for light harvesting), facet design and lowering the surface modification or raising the bulk porosity are just a number of steps which can significantly boost the performance of a superior water-splitting photoelectrode.

Owing to their natural abundance, low price and excellent chemical and photochemical stability in oxidative mediums and with a tight band gap (1.9–2.2 eV) that may theoretically absorb 40 % of the photons of the solar spectrum, hematite (n-type semiconductor) based photoanodes were regarded as one of the leading photoelectric materials for PEC water splitting [81,82]. Like conventional water electrolysis, reduction (H_2 evolution) occurs at the cathode, oxidation (O_2 evolution) occurs at the anode and an aqueous electrolyte closes the current circuit between the electrodes and an external circuit. One or both of the electrodes may be a photoactive material forming a space charge (depletion) layer at liquid junction (SCLJ)/semiconductor. During illumination, the photo-induced charges (e^-, h^+) are separated through the space charge field and the minority charges (holes for an n-type photoanode and electrons for a p-type photocathode) move to the SCLJ to perform one half of the water splitting reaction. A schematic of an n-type photo-anode (Fe_2O_3) is given in Fig. 4. The benefit of the PEC process is that it enables the separate generation and therefore collection of O_2 and H_2 [83].

Despite this, hematite has a fairly low PEC efficiency as a result of these severe disadvantages including low electrical conductivity, slow kinetics of oxygen evolution on the surface, short hole diffusion length (2–4 nm) and weak absorption coefficient as well as bad mobility of minority charges, leading to a substantial recombination of the global charge [49]. To bridge these clear boundaries to upgrade the PEC performance of hematite-based photoanodes for water splitting, a number of works have been carried out on the nanostructuring of hematite-based photoanodes, this strategy has shown efficient and robust results regarding the photoelectrochemical splitting of water [84–86]. By way of example, one-dimensional (1D) materials such as nanowires and nanorods are commonly employed effectively given their dimensions, which are similar to the carrier scattering lengths [82,87]. Likewise, ultrafine (~10 nm) hematite nanowires arrays have been fabricated on fluorine-doped tin oxide substrates (Fig. 5**a**), and they revealed higher photocurrents and charge separation efficiencies than the nanorods electrode this is due to the reduced charge transfer distance owing to the 1D nanowire structure [88]. It has been reported that α-Fe_2O_3 nanoflowers synthesized by aerosol assisted chemical vapor deposition (AACVD) (Fig. 5**b**) exhibit higher catalytic activity due to the large surface area and high light absorption [89]. Wang et al. [90], have prepared α-Fe_2O_3 nanoflakes (NFs) (Fig. 5**c**) for PEC water splitting. The as-cultured arrays of α-Fe_2O_3 NFs presented a water oxidation starting potential of 0.6 V versus RHE, and the attained photocurrent density was 0.8 mA/cm² at 1.23 V. Mao et al. [91], demonstrated that the hematite nanotubes displayed considerably better photoelectrochemical performance in comparison to the hematite nanorods, which in-

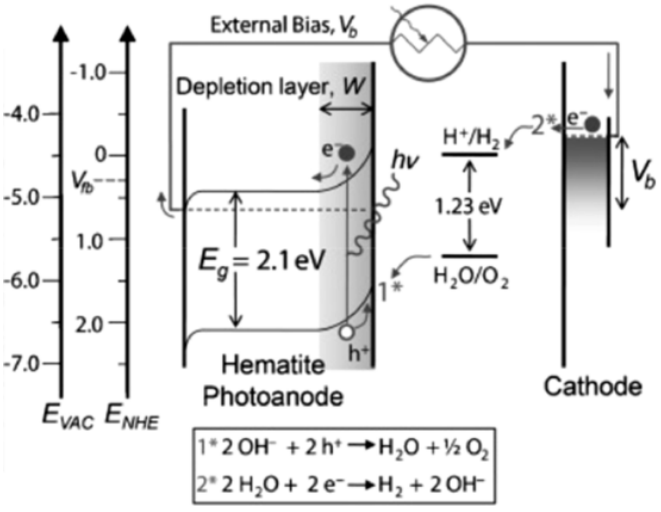

Fig. 4. Energy scheme for photo-electrochemical water splitting using an n-type photo-anode (hematite) for the oxygen evolution reaction and a cathode for the hydrogen evolution reaction. The flat band potential V_{fb}, bandgap E_g and the applied bias V_b are given. Reproduced from [83]. Copyright 2011 ChemSusChem.

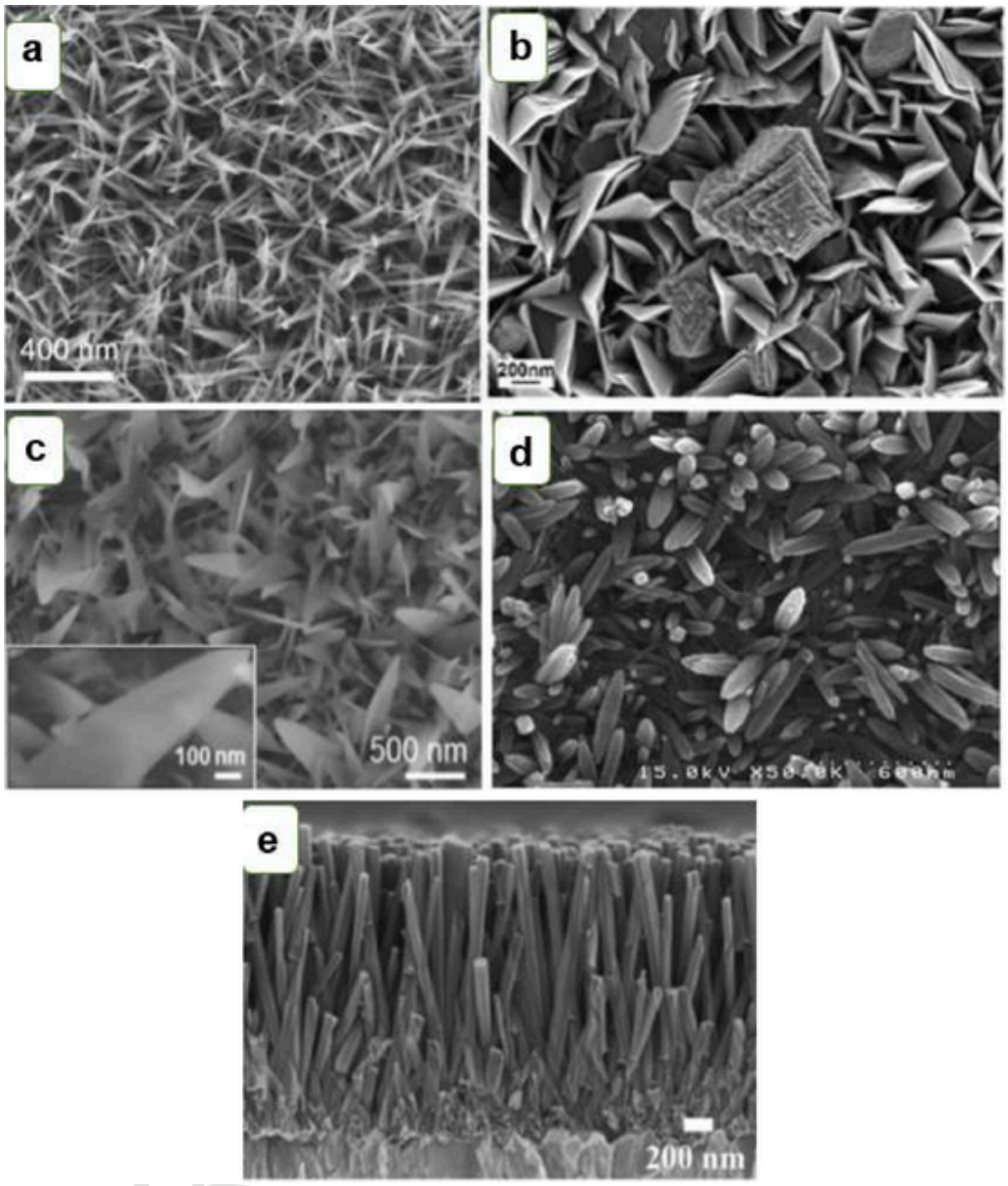

Fig. 5. Morphology images of (a) α -Fe_2O_3 nanowires. Reproduced from [88]. Copyright 2018 ACS Applied Materials & Interfaces. (b) α-Fe_2O_3 nanoflowers. Reproduced from [89]. Copyright 2019 Ceramics International. (c) α-Fe_2O_3 nanoflakes. Reproduced from [90]. Copyright 2017 Nano Energy. (d) α-Fe_2O_3 nanorods. Reproduced from [92]. Copyright 2020 Optik. (e) α -Fe_2O_3 nanotube. Reproduced from [94]. Copyright 2019 Applied Catalysis B: Environmental.

cluded superior carrier transfer capability, enhanced photocurrent density and greater photon capture [91]. In another work using a facile chemical bath deposition, hematite-based nanorods have been deposited on FTO-coated glass substrate **(**Fig. 5**d)** the electrode has shown considerable activity as a photoanode for photoelectrochemical splitting of water with a maximum photocurrent density of water splitting of 700 μA.cm^{-2} at 1.6 V (RHE) [92]. In another work, it was shown that the conversion of α-Fe_2O_3 nanoparticles into nanorods leads to an increase in the specific surface area, which in turn leads to better electrochemical characteristics [93]. Very recently Chenchen et al., obtained hematite (α -Fe_2O_3) nanotube arrays with well-defined crystal structures with an average length of 2 μm (Fig.5e), this results in strongly enhanced light absorption and PEC activity for water oxidation with a photocurrent of about 1.2 mA cm^{-2} at 1.23 V (compared to, RHE) [94]. Mouchani and his team [95] have succeeded in modulating the oxygen vacancy in hematite thin films using annealing on a graphite bed for PEC water spliiting. The PEC characteristics indicated that the photocurrent density at 1.23 V vs. RHE was enhanced from 0.05 mA.cm^{-2} for the air annealed material to 0.27 mA.cm^{-2} for the flake graphite bed annealed material, this enhancement results from the creation of oxygen vacancies in the reducing atmosphere.

On the other hand, Qiu et al. [96], have shown the importance of photonic nanostructures in improving water splitting performance owing to their light harvesting ability. In this work they have succeeded in involving a new framework of PEC device with ultrathin hematite film deposited on regular arrays of conductive 3D nanospikes (NSPs). In this structure the ultrathin hematite films function as active photocarriers materials, as well as the conductive NSPs, act as an efficient carrier collection pathway. The specially designed 3D architectures have been used to efficiently harvest light, as observed in the optical absorption spectrum, the hematite deposited NSP device exhibited considerably improved light absorption than the planar device. Furthermore, the absorption was found to increase monotonically with the height of NSP with a percentage of 95.9 % for 1000 nm NSP array and 94, 2 % for

500 nm NSP grating [96]. Wada et al. [97] have observed the specific microwave absorption at the grain boundaries of the α-Fe_2O_3 photoanode, through which the energy can be delivered effectively to the localized carriers on the grain boundaries. Then, the synergy between the accumulation of holes on the material surface and the localization of carriers at grain boundaries improves the electron transfer pathway in the electrochemical water splitting, thereby effectively increasing the photocurrent density. In the other hand, Souza et al. [98] claimed that in thicker films, the intense interaction between the substrate and the film generates stress that causes defects in the crystal structure of the hematite film, thereby promoting the electron hole recombination process. For PEC water splitting, the nanostructured materials (NPs, NWs…) can offer a large interfacial area between the electrolyte and the photo-catalyst making it suitable for the transport and separation of charge carriers. For instance, an arrangement of single-crystal nanorods in the range of 10 nm in diameter, mounted and oriented perpendicularly to a conductive substrate, could avoid grain boundaries and offer a direct route for electron collection, whilst still enabling photogenerated holes to access the SCLJ efficiently [83]. In summary, well-designed morphologies provide a favorable pathway for charge carriers, thereby reducing recombination losses and facilitating efficient transport to the electrode-electrolyte interface. In addition, tuning the size, arrangement and shape of the nanostructures allows the energy levels to be aligned, lowering the energy barriers for charge carriers involved in the water splitting reactions [2]. Table 1 summarizes other investigations of the various surface morphologies of α-Fe_2O_3 that indicate their own role in monitoring the photoactivity and overall PEC performance of the cell [96].

2.2.2. *Heterojunctions strategy*

Besides morphology control, there are other approaches that have been adopted to enhance the performance of hematite-based photoanodes, among them elemental doping, surface treatment and heterojunctions. Substantially, the formation of a heterojunction structure and through synergistic effects caused by the interactions between the components, there is the creation of a variety of improvements which includes: Enhanced visible light absorption, improved charge carrier transport and separation, and extended electron-hole pair lifetimes [108,109]. Up to now the heterojunction based on α-Fe_2O_3/semiconductor architecture is more used than the other heterojunctions as for example SC/carbon and SC/metal [110]. In the same direction in 2018 Shabeeb et al. [111], reported α-Fe_2O_3/$NiFe_2O_4$ heterojunction which experienced higher water oxidation efficiency at a molar ratio of 1:1 and on 3D nanospike array (NSP) substrates. This improvement of the performance towards water oxidation compared to bare hematite is essentially linked to the building of the p-$NiFe_2O_4$/n-Fe_2O_3 heterojunction leading to a much more improved charge separation (e^-; h^+) as a result of the alignment of the Fe_2O_3 and $NiFe_2O_4$ band positions as observed in Fig. 6**(a)** [111]. The same team [112], showed that $CuFe_2O_4$/α-Fe_2O_3 composite thin films deposited on three-dimensional nanospike (NSP) substrates with a 1:1 molar ratio revealed robust results concerning PEC water splitting with an effective photocurrent density of 2.26 mA/cm² at 1.23 V RHE as well as a photoconversion efficiency (η_c) almost 2.8 % which is 4.17 times greater than that of pure hematite (η_c = 0.67 %). Previous work by Qiong Liu et al. [113], report that an enhanced photocurrent has been achieved for the $ZnFe_2O_4$ on α-Fe_2O_3 heterojunction. From the study, it is found that the alignment of Fe_2O_3 and $ZnFe_2O_4$ band positions enables a facile migration of photo-generated holes in the valence band of hematite to the $ZnFe_2O_4$ phase. Then the photo-generated electrons in the conduction band of $ZnFe_2O_4$ being transferring to α-Fe_2O_3 and then via the circuit to the counter electrode leading to the production of H_2. In another related study [114], it was stated that porous surface morphology of the α-Fe_2O_3/CuO heterostructure may ease photo-generated charge separation. During heterojunction formation of α-Fe_2O_3/CuO, there is creation of a space charge zone as shown in the Fig. 6**(b)**, this region is essentially owed to the spreading of the majority charge carriers of the p-type (CuO) and n-type (α-Fe_2O_3) materials in opposite directions, thus enabling the generation of an integrated electric field at the p-n junction, that is playing a very crucial role in the enhancement of the photocurrent response via the reduction of the pair recombination rate (e^-; h^+) [114]. It is well known that the use of metal oxide derived from metal–organic framework (MOF) is other favorable approach to override the slow water oxidation reaction because of large specific surface area of MOF precursor and therefore provide more active sites on electrode/electrolyte surface [115,116]. Currently [117], the p-n heterojunction Cu_2O/Ce-Fe_2O_3 derived from MOF amended with amorphous co-catalyst FeOOH exhibited a more significant photocurrent of 4.2 mA.cm^{-2} at 1.23 V RHE as well as IPCE value is 73.6 % at 400 nm and 0.56 % for the applied bias photon to current conversion efficacy (ABPE) in addition to 93.8 % efficiency regarding the surface charge transfer. This PEC efficiency is mainly due to the Cu_2O derived from MOF which acts as a supplier of active sites for the water oxidation reaction and the presence of Ce as a dopant allows to enhance the conductivity of Fe_2O_3 [117]. The satisfactory photoelectrochemical response was attained by employing the n/n type junction ZnO/Ag-(α) Fe_2O_3 as presented in Fig. 6**(c)** [118]. In another study published by Yi Wen et al. [119], in which they revealed the effect of incorporating electrochemically reduced graphene oxide (eRGO) and nickel oxide (NiO) on Hematite in terms charge transfer and light absorption [119]. This ternary heterostructure (eRGO/NiO/α-Fe_2O_3) displayed a hydrogen evolution rate at 92 μmol. h^{-1}. cm^{-2} which is 3-fold better than that of nude Hematite.This enhancement is generally due to the eRGO sheets that enables efficient separation of electron-hole pairs by forming cohesive interface between NiO and α-Fe_2O_3 which acts as an electron transport bridging to the SC/electrolyte interface (Fig. 6**(d)**). Alongside this discussion, and by creating a chemical equilibrium between electrolyte and the material, an electric field is formed that can be exploited to separate the e^-/h^+pairs produced. Working in 'hidden junction' mode, where the photovoltage production is decoupled from its source, the photovoltage is generated via the difference between two materials working at their Fermi level and this is called the Fermi level- difference (EF). In both situations, the photovoltaics are limited by the difference between the electrons and holes at the nearest Fermi level, thus, it is a critical issue to optimise the EF differences in order to enhance the photovoltage. In addition, the imperfect band alignment of the semiconductors in a 'hidden junction' can lead to less equation of state splitting, resulting in less photovoltage [120]. Zhang et al. [121] succeeded in integrating a novel copper-cobalt oxide ($CuCoO_x$) cocatalyst and an ultra-thin Al_2O_3 layer and on α-Fe_2O_3 photoanode to construct an unob-

Table 1
Summarized α-Fe_2O_3 nanostructures synthesized and their PEC performances.

Hematite Photoanode	Morphology	Synthesis method	Photocurrent at 1.23 V vs. RHE	Ref.
α-Fe_2O_3	Nanowires	Hydrothermal	1.24 mA/cm²	[99]
α-Fe_2O_3	Nanotubes	Sonoelectrochemical Anodization	1.41 mA/cm²	[100]
α-Fe_2O_3	Nanopetals	Pulse reverse Electrodeposition	0.39 mA/cm²	[101]
α-Fe_2O_3	Nanoparticles	Anodization	0.05 mA/cm²	[102]
α-Fe_2O_3	Cauliflower	Particle-assisted Deposition	3.0 mA/cm²	[84]
α-Fe_2O_3	Nanorods	Atomic layer Deposition	0.11 mA/cm²	[103]
α-Fe_2O_3	Nanosheets	Anodization	1.5 mA/cm²	[104]
α-Fe_2O_3	Mesoporous	Solution-Based Colloidal	0.56 mA/cm²	[105]
α-Fe_2O_3	Dendrites	Electrodeposition	0.018 mA/cm²	[106]
α-Fe_2O_3	Nanocorals	Pulse reverse Electrodeposition	0.813 mA/cm²	[107]

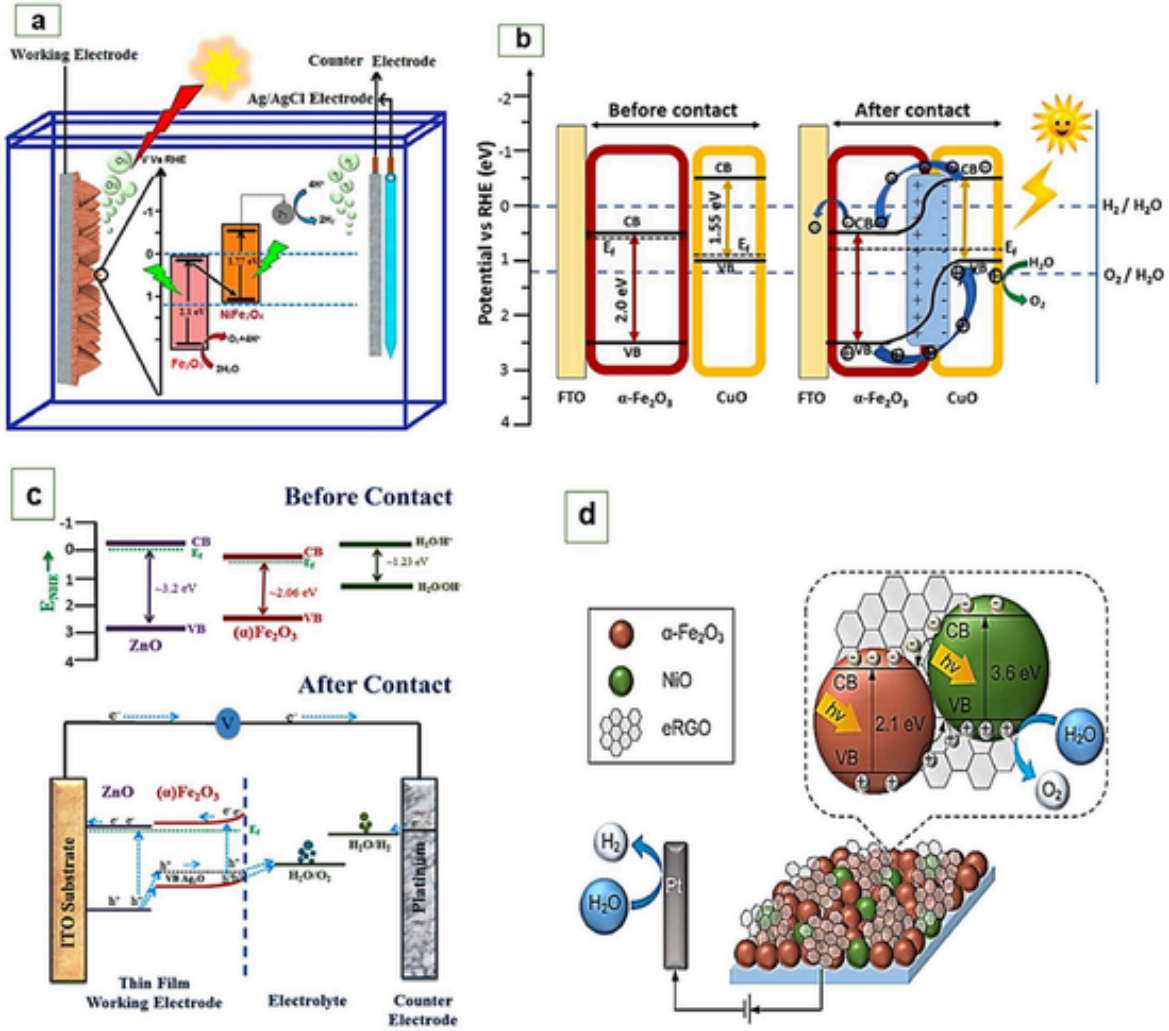

Fig. 6. (a) Diagram showing the Z schematics direct charge transfer route for the α-Fe_2O_3/$NiFe_2O_4$ heterojunction. Reproduced from [111]. Copyright 2018 Langmuir. (b) Charge transfer pathway in a Fe_2O_3/CuO heterojunction photoanode for PEC water separation. Reproduced from [114]. Copyright 2021 Journal of Alloys and Compounds. (c) Illustrative diagram of the direct charge transfers way of the ZnO/Ag-α-Fe_2O_3. Reproduced from [118]. Copyright 2021 Renewable Energy. (d) charge transfer mechanism of the eRGO/NiO/α-Fe_2O_3 heterojunction. Reproduced from [119]. Copyright 2017 Solar Energy Materials and Solar Cells.

structed hole transfer channel and improve PEC performance. The obtained α-Fe_2O_3/Al_2O_3/$CuCoO_x$ photoanode shows high photocurrent density of 2.23 mA/cm² at 1.23 V vs. RHE and negative onset potential of 0.7 VRHE, approximately 17.6 fold greater and 200 mV cathodic shift compared to bare α-Fe_2O_3 [121]. Chen et al. [122] have prepared a bimetallic oxyhydroxide NiFeOOH film on Fe_2O_3 catalyst via a simple electroless ligand-regulated oxidation process to construct a highly tuned semiconductor/cocatalyst interface. Benefiting from low overpotential of bimetallic oxyhydroxide NiFeOOH and the accelerated OER kinetics, the resulting NiFeOOH/ Fe_2O_3 composite with strongly bound heterojunction interface exhibits superior visible light absorption, improved photocurrent density (1.83 mA/cm² at 1.23 VRHE) and better stability compared to bare Fe_2O_3 photoanode [122].

2.2.3. *Doping technology*

During the last years, the inclusion of an element as a dopant has been regarded as a promising approach for improving the overall performance of a hematite-based photoanodes [123–126]. In general, doping is supposed to increase the charge carrier's concentration and thus improve the electrical conductivity of a hematite-based photoanodes. Among the more widely elements used to dope hematite photoanodes for improving its photoactivity as well as carrier mobility we can mention metals like Ti [127–129], Ni [130,131], Sn [132,133], Zn [134,135], Mn [136], Cu [124,137]. Nevertheless, it has been pointed out that the various doping types result in negative effects like the creation of localised impurity states which might function as recombination sites in the band gap for the photoexcited charge carriers [138,139]. Hence, it is necessary to use an appropriate doping mode to improve the PEC activity of *α*-Fe_2O_3 [135] Zhu et al. [140], have explored the effect of bimetallic doping on the improvement of electronic properties of hematite-based photoanode. In this work, they are based on the hydrothermal process followed by dip-sintering operation to homogeneously introduce the two dopants (Zn, Ti) into the n-type Fe_2O_3 photoanode [140]. The morphological analysis showed that the addition of the $TiCl_4$ precursor allowed a shift from a nanorods type nanostructure (Virgin hematite, Fig. 7**a**) to a nanocubes kind of porous morphology (Ti-Fe_2O_3, Fig. 7**b**). However, the insertion of Zn has not changed the morphology **(**Fig. 7**c)** which shows that Zn was inserted inside the mass of the Ti-doped hematite instead of deposited on its surface. In addition, transmission electron microscope analysis (Fig. 7**d**) and EDX elemental-mapping (Fig. 7**e and h**) showed that Zn, Ti were homogeneously distributed in the hematite resulting in more improved photoelectrochemical results as shown in Fig. 7**(i)**, which are 2.5 times improvement in photocurrent density of the Fe_2O_3 electrode co-doped with Ti, Zn compared to that of the virgin hematite photoanode [140]. Besides the homogeneous distribution of Zn and Ti, the enhanced PEC

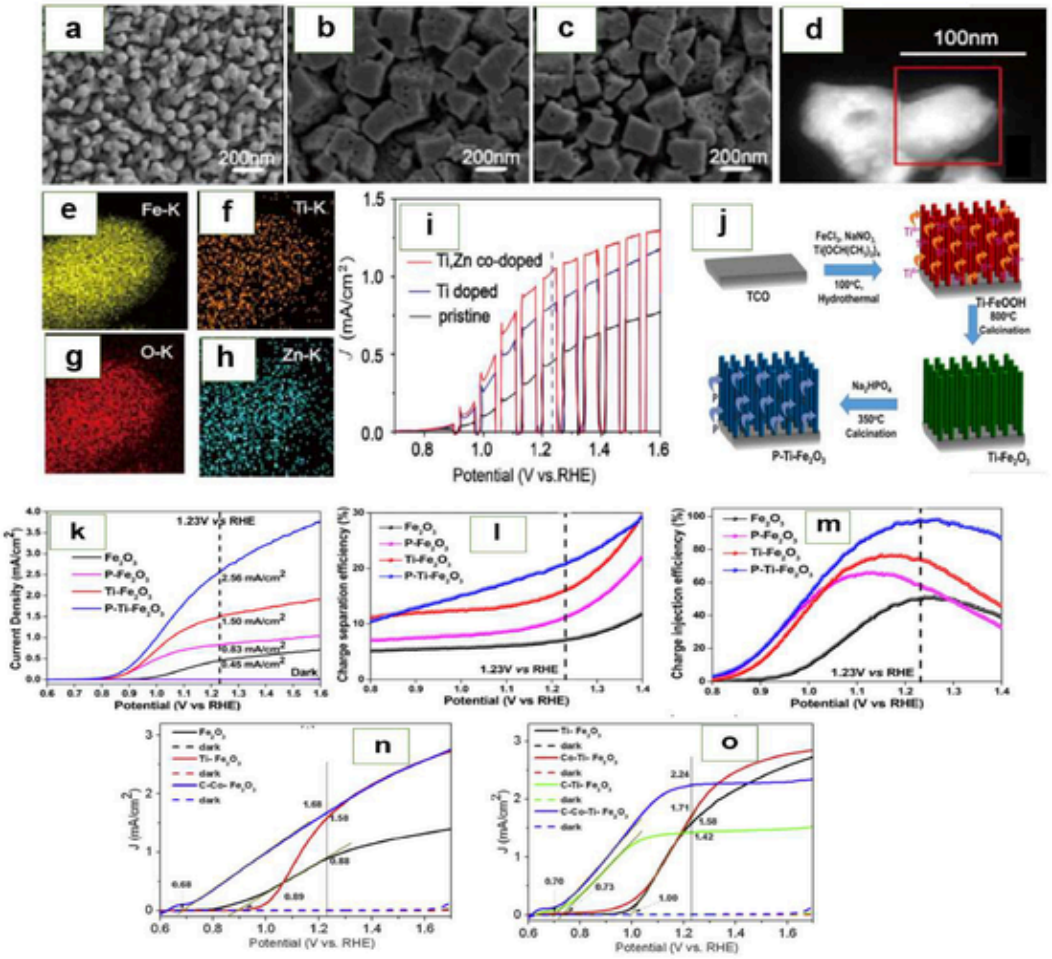

Fig. 7. SEM micrographs of (a) virgin hematite, (b) Ti—Fe_2O_3, (c) Ti—Zn—Fe_2O_3. (d) TEM image of Ti—Zn—Fe_2O_3. (e-h) EDX mapping of Fe, O, Zn and Ti. (i) LSV curves of Ti—Zn—Fe_2O_3 Ti—Fe_2O_3 and virgin hematite. Reproduced from [140]. Copyright 2019 Journal of Energy Chemistry. (j) Schematic representation of the manufacturing method of the P—Ti—Fe_2O_3 photo-anode using in-situ doping of Ti and ex-situ doping of P. (k) Photocurrent density plots according to the potential polarization of pristine and modified hematite photoelectrodes. (l and m) Charge separation and charge injection efficiency of pristine and modified hematite photoelectrodes. Reproduced from [142]. Copyright 2019 ACS Applied Energy Materials. (n) *J–V* scanning of pristine hematite, Ti—Fe_2O_3 and C—Co-Fe_2O_3. (m) Photocurrent density plots according to the potential polarization of Ti-Fe_2O_3, Co—Ti—Fe_2O_3 and C—Co—Ti—Fe_2O_3. Reproduced from [143]. Copyright 2019 Applied Catalysis B: Environmental.

performance of the Zn, Ti-Fe_2O_3 photoanode was also attributed to a higher carrier density that elicited by the Ti dopant as well as a reduction in the recombination of electron-hole into the mass and surface of the photoanode elicited by the Zn dopant [140]. Zhang et al. [141], proved that with a facile electrochemical activation procedure that altered the bulk and surface properties, the co-doped Nb—Sn—Fe_2O_3 photoelectrode applied for this bulk and surface activation condition has demonstrated an effective enhancement in PEC performance. Furthermore, they showed that these modifications provided fewer defects with more enriched Sn—O and Nb—O bonds to hematite, thereby passivizing the surface trap states and enhancing its PEC stability as well as the separation efficiencies of charges both in the bulk (η_{bulk}) and on the surface ($\eta_{surface}$) Hence the codoped photoanode (Nb—Sn—Fe_2O_3) displayed a photocurrent enhancement of 62 % as compared to virgin hematite[141]. In a further work Sahu et al. [142], investigated the impact of incorporation of metals (Titanium) and non-metals (Phosphorus) on hematite photoelectrode. The design of this photoelectrode was based on in-situ and ex-situ processes at different annealing temperatures to finally arrive at the P—Ti—Fe_2O_3 co-doped photoelectrode **(**Fig. 7**(j)**. EIS data and Moot-Schottky(MS) analysis showed that the P—Ti—Fe_2O_3 co-doped photoelectrode exhibits more efficient charge separation and improved charge carrier density hence a significantly greater photocurrent of 2.56 mA/cm² and a V_{onset} cathodic shift (~90 mV) was obtained **(**Fig. 7**k)**.The charge separation efficiency (η_{sep}) as well as the charge injection efficiency (η_{inj}) can be seen in Fig. 7**(l-m)**, where the separation efficiency is systematically considered as a control parameter for the PEC performance with its highest value achieved through the P—Ti—Fe_2O_3 photoanode (around 20 %). Nevertheless, with the same device having a hole injection performance approaching 100 % at 1.23 V vs. RHE, surpassing the other devices tested, explaining its significant increase in photocurrent [142].

Lan et al. [143], reported the use of a Cobalt (Co) doped carbon layer applied on hematite to substantially enhance the oxidation performance of solar water. Fig. 7**(n)** demonstrates that with respect to pristine α -Fe_2O_3, the Ti-doped sample shows an improved photocurrent response although revealing a poorer onset potential. After Co and C treatment, the C—Co—Fe_2O_3 photoanode exhibited a significantly enhanced performance together with a remarkable cathodic onset potential shift of 210 mV and a photocurrent density of 1.68 mA /cm² at 1.23 V vs. RHE [143]. This betterment was substantiated by the Co-doped carbon layer which acted as a tri-functional material that

blocked the defects on the surface and improved its conductivity via the sp2 carbon structure, accelerating the oxygen evolution reaction process [143]. On the other hand, in case the Co and C-based treatment has been extended to the Ti-treated photoelectrode like shown in Fig. 7 **(o),** a noteworthy performance improvement may be found which is expressed by a photo current density of 2.24 mA/cm² at 1.23 V vs RHE [143]. Hien and his team [133] have shown that Sn may be successfully doped into the hematite, resulting in improved photoelectrochemical activities in comparison to undoped hematite. The Sn-doped Fe_2O_3 exhibits improved photocurrent density, which is attributed to an enhancement of charge carriers and a concomitant improvement of charge conduction [133]. Recently, a novel catalyst, S-doped FeOOH, was deposited on the surface of the Fe_2O_3 NR framework using a simple chemical bath deposition technique integrated with thermal sulphuration. The composite Fe_2O_3@S-FeOOH photoanode achieved a significant enhancement in PEC efficiency of 2.30 mA cm^{-2} at 1.23 V. vs RHE with an apparent negatively shifted onset potential of 250 mV relative to bare Fe_2O_3 (0.95 mA cm^{-2} at 1.23 VRHE [125]. Shaohua et al. [144] reported the mechanism of the $Ag_xFe_{2-x}O_3$ overcoat catalyzing the water oxidation reaction, as shown in Fig. 8. In the presence of sunlight, electrons were excited from the oxygen to the iron (S1), and the holes linked to the oxygen led to the oxidation of Ag^{I} to Ag^{III} (S2). The Oxidized Ag^{III} may help the oxidation of water to generate oxygen and in the meantime be reduced back to Ag^{I} (S3). This multi-step charge transfer mechanism was designed to avoid the recombination of oxygen associated holes with surface electrons or surface traps, thereby catalyzing the water splitting reaction.

2.3. Copper based oxides photo-electrocatalysts

2.3.1. Morphological handling

It is widely recognized that cupric oxide (CuO) crystallizes within two crystallographic structures, cubic and monoclinic, where the latter exhibited high chemical and structural stability that was confirmed by a more negative value of cohesive energy about −6.01 eV/atom which is lower than that obtained by the cubic structure (−5.60 eV/atom). Besides the great microstructure variety of CuO and its easy synthesis, it is well noticed that the morphology control with controllable dimensions has a meaningful impact on the photoelectrochemical performances of the photocathode [145,146]. Saeid et al. [147], exhibited the significance of the crystal grade impact of the CuO photocathode on the performance of PEC water splitting. They indicated that an increase in film thickness from 150 nm to 500 nm leads to an improvement in photocurrent from 0.92 mA/cm² to 2.5 mA/cm² at 0 V vs. RHE respectively. Similarly, Tran et al. [148], performed a systematic investigation about the significant parameters which may influence the morphological and size of CuO nanomaterials. In the same context, Saeid et al. [149] were based on a thermal treatment in order to tune the crystallinity as well as the surface morphology of CuO based films. They found that increased annealing temperature leads to improved crystallinity which substantially improves the photocurrent generation capacity with a stronger stability towards photocorrosion. Also 1D nanoamterials such as nanorods and nanowires have been exploited in the fields of catalysis in particular for photoelectrochemical water splitting thanks to its impressive photoelectric properties such as an efficient charge transport [150]. By way of example Jianming et al. [151], through a facile thermal treatment procedure, they succeeded in elaborating cupric oxide (CuO) nanowires from a copper substrate. In this work, it has been established the effect of one-step and two-step heat treatment on the photoelectrochemical performance of CuO photocathode. As observed in the SEM images of Fig. 9**(a),** the two-step calcined photocathode (300 °C for 1 h and 500 °C for 2 h) exhibited a more compact interface between the formed CuO nanowires and copper substrates than the one-step calcined photocathode (500 °C for 2 h) This is an advantage for the charge transfer of the nanowires to the substrates, this is supported by the electrochemical impedance results as can be seen in Fig. 9**(b)**. The two-step calcined photocathodes showed a small radius arc as opposed to the one-step calcined photocathodes suggesting that the separation of photo-generated charge is significantly better after two-step treatment [151]. Furthermore, from Fig. 9**(c and d)** it can be observed that the two-step processed photocathode called CuO 300–500 displayed a strong photocurrent enhancement about 1.4 mA/cm² at 0 V against RHE using Air Mass1.5G irradiation with a very positive onset potential of 0.7 V that will be energetically beneficial. As more positive onset potential the more chance there is of cooperating together with a photoanode in order to build a photoelectrochemical water separation cell with no bias [151]. The photostability test (Fig. 9**e)** revealed a decrease in photocurrent to 0.4 mA/cm² during 10 min that represents just 35 % of the initially photocurrent. This low stability can be driven mainly by CuO reduction to Cu_2O then to Cu via photogenerated electrons rendering this electron portion ineffective for hydrogen generation [151].

Kushwaha et al. [145], engineered a process involving an aqueous solution in which changing the concentration of the precursors yielded two types of morphologies (oriented nano-sheets and nano-leaves) as illustrated in the SEM images in Fig. 10**(a and b)**. The oriented nanosheets morphology was achieved at the lowest concentration (10 mM) as shown in Fig. 10**(a)**. The nanosheets are randomly linked with each other which makes them dense with a mean thickness of 50 nm, however increasing the concentration by about 50 mM leads to the formation of a new morphology called nanoleaves **(**Fig. 10**b)** This nanostructure displays separated nanoleaves from each other creating a wide surface/porosity [145]. As already reported, obtaining different CuO morphologies depends mainly on the growth and nucleation rate

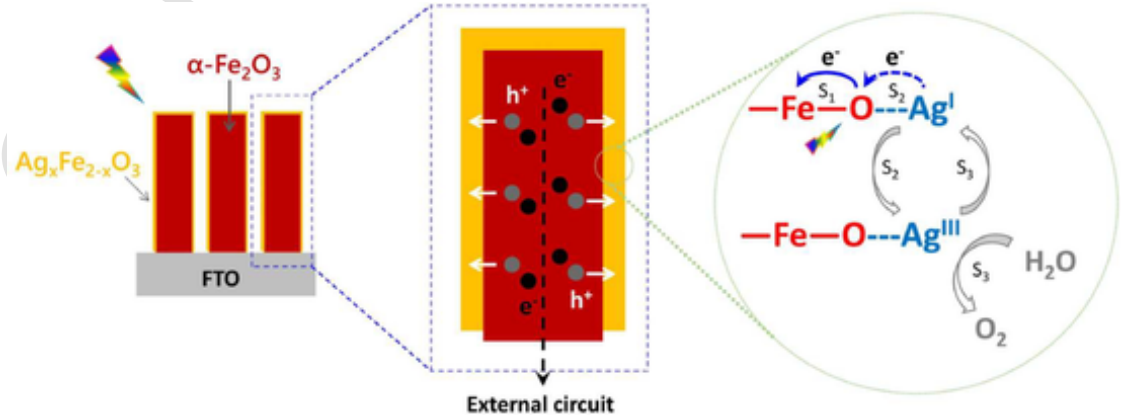

Fig. 8. Core/shell assembled α-Fe_2O_3/$Ag_xFe_{2-x}O_3$ and the scheme of the water oxidation reaction promoted by the $Ag_xFe_{2-x}O_3$ overlayer. Reproduced from [144]. Copyright 2014 Nature.

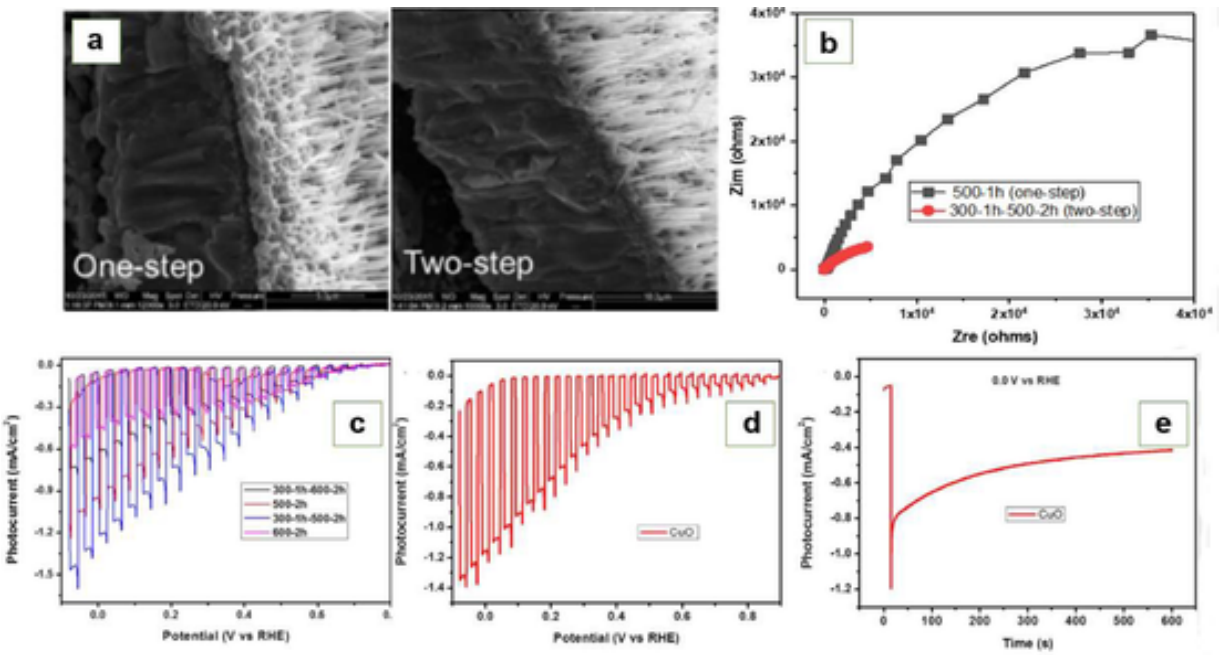

Fig. 9. (a) SEM of photoelectrodes prepared using one- and two-step annealing. (b) EIS of photoelectrodes following one- and two-step treatment. (c) Current-potential graph of CuO photocathodes produced using one and two step annealing at various temperatures. (d and e) Current-potential graph and stability test of a photocathode treated in two steps (300 for 1 h and 500 for 2 h). Reproduced from [151]. Copyright 2018 Applied Catalysis B: Environmental.

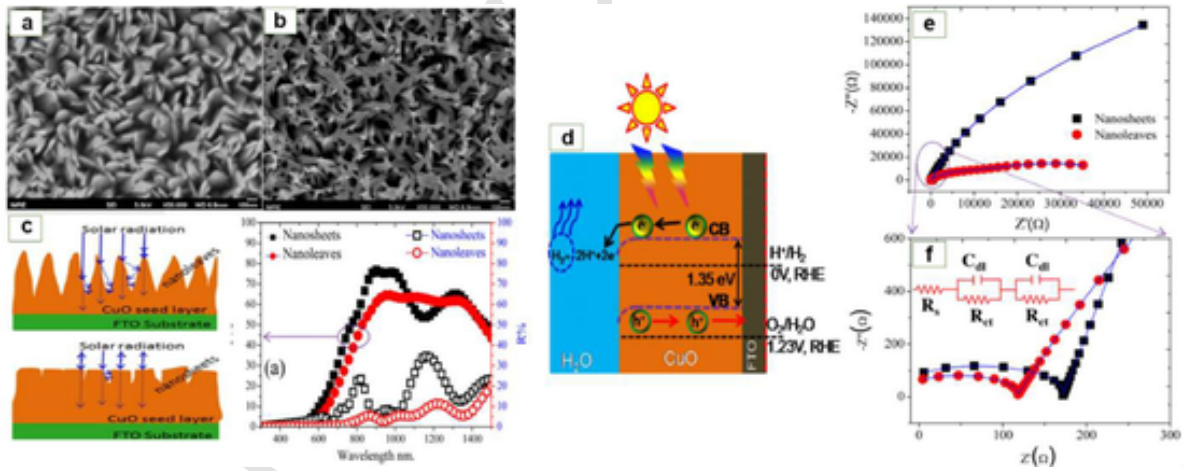

Fig. 10. SEM images of CuO-based phoelectrodes with various morphologies. (a) nanosheets and (b) nanoleaves. (c) Spectra of reflectance and Transmittance of CuO nanoleaves and nanosheets. (d) Charge transfer process of the CuO photoelectrode. (e) Nyquist plot for CuO nanosheets and nanoleaves. (f) Zoomed-in view of the EIS spectra high frequency section. Reproduced from [145]. Copyright 2017 Journal of Photochemistry and Photobiology A: Chemistry.

which varies with the quantity of starting precursors used [152,153]. The optical analysis presented in Fig. 10**(c)**, showed that nanoleaves exhibit high light absorption due to their lower transmittance/reflectance compared to nanosheets, as well as the more oscillations in the reflectance spectrum of nanosheets shows a slicker surface which leads to high reflection in contrast to nanoleaves which exhibit a rougher surface thus more diffuse reflection [145]. The gap energy recorded for nanoleaves is 1.26 eV while for nanosheets it is 1.33 eV, which confirms the high light absorption capacity by nanoleaves. Fig. 10(d) shows a simplified diagram of the charge transfer pathway, the energy difference between the fermi level and the redox potential of the electrolyte enables the photo-generated electrons to migrate to the electrolyte and the holes to the substrate sites (FTO) and then to the counter-electrode (Pt), as can be seen in the diagram, the position of the conduction band in relation to the position of the water reduction potential $E^{\circ}_{H+/H2}$ allows the reduction of the water and the generation of H_2. Due to its smaller charge carrier distance as well as its large surface area the nanoleaves morphology exhibits the maximum value of photocurrent which is 1.5 mA/cm² at 0 V vs. RHE while for the nanosheets is 1.1 mA/cm² at 0 V vs. RHE [145]. Fig. 10**(e and f)** illustrates the electrochemical impedance spectroscopy readings for the two nanostructures formed (nanosheets and nanoleaves). From the adjustment of the EIS data, they found that in the high frequency section corresponding to the CuO - FTO interface impedance, the nanoleaves photoelectrodes exhibit the lowest value of charge transfer resistance leading to a greater electrical connection between FTO and CuO nanoleaves resulting in a higher charge collection capacity. Regarding the low frequency region corresponding to the CuO-electrolyte interface, the adjustment of the EIS plots reveals a reduced charge transfer resistance for the nanoleaves photoelectrode (34.1 Ω) as compared to the nanosheets photoelectrode (628.1 Ω).This confirms the ability of the nanoleaves

structure to transfer the photo-excited electrons to the electrolyte solution in order to reduce the H^+ protons into H_2 [145].

2.3.2. Heterojunctions strategy

In an effort to surmount the disadvantages related to CuO, such as its sensitivity to photocorrosion and high rates of recombination, a number of strategies have been reported. Among them consists in building heterojunctions together with other semiconductors for promoting a more efficient charge carrier separation and avoiding photocorrosion [154,155]. In the last few years, CuO/Cu_2O heterostructures have gained a significant attention thanks to their high photoelectrochemical performance and improved photo stability as well as to their easy manufacturing using various methods [156]. John et al. [157], developed ramified CuO/Cu_2O heterostructures. As can be seen in Fig. 11**(a)**, a mixture of methods was used. Firstly, Cu_2O nanowires (NWs) were obtained by anodising a copper foil followed by heat treatment at 450 °C, and then hydrothermal processing at 100 °C for 10 min yielded a CuO/Cu_2O nanowire/nanoflake heterostructure (CuO/Cu_2O- Hy NFs/NWs). A short annealing at 250 °C during 5 min is carried out for growing a conforming CuO layer on the exposed Cu_2O NWs between the CuO NFs (CuO/Cu_2O- HyA NFs/NWs) [157]. On the other hand, a shell/core CuO/Cu_2O heterostructure was manufactured by direct annealing without hydrothermal treatment. The calculation of the band level positions results in the appearance of a type II heterostructure which allows the photoexcited electrons to migrate from the more negative conduction band of Cu_2O to the conduction band of CuO while the photo-generated

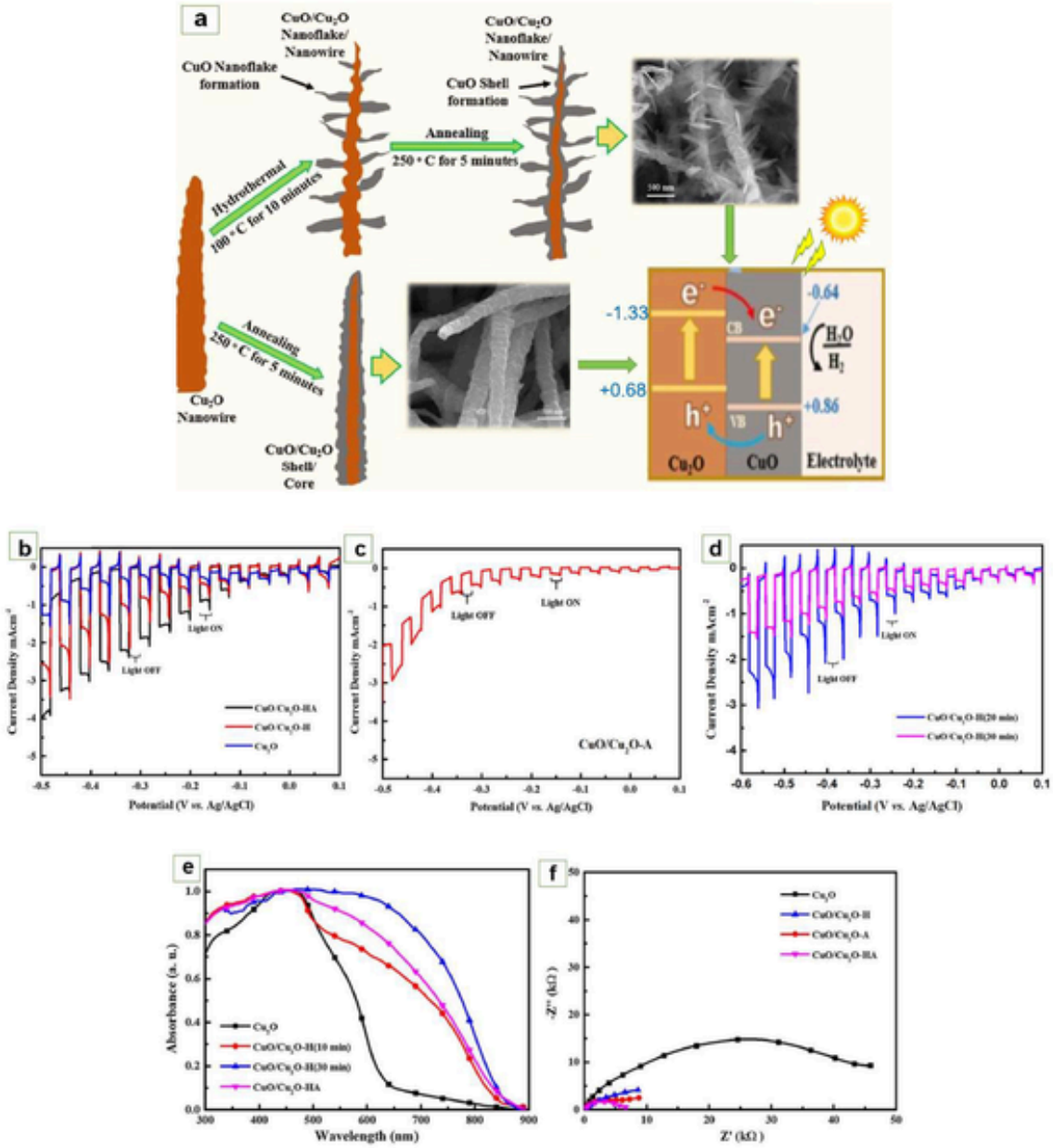

Fig. 11. (a) CuO/Cu_2O Nanoflakes/Nanowires produced using hydrothermal treatment of Cu_2O nanowires followed by a short annealing at 250 °C (Cuo/Cu_2O—HyA). CuO/Cu_2O shell/core achieved by direct annealing of Cu_2O nanowires. (b–d) photocurrent measurements of heterostructures prepared at different conditions. (e) absorption spectrum of the heterojunction obtained by hydrothermal treatment alone at t = 10 min (CuO/Cu_2O—Hy 10 min) and t = 30 min (CuO/Cu_2O—Hy30min) and of the heterojunction (CuO/Cu_2O—HyA 10 min) achieved by a short annealing, and the virgin Cu_2O sample. (f) EIS results for heterostructures made under various conditions. Reproduced from [157]. Copyright 2020 Applied Surface Science.

holes are moved from the more positive valence band of CuO to the valence band of Cu_2O [157]. The photocurrent measurements achieved at different conditions are presented in Fig. 11 **(b–d).** As can be clearly noticed in Fig. 11**(b and c)** the highest value of photocurrent density was recorded for the heterostructure obtained by hydrothermal processing at 10 min followed by a short annealing (CuO/Cu_2O- HyA NFs/NWs) The superiority of this heterostructure was ascribed to the conformable covering of CuO over Cu_2O which improves the interface region of the heterojunction as well as the synergistic effect of the two materials which leads to a better charge separation at the NFs/NWs interface, that is also reinforced by the higher surface area provided by the nanostructures. Fig. 11**(d)** presents the effect of hydrothermal reaction time on photocurrent density. It indicated that with increasing hydrothermal reaction time the density of CuO NFs is enhanced which can promote the inhibition of the heterojunction effect, thereby restricting the photocurrent [157]. In contrast, optical measurements of the fabricated heterostructures shown in Fig. 11**(e)** indicated that the absorbance increased with increasing hydrothermal reaction time in the range of 640–860 nm owing to the development of CuO indicating that the photocurrent performance is not driven by optical absorption but rather by the charge separation at the CuO/Cu_2O. These properties were confirmed by the electrochemical impedance measurements as it can be seen in Fig. 11**(f)** that the CuO/Cu_2O heterostructure with a hydrothermal method following a short annealing at 250 °C during 5 min (CuO/Cu_2O—HyA) has the lowest semicircular arc which implies the weakest resistance of charge transfer and hence the best charge separation [157].

Chang et al. [158], made an endeavour to construct a CuO/ZnO photocathode. They prepared a p-n heterojunction in p-CuO/n-ZnO nanowire arrays (NWs) by a combination of several methods. Firstly, and by using electrodeposition a copper (Cu) film has been deposited on FTO following by chemical oxidation and immersion coating, finally arriving at the CuO/ZnO (NWs) composite. The photocurrent density recorded by this photocathode was - 8.1 mA/ cm^2 at 0 vs. RHE. Fig. 12 **(a)** shows an illustration of the FTO-coated CuO/ZnO heterojunction irradiated with visible light. As it can be observed that the charge transfer takes place according to a type II heterojunction, the photo-generated electrons can move from p-type CuO to n-type ZnO which favours the charge separation resulting in an improved rate of hydrogen production. On the one hand,the narrow band gap of CuO improves the absorption of light and on the other hand it has been shown that the ZnO layer allows to protect CuO against corrosion and to form a charge zone which is able to provide the necessary energy to have a better charge separation [158]. To date, the use of an external polarisation is needed for nearly all PEC systems in order to provide an efficient charge separation and to bridge the resistance occurring between the photocath-

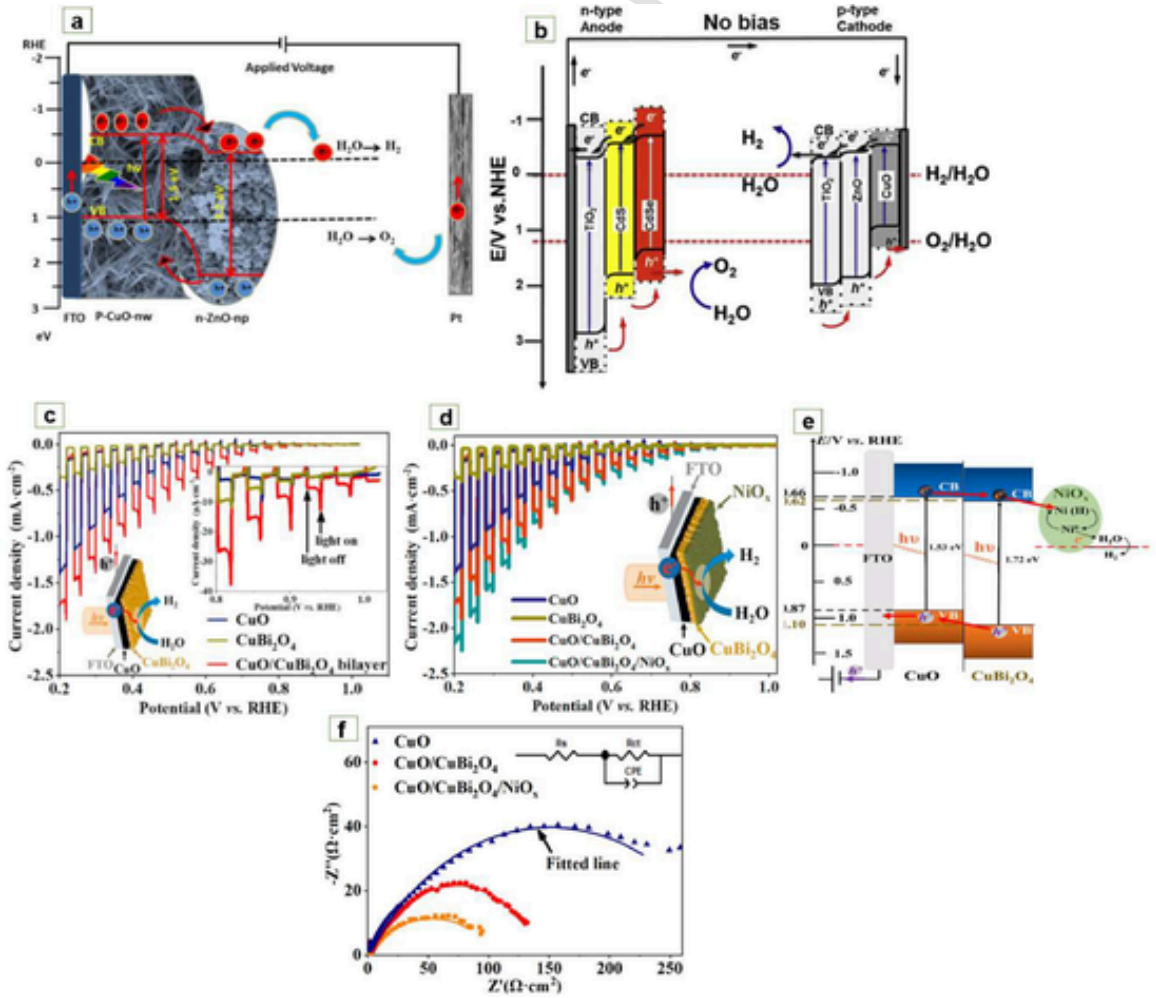

Fig. 12. (a) Illustration of the energy diagram of the p-CuO/n-ZnO heterojunction. Reproduced from [158]. Copyright 2017 Energy materials. (b) Band diagram of the photoelectric cell comprising photoelectrodes based on n-TiO_2 and p-CuO. Reproduced from [159]. Copyright 2020 Journal of Hydrogen Energy. (c and d) Current density-potential measurements before and after incorporation of the NiO_x layer on the photocathode CuO/$CuBi_2O_4$. (e) Band diagram of the photocathode CuO/$CuBi_2O_4$/ NiO_x. (f) Nyquist graphs of pristine CuO, CuO/$CuBi_2O_4$ bilayer photocathode and CuO/$CuBi_2O_4$/NiO_x measuring at 0.40 V according to RHE. Reproduced from [160]. Copyright 2021 Journal of Hydrogen Energy.

odes, however applying a bias externally is not economically or environmentally preferable. Consequently, developing a PEC cell which will not necessitate an external bias to initiate a water separation reaction would be highly desirable. Shaislamov et al. [159] have demonstrated an unbiased photoelectrochemical water splitting approach, by combining a brief-circuited photoanode (n-type) with a photocathode (p-type).

Among the benefits of using this approach is the integrated voltage between the p-type photocathode and the n-type photoanode, helping to achieve charge separation in each photoelectrode [159]. To achieve their goal, a combination of a p-CuO nanoflake-based photocathode with an n-TiO_2 nanorod-based photoanode in a PEC system with no external polarisation has been developed. As can be seen in Fig. 12**(b)**, when the two electrodes are irradiated with light whose photon energy is higher than their gap energy that implies the generation of (e^-; h^+) pairs in the two photocathodes (n and p). The photoexcited electrons in the p-CuO photocathode result in the reduction of water to hydrogen whereas the photo-generated holes in the n-TiO_2 photocathode lead to the oxidation of water to oxygen [159]. On the other hand, Zhang et al. [160], developed a CuO/$CuBi_2O_4$ based bilayer photocathode for photoelectrochemical hydrogen generation. Substantial enhancements in the PEC performance are achieved after the formation of the CuO/$CuBi_2O_4$ heterojunction as can be seen in the representative linear sweep voltammetry (LSV) scans displayed in Fig. 12**(c),** the photocurrent density provided by the CuO/$CuBi_2O_4$ heterojunction was about 1.73 mA/cm² at 0.2 V vs. RHE.This value is 4.81 and 1.25 times greater than that provided by the pristine $CuBi_2O_4$ and CuO, respectively. It has been found that the incorporation of the NiO_x layer on the CuO/$CuBi_2O_4$ heterojunction allows for a significant increase in photoactivity and improved stability [160]. Fig. 12**(d)** shows the LSV scans for the CuO, $CuBi_2O_4$, CuO/$CuBi_2O_4$ and CuO/$CuBi_2O_4$/NiO_x photocathodes, the last of which recorded the highest photocurrent density (2.17 mA/cm² at 0.2 V. vs RHE), with a more positive onset potential of 1.10 V and a faradic efficiency of 73.3 %, suggesting that most of the calculated photocurrent density was accounted by the HER process [160]. These excellent results have been attributed to several factors, for example the greater specific surface area which results in a high injection of charge carriers into the electrolyte, improved charge transfer efficiency due to a type II heterojunction with appropriate edge positions for water reduction. As shown in Fig. 12**(e)** the photo-excited electrons are migrating from the CuO conduction band to the $CuBi_2O_4$ conduction band and then through the NiO_x layer to the electrolyte, while the photo-generated holes are transported through the circuit to the counter electrode. The EIS results presented in Fig. 12**(f)** confirm the strong photoelectrochemical properties of the CuO/$CuBi_2O_4$/NiO_x composite, with the lowest charge transfer resistance was obtained, compared to other photocathodes (CuO, CuO/$CuBi_2O_4$) [160].

2.3.3. Doping technology

In the recent years doping is considered as a desirable technology to obtain hybrid materials with appropriate characteristics and capabilities for water splitting. In the preceding research into the CuO photoelectrode, doping investigations were carried out involving a number of materials, namely transition metals (Fe, Co, Cr, Mn, Zn, Ni) as well as an alkaline earth metal (Mg) [161,162]. These studies showed that the photocurrent density was found to improve with increasing conductivity [161]. Jaejin et al. [163], showed that doping the CuO seed layer by nickel influenced characteristics including the surface roughness, crystal quality and photostability. They proved that the Ni-doped atoms in the seeding layers scattered through the CuO nanostructures, leading to a reduction of the current of the dark as the scattered Ni atoms disabled the reduction of the metallic oxide into metal. Furthermore, as the Ni-doped seed layers were rougher and with a larger surface area compared to the non-doped layer, the adhesion strength was enhanced when the contact zone between the seeding layer and the CuO nanostructures was expanded, suppressing the photostability degradation. The maximum photostability value of 46.2 % was found to be obtained when the sample was doped with 10 at% Ni [163]. Recently Ashour et al. [164] published a paper on the fabrication of a Barium-doped cupric oxide (CuO) photoelectrode. As can be seen in Fig. 13**(a),** the Ba-doped CuO films have been fabricated by a simple method of adsorption and reaction in successive ionic layers on glass substrates. In this work, they found that the control of Ba doping rate from 0 % to 6 % influences the morphological and structural properties of CuO thin layers. The images obtained by SEM analysis presented in Fig. 13**(b–e),** revealed that the pristine CuO photocathode (Fig. 13**b)** exhibited a rough morphology with a haphazard distribution of multiform nanoparticles and an average size of approximately 195 nm [164]. After incorporation of Barium with different doping rates, there is the formation of numerous nanoclusters containing lots of aggregates and CuO nanoparticles accumulations as well as the average size was diminished from 195 to 100 nm when the Ba doping rate increases from 2 % to 4 %. This was justified by the effect of Ba^{2+} ions consuming OH^- ions and thus decreasing the rate of growth, which leads to more small grains. In the case of the 6 % Ba-doped CuO photocathode **(**Fig. 13**e)**, the film contained numerous holes between nanoparticles with only a small amount of surface still not covered, probably owing to unfinished growth of the grains [164]. Fig. 13**(f–h)** gives the optical results of the doped and undoped photocathodes. According to the Figures, the 2 % Barium doped films exhibit the broadest absorption band which extends in the visible range from 400 to 800 nm and which is due to the electronic transition from the 2p orbital (valence band) of the O^{2-} ions to the 3d;4 s orbital (conduction band) of the copper ions. It is noted that the appropriate gap energy (1.35 eV) was achieved by the 2 % doped films which implies that a greater number of photons may be absorbed through this film, which can greatly enhance the photocatalytic production of hydrogen [164]. Fig. 13**(i)** displays the photocurrent density measurements of the doped and undoped films, it is clearly observed that the 2 % doping exhibited the best photocurrent density (17 mA/cm²) that is 3.5 times higher than that of the pristine CuO photocathode (4.8 mA/cm²), and which is in good accordance with the optical results. Furthermore, the 2 % doped CuO photocathode exhibited high stability towards photocorrosion (Fig. 13**j**) which was justified by the fast electron transfer from the 2 % Ba doped CuO layer surface into the electrolyte and the reduced electron-hole recombination. The number of moles of hydrogen generated by this photocathode (CuO/Ba 2 %) was 5.1 mmol/cm² for 400 s [164].

2.4. Cobalt based oxides photo-electrocatalysts

2.4.1. Morphological handling

In the last few years, nanostructured materials have become very interesting in the field of electrocatalytic HER, as they normally exhibit a higher surface area compared to bulk materials, thus revealing additional active sites [165]. A range of nanostructured Co_3O_4 photoelectrodes were successfully fabricated and applied for electrocatalytic HER, for example 0D Co_3O_4 nanocrystals [166], 1D nanofibers [167] and 2D layer [168], 3D sphere networks [169]. George et al. [167], were reported to have engineered Co_3O_4 nanofibers using a sol-gel supported electrospinning process with subsequent calcination under various temperatures. It was found that Co_3O_4 nanofibers that were calcined in 773 K showed the highest HER electrocatalysis efficiency under 1 M KOH solution, which may be mostly ascribed to the larger surface area and smaller size of the particles. Zhang et al. [168], indicated that the controled oxygen vacancy tailoring of Co oxide-based materials might be key to enhance the performance of hydrogen evolution reaction under alkaline conditions [168]. By using a solid-phase fusion technique as well as modifying the reaction temperature, a layer of Co_3O_4 with controled oxygen vacancy on Ni foil has been obtained [168]. As illustrated in Fig. 14**(a)** in comparison to both low and high oxygen va-

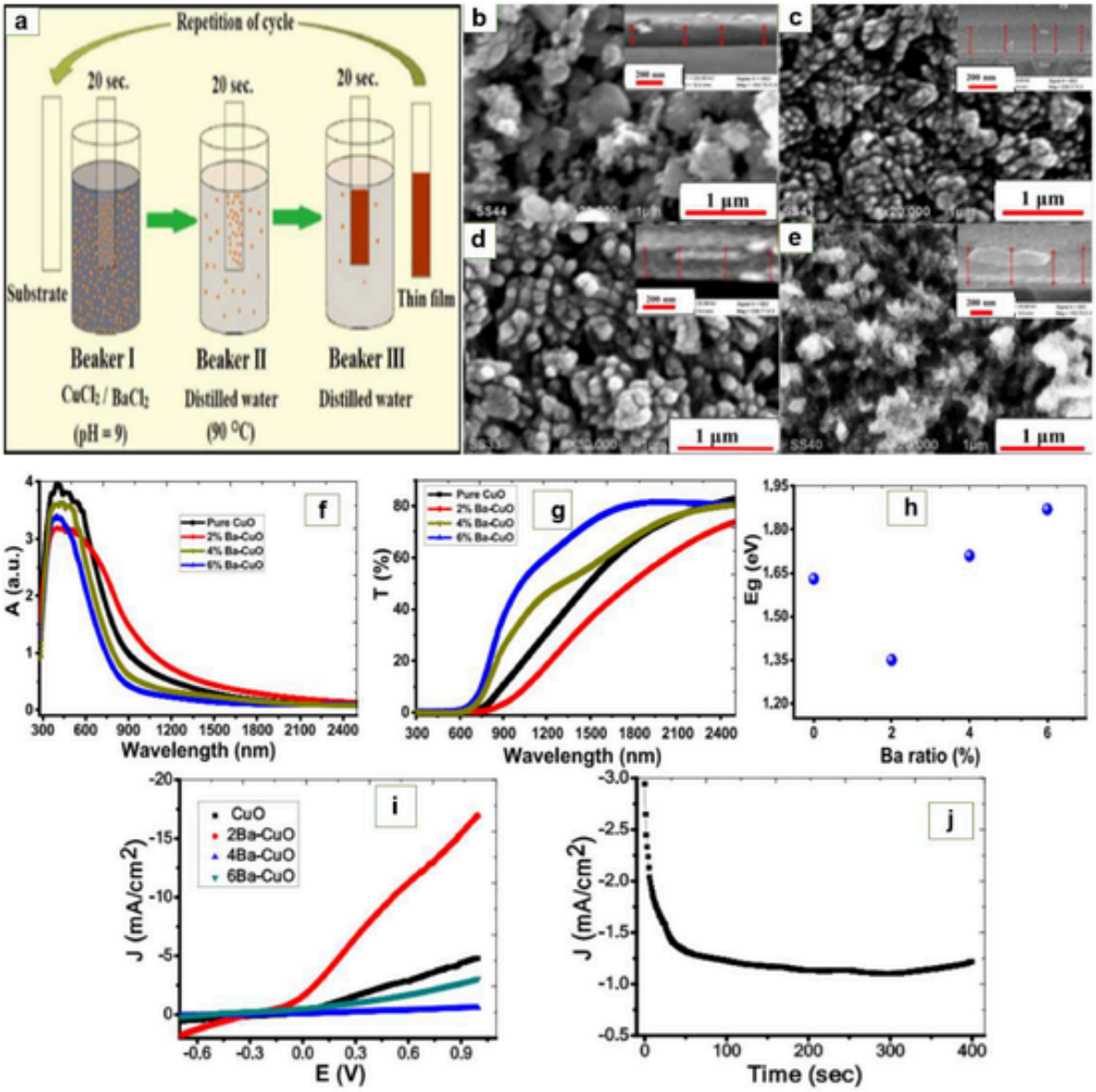

Fig. 13. (a) SILAR procedure for coating Ba-doped CuO thin layers. SEM images of (b) pristine CuO, (c) 2 % Ba-doped CuO, (d) 4 % Ba-doped CuO and (e) 6 % Ba-doped CuO. Spectrum of absorption (f) and transmittance (g), gap energy (h) of pristine and Ba-doped CuO photocathodes. (i) Linear sweep voltammetry (LSV) of Ba/CuO and CuO thin films. (j) Photocurrent density versus exposure time in white lighting irradiation with 2 % Ba-doped CuO photocathode. Reproduced from [164]. Copyright 2020, the Journal of Physical Chemistry C.

cancy amount Co_3O_4 samples, the medium oxygen vacancy amount Co_3O_4 layer (32 %, M-Co_3O_4) needed a very low overpotential value of 203 mV to reach −100 mA/cm² within 1 M KOH at a scanning rate of 1 mV/s. This higher electrocatalytic efficiency for HER may be exemplified by the fact that the M-Co_3O_4 electrode exhibited the lowest slope values of Tafel and the resistance of charge transfer (Rct) (Fig. 14**b** and **c**) [168]. Moreover, these properties might promote catalytically active intermediary adsorption in order to accelerate the kinetics of HER reaction. As a result, it was found that electrodes mass activity (32 %, M-Co_3O_4) was −2.12 A/g which was considerably greater than the activity of 45 %, H—Co_3O_4 (1.21 A/g) and 22 %, L-Co_3O_4 (0.89 A /g)[168]. This was confirmed by the Co 2p spectrum of the M-Co_3O_4 photocathode (Fig. 14**d**), which indicates that the electronic structure for the Co metallic center was suitable for the adsorption of catalytic intermediate [168]. Similarly, Jian et al. [170], engineered a flower-shaped Co_3O_4 photoelectrode having an abundance of oxygen vacancies through an easy hydrothermal approach. Morphological analyses (Fig. 14**e and f**) have revealed that Co_3O_4 retained a nanoflower structure with a thickness of 18 nm [170]. Based on BET measurement (Fig. 14**g**), Co_3O_4 nanoflowers (NFs) exhibited a higher specific surface of 84 m²/g and a lower mean pore size by ~ 4.4 nm when compared to commercially available Co_3O_4 nanoparticles (NPs), thus providing additional active sites throughout the catalytic pathway [170]. The XPS results presented in Fig.14**h** showed that the existence of excess Co^{2+} content inside the Co_3O_4 nanoflowers might contribute to the formation of oxygen vacancies at the electrocatalyst surface, furthermore Co^{2+} was considered to be active sites for catalyzing the OER operation. Thanks to their uniform morphology and suitable electronic structure together with abounding oxygen vacancies, the Co_3O_4 nanoflowers show improved OER and HER capabilities with respect to the commercial Co_3O_4 NPs (Fig.14**i and j**) [170]. Moreover, they consistently show excellent catalysis with no noticeable decrease in potential during 9 days (Fig. 14**k**). The superiority of Co_3O_4 nanoflowers was theoretically explained by the availability of oxygen vacancies which stim-

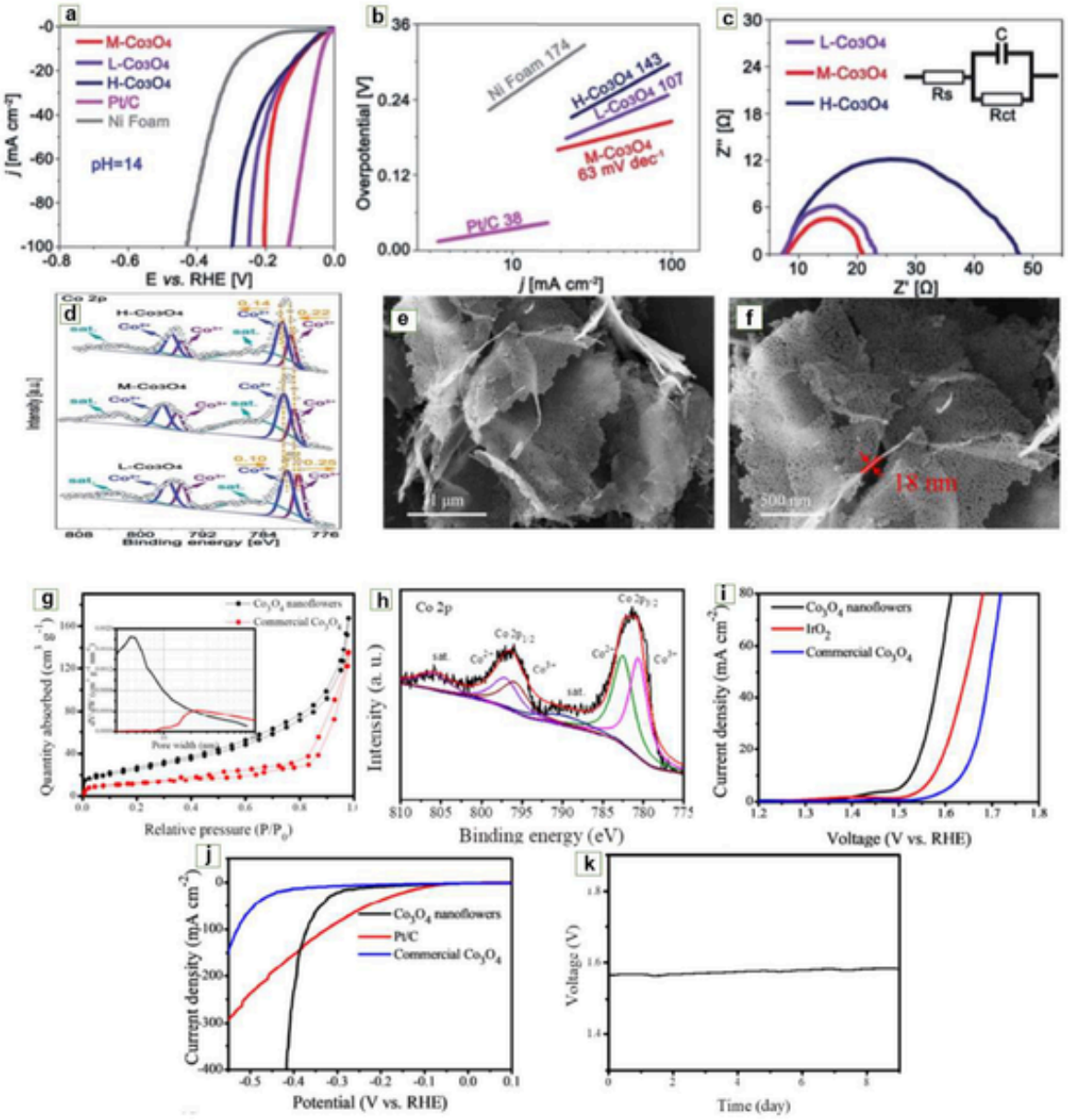

Fig. 14. (a) HER polarization plots in 1.0 M KOH saturated with N_2. (b) Tafel graphs and (c) Nyquist graphs of L-Co_3O_4, H—Co_3O_4 and M-Co_3O_4. (d) XPS spectrum of the Co 2p domains of L-Co_3O_4, H—Co_3O_4 and M-Co_3O_4 after HER process. Reproduced from[168]. Copyright 2019 Journal of Materials Chemistry A. (e-f) SEM pictures showing the Co_3O_4 nanoflowers (NFs). (g) Nitrogen adsorption/desorption isotherms and plot of pore size distribution computed through the BJH formula of Co_3O_4 (NFs) and commercial Co_3O_4 (NPs). (h) XPS spectrum of the Co 2p of Co_3O_4 (NFs). (i-j) The OER and HER LSV polarization plots. (k) stability test of Co_3O_4 NFs at a fixed current density from 10 mA /cm². Reproduced from [170]. Copyright 2020 Electrochimica Acta.

ulates the adsorption of H_2O onto the electrocatalyst surface, hence the surface with more oxygen vacancies becomes considerably activated [170].

2.4.2. *Heterojunctions strategy*

Building a heterojunction is a feasible approach to improve the electrocatalytic and photoelectrocatalytic properties of the Co_3O_4 material for both HER and OER. In the bibliography, the Co_3O_4 material has been compounded with numerous other materials, like metal oxide [171,172], carbon [173,174] and some other materials [175,176]. A number of metal oxides have been associated with Co_3O_4 materials in order to obtain improved electrocatalytic performances for the hydrogen evolution reaction and oxygen evolution reaction [177]. As an example, Aneela and co-workers [178], found that the integration of copper oxide (CuO) into the nanowire precursor (Co_3O_4) activated the cobalt oxide compound and achieved performance similar to the better HER catalysts that were reported under alkaline conditions. Scanning electron microscopy analysis (Fig. 15**a and b**) showed that the inclusion of copper has not changed the morphology of Co_3O_4 but it has modified the upper surface of the nanowire which has become finer and sharp. This property provides a higher surface area which allows for a large area of contact with the electrolyte and consequently speeds up the HER kinetics [178]. When evaluated as an electrode for HER, the low overpotential and excellent stability were attributed to the synergistic effect of the Co_3O_4/CuO hybrid as well as its uniform structure (Fig. 15**c**). The current density recorded for this electrode was −10 mA/cm² at a potential value of −0.288 V vs RHE. Furthermore, the EIS results (Fig. 15**d**) indicated that the hydrogen evolution reaction is

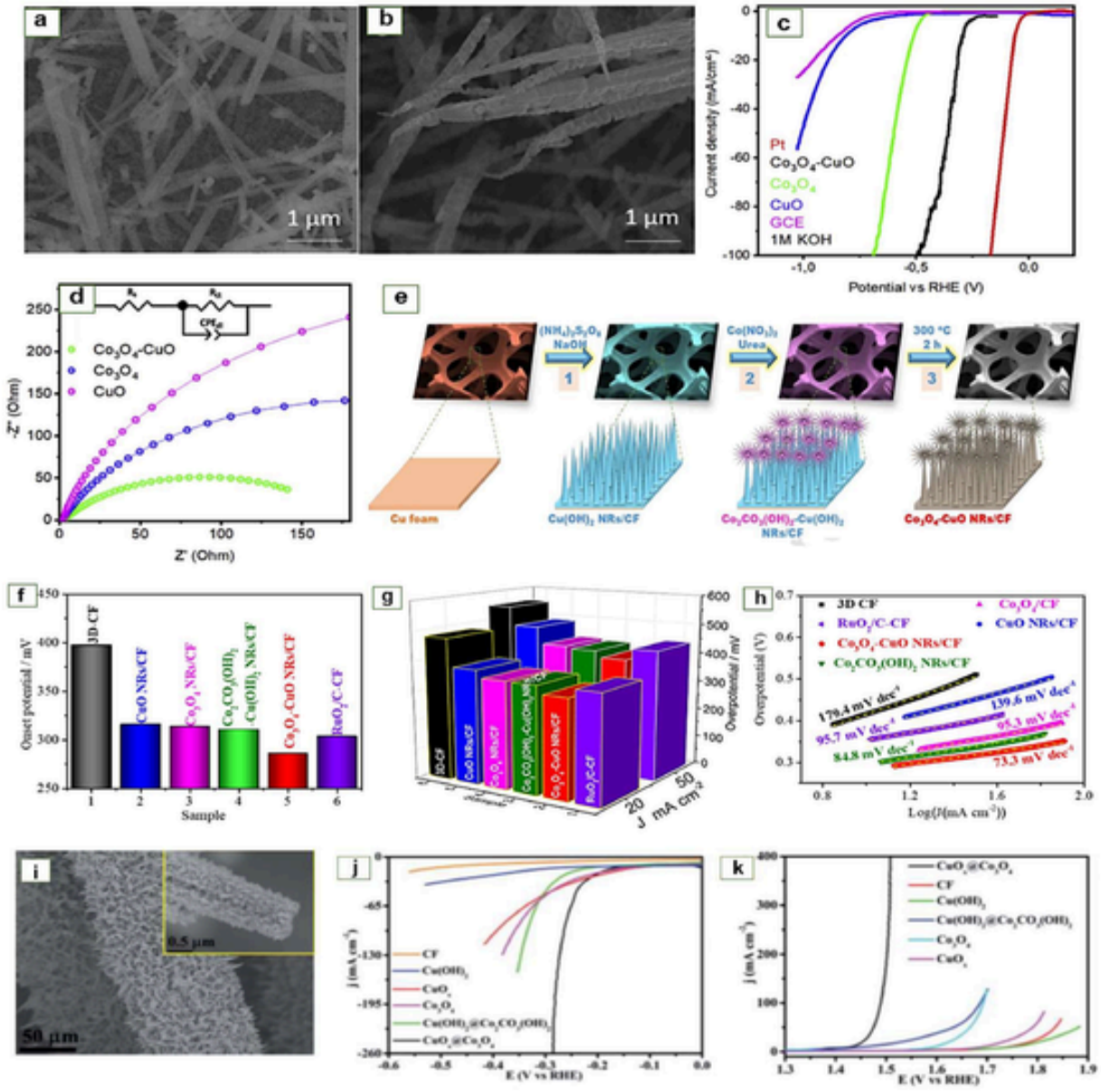

Fig. 15. (a and b) SEM images of pristine Co_3O_4 and Co_3O_4/CuO heterojunction. (c) LSV polarization plots for various catalysts with a scan rate of 5 mV/s under 1 M KOH conditions. (d) Nyquist graphs for HER at an applied potential value of −0.3 V versus RHE. Reproduced from [178]. Copyright 2019 Journal of Hydrogen Energy (e) Schematic representation of the manufacturing procedure of Co_3O_4/CuO NRs/CF. (f and g) Onset potential and overpotential values for diverse catalysts. (h) Tafel plots for diverse catalysts. Reproduced from [179]. Copyright 2020 Journal of Electroanalytical Chemistry. (i) SEM images of CuO_x@Co_3O_4 NRs/CF composite. (j and k) LSV plots of CuO_x@Co_3O_4 for the HER and OER. Reproduced from [171]. Copyright 2018 Journal of Materials Chemistry A.

found to be very favorable on the surface of the Co_3O_4/CuO composite owing to the lower charge transfer resistance in comparison with virgin Co_3O_4 and CuO [178]. On the other hand, Nguyen et al. [179], through three step chemical synthesis pathway (Fig. 15**e**), succeeded in developing a new heterostructured anode that contained snowflake-like Co_3O_4 compounds deposited onto the extremity of CuO nanorods networks that were directly synthesized on a 3D Cu foam surface. The resulting Co_3O_4/CuO NRs/CF heterostructure was utilized as a successful electrocatalyst to accelerate the oxygen evolution reaction under alkaline environment. As a result of their mesoporous properties (pore size~30–32 nm), the Co_3O_4/CuO NRs/CF heterostructure displayed a great active electrochemical surface area which leads to a considerably enhanced electrocatalytic activity. This translates into a low onset potential of 285.6 mV vs. RHE (Fig. 15**f**) as well as a weak overpotential of 340 mV in order to attain a current density value of 20 mA/cm²(Fig. 15**g**) [179]. The tafel curve (Fig. 15**h**) suggest that the oxygen evolution reaction is greatly favored at the surface of the Co_3O_4 -CuO NRs/CF heterostructure due to the lowest Tafel slope of 73.3 mV.dec^{-1}. In comparison with the noble material RuO_2, the catalyst synthesized by this team showed an excellent stability, resulting in a current retention of 95.3 % compared to RuO_2 (85.2 %) for 30 h at a constant potential of 1.6 V vs RHE [179]. The use of catalysers with great activity and stability for the reactions HER and OER is required for effective water splitting, as these two reactions contribute significantly in overall yield. For this reason, Zho et al. [171], employed a three-step pathway for growing hierarchical CuO_x@Co_3O_4 nanorods on a 3D copper foil and which were studied as a bifunctional electrocatalyst for both HER and OER reactions. The catalyseur's hierarchical structure (Fig. 15**i**) as well as the synergistic effects created between the Co_3O_4 shell and the CuO_x core, besides its great electrochemical surface were the major factors that allowed the CuO_x@Co_3O_4 NRs/CF catalyst to exhibit substantial catalytic activity. They were reflected by a low overpotential value of 242 mV for HER

(Fig. 15**j**) and 240 mV for OER (Fig. 15**k**) from a current density by 50 mA/cm² as well as small Tafel slopes of 61 and 46 mV/dec, respectively [171]. A Co_3O_4/reduced graphene oxide (rGO)/$BiVO_4$ photoanode device was prepared to obtain outstanding PEC water splitting efficiency. rGO, acting as a metal, extracted holes from the un-derlying $BiVO_4$ light-absorbing layer while Co_3O_4 played the function of a catalyst for the OER. The photocurrent produced using the Co_3O_4 and rGO catalytic layers on $BiVO_4$ was approximately 93 % of that produced in an electrolyte containing a hole scavenger, demonstrating the crucial role of the rGO and Co_3O_4 materials in the strong PEC water splitting capability of the Co_3O_4/rGO/$BiVO_4$ photoelectrode [180].

2.4.3. *Doping technology*

Wang et al. [181], by using a low temperature heat treatment and varying the quantity of NaH_2PO_2 which served as a source of phosphorus, succeeded in manufacturing a bifunctional catalyst of $P_{8.6}$-doped Co_3O_4 nanowires on nickel foam (Fig. 16**a**) [181]. They showed by means of XPS analysis (Fig. 16**b**) that the low intensity of lattice oxygen in $P_{8.6}$-Co_3O_4 /NF compared to pristine Co_3O_4 was due to the partial exchange of the lattice O with the P atom within Co—O. Furthermore, the appearance of the P ($2p_{1/2}$ and $2p_{3/2}$) peaks (Fig. 16**c**) confirmed that phosphorus has been doped successfully in Co_3O_4 resulting in an increase in the number of Co^{3+} and consequently more empty d-orbitals capable of adsorbing H atoms as well as OH groups [181]. This adsorption was considered necessary to enhance the Volmer step kinetics in the HER process thereby decreasing the Tafel slope of the HER operation upon P-doped Co_3O_4 (Fig. 16**d**). In the step determingin the potential of oxygen evolution reaction (OER), the DFT calculations (Fig. 16e and f) confirmed the favorable influence of the P-doping on the oxygen evolution reaction which was evideced by obtaining a signifi-

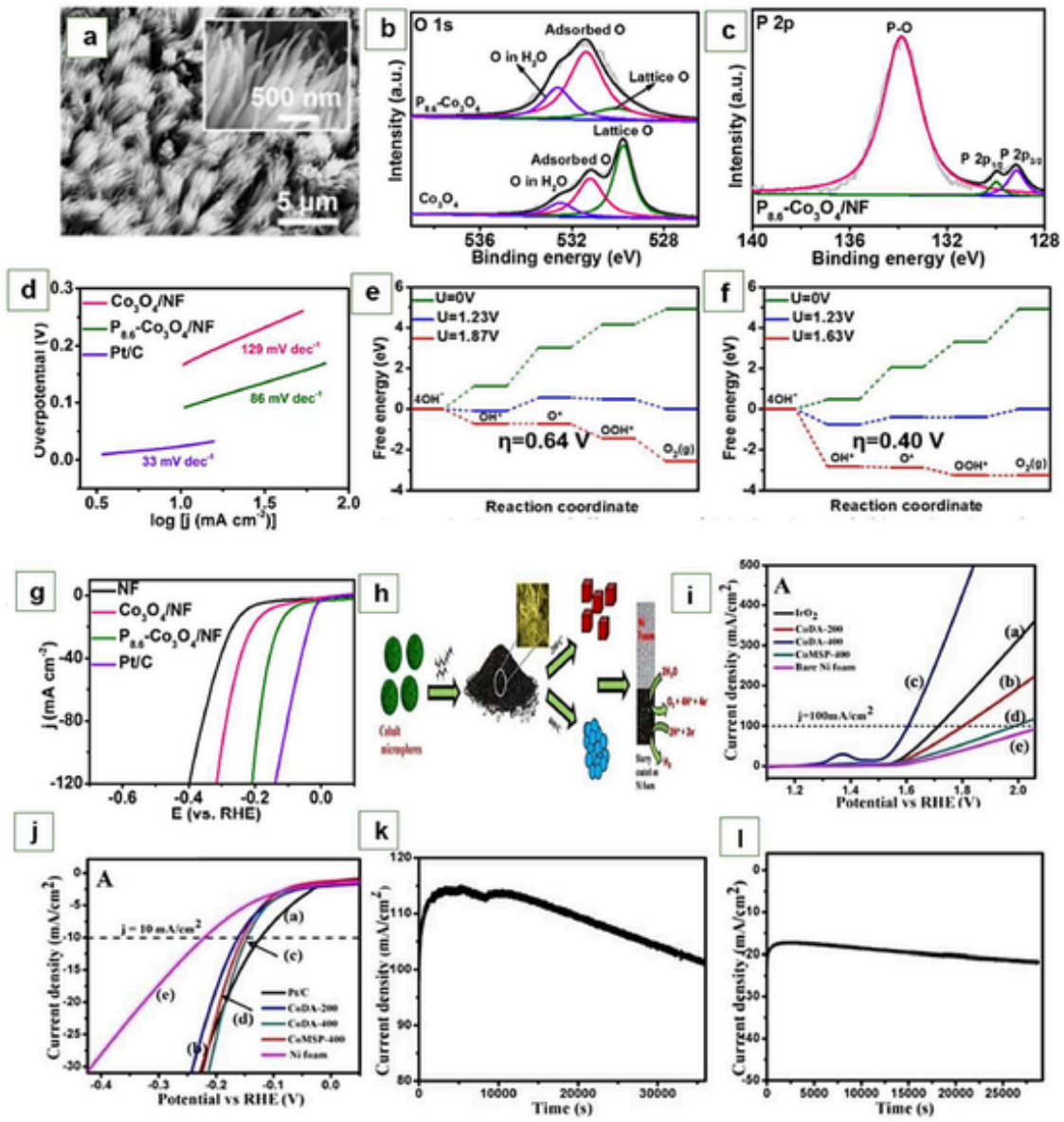

Fig. 16. (a) SEM images of the developed $P_{8.6}$-Co_3O_4/NF electrode. (b and c) XPS spectrum of $P_{8.6}$-Co_3O_4/NF in the O_{1S}, P_{2p} regions. (d) Tafel plots of Pt/C, $P_{8.6}$-Co_3O_4/NF and Co_3O_4/NF for HER process. (e-f) Diagrams of free energy for OER upon Co_3O_4 and P-Co_3O_4 respectively. (g) LSV graphs of $P_{8.6}$-Co_3O_4/NF in comparison with various catalysts for HER at 2 mV/s. Reproduced from [181]. Copyright 2018 ACS Catalysis. (h) Schematic illustration of the preparation process of the N-doped Co_3O_4 catalyst. (i and j) LSV plots displaying the OER and HER catalytic activity of several materials. (k-l) Stability investigation of CoDA-400 by employing amperometry for analyzing the duration of electrocatalytic activity of OER at 1.608 V and HER at −0.183 V versus RHE. Reproduced from [182]. Copyright 2018 ChemistrySelect.

cantly smaller change in free energy (1.63 V) compared to pristine Co3O4 (1.87 V). They also noted that the generation of the O_2 molecules were derived from the OOH* intermediate with a theoretical overpotential of 0.40 V for P-Co_3O4 and O* intermediate with a theoretical overpotential of 0.64 V for pristine Co_3O_4 [181]. On the other hand, the elaborated $P_{8.6}$-Co_3O_4/NF also displayed a significant electrocatalytic activity for HER which was reflected by a low overpotential 97 mV compared to NF (231 mV) and Co_3O_4 /NF (165 mV) (Fig. 16**g**) [181]. In the same years Mers and co-authors[182], have employed dopamine as source of nitrogen to develop a bifunctional electrocatalyst deposited on nickel foam (N—Co_3O_4/NF) [182]. Depending of the annealing temperature, which was between 200 °C and 400 °C, they were able to modify the morphology of the catalyst into cubes (CoDA200) and spherical particles (CoDA400) (Fig. 16**h**). They showed that the varying structural morphology allows to influence the electrocatalytic performance of each catalyst particularly the sample treated at 400 °C (CoDA400) compared to the other catalysts, demonstrating a greater bifunctional activity for both HER and OER processes which was manifested by a low overpotential of 378 mV to achieve a density of 100 mA/cm² for OER (Fig. 16**i**) and 147 mV to reach a density of 10 mA/cm² for HER (Fig. 16**j**) [182]. Additionally, this particular electrocatalyst presents a noticeable stability in the long term for both OER and HER (Fig. 16**k and l**) respectively [182].

On the other hand, the doping using metallic elements was also employed for improving the electrocatalytic HER and OER properties of Co_3O_4 [183–185]. Recently Zhao et al. [186] were successful in developing a bifunctional electrocatalyst based on molybdenum (Mo)-doped cobalt oxide sustained on nitrogen-doped carbon (x%Mo-Co_3O_4/NC, whereby x% denotes the molar ratio of Mo/Co) [186]. They found than when x equaled 4 %, the grain size becomes smaller which gives rise to a bigger electrochemically active surface (Fig. 17**a**). Compared to the Co_3O_4/NC and (2 %, 6 %)Mo-Co_3O_4/NC electrodes, the 4 %Mo-Co_3O_4/NC electrode in 1 M potassium hydroxide solution had the lowest overpotentials that was 276 mV and 91 mV for OER and HER respectively (Fig. 17**b and c**) [186]. The positive impact of Mo doping was confirmed by the superior durability of the 4 %Mo-Co_3O_4/NC electrode at 10 mA/cm² in comparison with the commercially available noble metal electrodes (IrO_2||20 % Pt/C) (Fig. 17**d**) [186]. In another work Xiong et al. [183], developed a new strategy consisting of two stages that leads to ultrathin nanosheets of Mo-doped Co_3O_4 supported on a nickel substrate (Fig. 17**e**) [183]. Due to their ultrathin property, the developed electrocatalyst with an amount of Molybdenum of 0.4 mmol displayed a higher specific surface area and exposed higher percentage of active sites leading to a lower Tafel slope of 98 and 83.7 mV/dec for HER and OER respectively (Fig. 17**f and g**) [183]. Furthermore, the combined 0.4Mo-Co_3O_4|| 0.4Mo-Co_3O_4 electrolyser (Fig. 17**h**), demonstrated a current density value of 10 mA/cm² at 1.64 V, together with a high stability for a duration of 12 h **(**Fig. 17**i)** [183]. On the other hand, the H_2 production may happen via the transfer of free electrons to H_2O molecules, as depicted in Fig. 17j. The Na_2SO_4 molecules, with the help of OH^-, receive holes from the (Fe, Ni) doped Co_3O_4 photo-electrode to generate O_2 at the Pt counter electrode. The produced electrons reduce H_2O molecules, and interact with hydrogen ions to form hydrogen atoms ($4H^+ + 4e^- \rightarrow 2H_2$ ($E^o_{H+/H2} = +0.00$ VNHE)), while water oxidation takes place at the Pt electrode, which acts as the anode for the PEC cell ($2H_2O + 4h^+ \rightarrow 4H^+ + O$ ($E^o_{H2O/O2} = -1.229$ VNHE)) [187].

2.5. Zinc based oxides photo-electrocatalysts

2.5.1. Morphological handling

Zinc oxide nanomaterials, especially ZnO (n-type semiconductor), were widely investigated in water separation thanks to their cheap cost, eco-friendly nature and their earthly abundance as well as outstanding electron mobility, they also feature an energy band structure (band gap ~3.3 eV) with optoelectronic characteristics resembling those of TiO_2 [188–190]. Nevertheless, the use of ZnO for solar water splitting is actually hampered by certain natural restrictions of this material, as an example, there is a weak photocatalytic performance of ZnO on account of its poor absorption of visible light and a weak quantum photocatalytic yield [191]. Following a discussion of some overall material properties, this section outlines the various approaches that were taken to boost further the capabilities of ZnO for use in photo-electrochemical processing. In this context, ZnO nanoflowers grown from zinc acetate hydrolysis in the presence of DMF with 50 nm average size and a band gap of 3.25 eV have demonstrated a photocurrent density of 0.39 mA/cm² at 0.6 V relative to Ag/AgCl as well as an efficient separation of photo-generated electron-hole pairs and a rapid charge transfer interfacial process [192]. On the other hand, Gill et al. [193], have synthesized vertically aligned ZnO nanorods by employing a hydrothermal method, with the addition of varying quantities of ammonia to the solution to monitor the forming of the ZnO rod. Based on the I-V I-V electrochemical analysis, a considerable photocurrent has been registered for sample Z3 (ZnO with 0.7 M of ammonia), with an evolution of the short circuit current (J_{sc}) from 0.60 mA/cm² for Z1 (ZnO with 0 M of ammonia) to 0.74 and 0.81 mA/cm² in Z2 (ZnO with 0.4 M of ammonia) and Z3, respectively. Furthermore, Zhifeng et al. [130], proved that based on a sol-gel immersion deposition method which was followed by changing the resting time of the samples that were immersed in a growth solution containing zinc acetate dihydrate and hexamethylenetetramine for 5, 10, 15 days. Four diverse morphologies of ZnO nanostructures that displayed different PEC performances could be formed, including nanowires and nanorods (5days), nanotubes (10-days) and nanodisks at the end. Photocurrent density measurements exhibited an upgrade from nanodisks to nanorods/nanowires and nanotubes, this outstanding PEC performance of the nanotubes was explained by their tubular structure that leads to an intensified light absorption resulting in a high generation of electron-hole pairs that was beneficial for a better PEC water splitting. As one example, Ming et al. [194], constructed a strongly photoactive photoanode for PEC water splitting based on three-dimensional (3D) inverse opals-like Zno nanostructures. The photocurrent density achieved using the electrode was registered as 0.9 mA/cm². Furthermore, Qiang et al. [195], also carried out the hydrothermal growth of ZnO nanobranches radially on seed nanocrystalline ZnO nanofibers, resulting in the fabrication of the branched ZnO nanostructures of the "caterpillar" type. Based on these engineered nanostructures, a photo-to-hydrogen conversion rate of 0.165 % and a highest photocurrent density of 0.524 mA/cm² at +1.2 V (versus Ag/AgCl) has been found. Currently, high attention has been paid to the hierarchical structure for water splitting owing to its elevated surface area, which augments the interface area between the electrolyte and the electrodes. Using a hydrothermal technique with FTO glass substrates made it possible to prepare three kinds of ZnO hierarchical film morphology, including vertically aligned nanorods (NR), nanorods interconnected by thin nanosheets (NR@TN) and nanorods interconnected with dense nanosheets (NR@DN). The photoelectrochemical outcomes revealed that the highest photocurrent density and lower onset potential registered with NR@TNs, those noteworthy PEC achievements may be ascribed to the thin nanosheets and the improved ability of light capture as well as the enhancement of the semiconductor/liquid interfaces that was advantageous for an effective charge transfer/transport [196]. From the early stages of the development of PEC water splitting, the solid–liquid interface attracted a considerable degree of interest. As illustrated in Fig. 18, when the n-type ZnO comes into direct contact with the electrolyte, charge transfer happens at the electrode/electrolyte junction owing to the positional difference between the potential of the redox pair in the electrolyte and the Fermi level of the ZnO. This charge transfers changes the charge partitioning at the interface. Hence, at the electrolyte surface, an electrical double layer is created, comprising a Gouy–Chapman layer and a

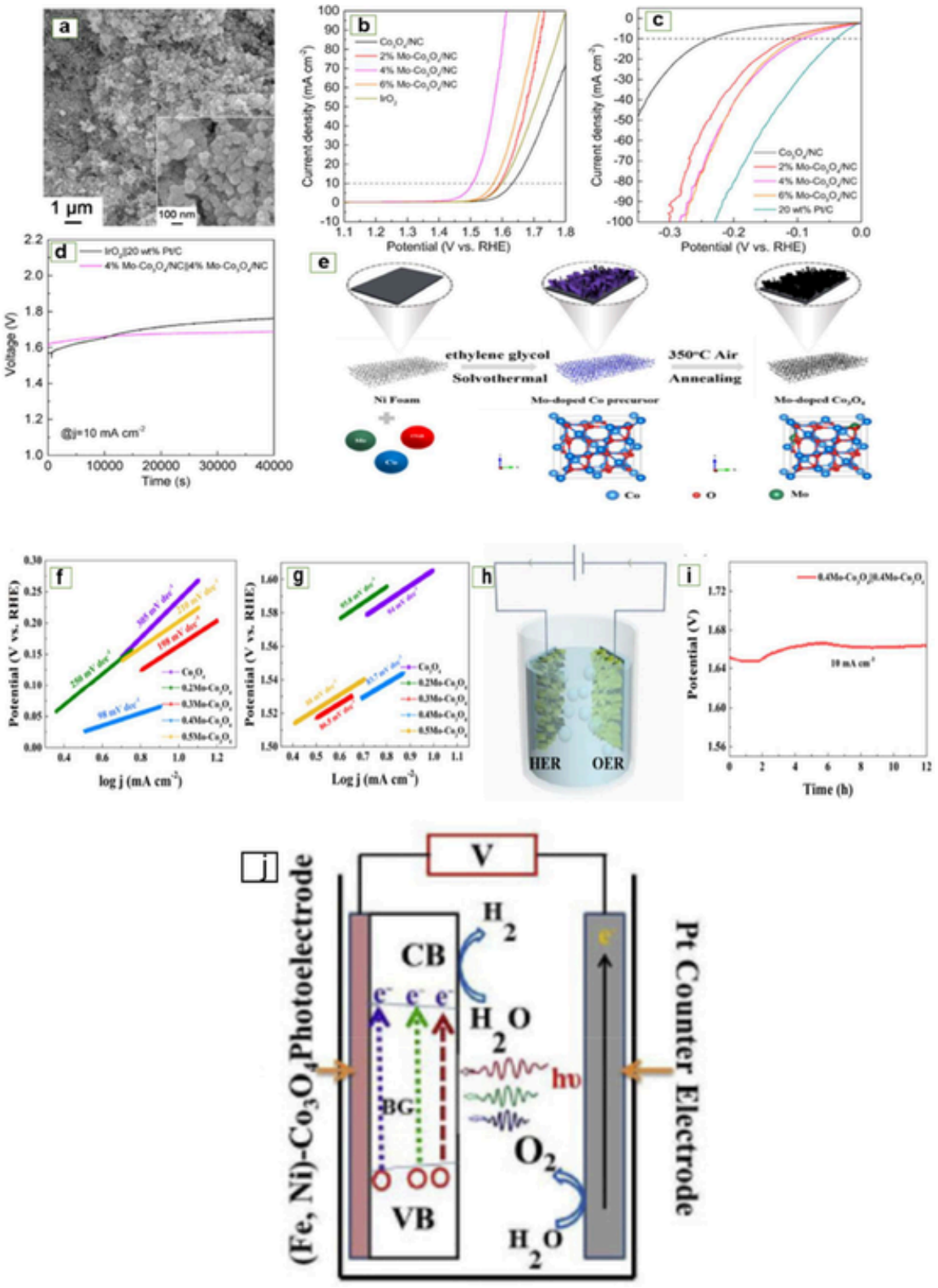

Fig. 17. (a) SEM images of 4 %Mo-Co_3O_4/NC. (b and c) LSV curves of OER and HER for4 %Mo-Co_3O_4/NC compared to different electrocatalysts. (d) Chronopotentiometric graphs at 10 mA/cm² of the overall water splitting for the 4 %Mo-Co_3O_4/NC||4 %Mo—Co_3O_4/NC cell in comparison with IrO_2|||20 wt% Pt/C in 1 M KOH solution. Reproduced from [186]. Copyright 2021 Journal of Hydrogen Energy. (e) Schematic of the Mo-doped Co_3O_4 synthesis process. (f-g) Tafel plots of 0.4Mo—Co_3O_4 in comparison to various electrocatalysts for HER and OER respectively. (h) A schematic showing the 0.4Mo—Co_3O_4|0.4Mo—Co_3O_4 electrolyser. (i) Chronopotentiometric graphs of 0.4Mo—Co_3O_4||0.4Mo—Co_3O_4 electrolyser at 10 mA/cm². Reproduced from [183]. Copyright 2021 Journal of Col-

Fig. 17 .—*continued*
loid and Interface Science. (j) Schematic representation of PEC water splitting with (Fe, Ni) Co_3O_4 photo-electrode. Reproduced from [187]. Copyright 2021 International Journal of Hydrogen Energy.

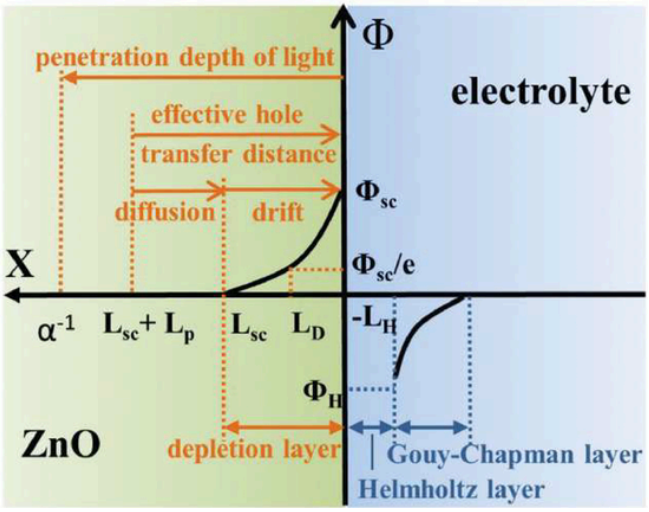

Fig. 18. The energy band diagram of the interface between the electrolyte and ZnO photo-anode. Reproduced from[198]. Copyright 2019 Advanced Functional Materials.

Helmholtz layer. On the ZnO surface, the upward bending of the band edges seems to create an electric field, with the degree of bending depending on the initial difference between the electrolyte potential and the Fermi level of the ZnO. Therefore, the photo-induced charge carriers may be separated effectively and migrate under such an electric field across the solid-liquid interface, allowing subsequent oxidation and reduction reactions for water splitting. For an n-type ZnO semiconductor, the thickness of the space charge layer is commonly determined using the following equations [197].

$$L_{SC} = L_D\left[\frac{2q\left|\Phi_{SC}\right|}{kT}\right]^{1/2} = L_D\left[\frac{2q\left(V - V_{fb}\right)}{kT}\right]^{1/2}$$

$$L_D = \left[\frac{\varepsilon_0 \varepsilon kT}{q^2\left(n_0 + p_0\right)}\right]^{1/2}$$

where L_D is the Debye length which has been treated as the characteristic length for potential attenuation (Φsc/e), ε is the relative dielectric constant, ε_0 is the vacuum dielectric constant, T is the absolute temperature in degrees Kelvin, k is the Boltzmann constant, V_{fb} and V are the flat potential and applied bias of the electrodes, respectively. q is the electron charge, p_0 and n_0 are the hole concentrations and the electron of the electrodes, respectively.

In addition, after exiting the depletion layer, the separated charges undergo a diffusion operation, and the hole diffusion length (L_p) before recombination is defined as [199]:

$$L_p = (D\tau)^{\frac{1}{2}} = \left(\frac{\mu k_B T}{q}\tau\right)^{\frac{1}{2}}$$

where τ and D are the lifetime of the minority carrier and the diffusion coefficient, respectively.

2.5.2. Heterojunctions strategy

Recently special attention has been provided to heterojunctions, since these structures would be more likely in utilizing the advantages offered through combination of elements having distinct characteristics, displaying a functional behavior in the interfacial area, as well as enhancing the solar energy conversion via synergetic effects [200,201]. Several research teams around the world have already adopted heterojunction technology (including co-catalysts, plasmonic structures, novel hierarchies, etc.) for developing more effective photoelectrodes. Cai et al. [202], developed a new 3D core-shell nanostructure that was decorated by plasmonic Au NPs. As it can be observed in the SEM images presented in Fig. 19, the ZnO nanorods (NRs) was orthogonal to the ZnO nanosheets (NSs) (Fig. 19**a**), as well as the ZnO NRs-NSs were coated by a fine TiO_2 shell which was formed through liquid phase deposition (Fig. 19**b**), on the other hand the plasmonic Au NPs was in situ formed upon the surface of the ZnO NRs-NSs/TiO_2 via thermal reduction (Fig. 19**c**), [202]. The photocurrent density recorded by this photoelectrode (3D ZnO NSs-NRs@TiO_2-Au) was 1.73 mA/cm² at 1.23 V (Fig. 19**d**), which was 4.33 fold more than those of ZnO nanosheets, while the photoconversion efficiency was 0.48 % which was 4.80 fold more than those of ZnO NSs (Fig. 19**e**), additionally the hydrogen generation ratio was 15.72 mmol/ h.cm² [202]. The obtaining of these improvements was justified by the fine TiO_2 shell which promoted efficiently the charge separation, as well as the Au NPs that acted as photosensitizers to extend the absorption range [202]. Tian et al. [203], successfully decorated the ZnO/$ZnFe_2O_4$ heterojunction with PbS quantum dots to further enhance the charge transport as well as to improve the absorption of visible light of the photoanode. The tuned ZnO/$ZnFe_2O_4$/PbS photoelectrode exhibited considerably improved current density with an outstanding PEC stability. Its photoconversion efficacy was found to be 3.54 and 1.34 fold better than those of ZnO NRs and ZnO/$ZnFe_2O_4$ photoelectrodes respectively. The IPCE of ZnO/$ZnFe_2O_4$/PbS photoanode achieved 54.99 % at 350 nm that was greater compared to ZnO NRs (28.65 %) and ZnO/$ZnFe_2O_4$ (45.18 %) [203]. Lin et al. [204], through an easy consecutive ion exchange reaction approach succeeded in Integer of ZnSe passivation nanoparticles in CdSe/ZnO binary hetero-structure. The CdSe/ZnSe/ZnO photoanode exhibited a significantly enhanced photoelectrochemical capacity to produce hydrogen with a rate of 54.4 μmol/h. Moreover, the photoconversion efficiency was 1.7 % at 0.5 V compared to RHE. The electrochemical impedance measurements (Fig. 19**f**) showed that the CdSe/ZnSe/ZnO photoelectrode possessed the smaller arc radius, hence the charge transport resistance of the photoanode was smaller which leads to an effective photo-generated charge separation. In the CdSe/ZnSe/ZnO heterojunction, the photo-generated electrons in the CB band of CdSe and ZnSe may travel to that of ZnO, and meanwhile, the photo-generated holes at VB of ZnSe and ZnO may migrate to that of CdSe, the separated electrons of CdSe, ZnSe and ZnO have been carried to the Pt electrode for performing the reduction reaction of water and generating hydrogen (Fig. 19**g**) [204]. Recently Li and co-authors [205], via a combination of hydrothermal and chemical bath deposition methods together with the adsorption reaction initiated by an amido bond succeeded in developing a $MoSe_2$/CdS/ZnO (MCZ) tandem Z photoanode with an intertwined ultrathin nanosheet and nanorod structure upon the Au paper electrode intended for PEC splitting water (Fig. 19**h**). For this kind of photoelectrode, they showed that it possessed two integrated electric fields (IEFs) between the interfaces of CdS|$MoSe_2$ and ZnO|CdS (Fig. 19**i**), this generated field acted as a strong driving force to accelerate the separation/transfer of photo-generated carriers. As a result, the photoanode attained an impressive photoelectrocatalytic hydrogen production performance (39,7 μmol /cm².h) with a photocurrent density around 2.4 mA/cm² at 0.3 V. vs RHE and an IPCE of 52 % at 460 nm. In addition to the integrated electric field, these improvements were also attributed to the synergistic effect of the Au substrate's higher electrical conductivity, as well as the Z-scheme mode which permitted the fabricated heterojunction to exhibit a great redox capacity

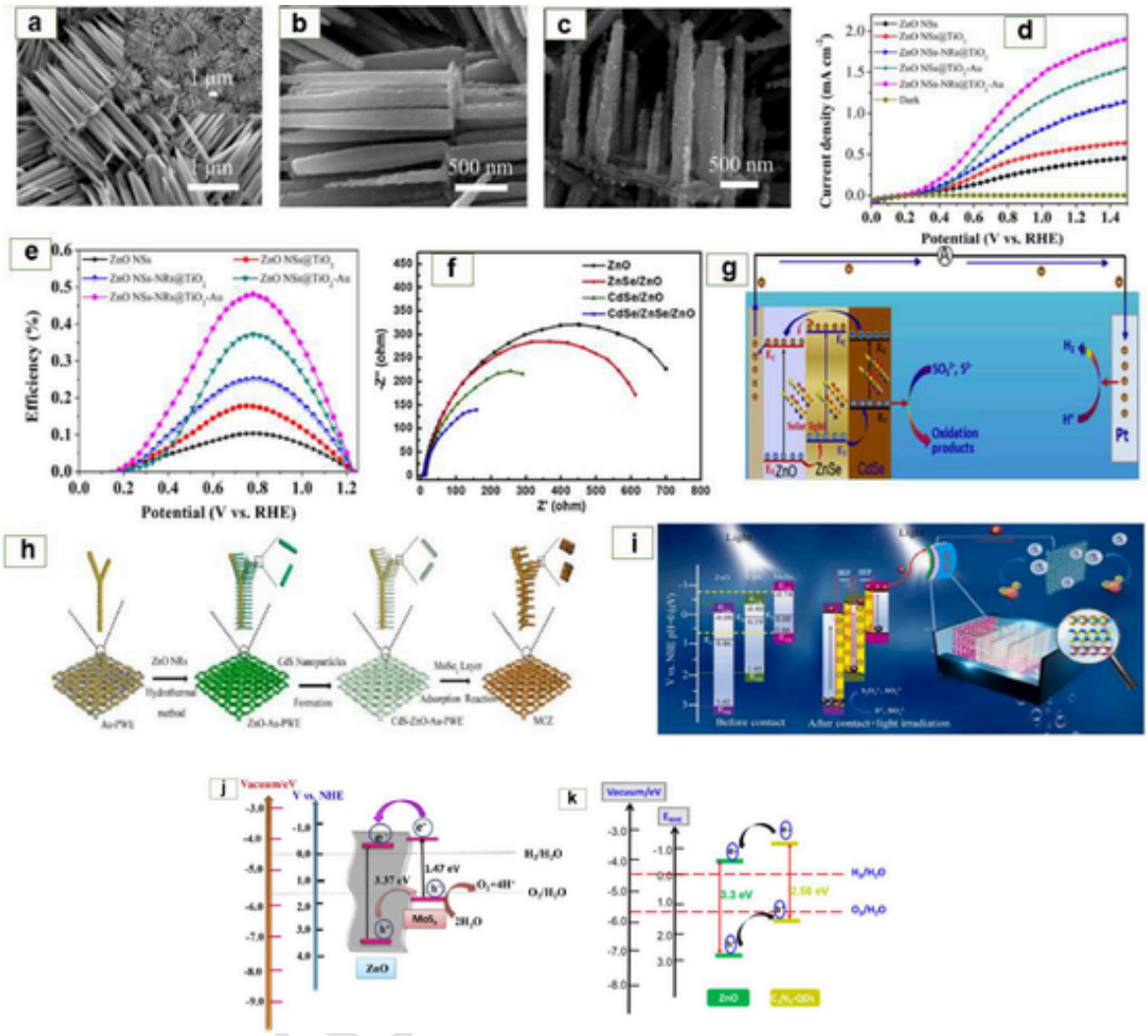

Fig. 19. SEM images demonstrating the morphological progression of the various samples:(a) ZnO NSs-NRs, (b) ZnO NSs-NRs/TiO_2, (c) ZnO NSs-NRs/TiO_2-Au. (d) *J–V* plots for dark and sunlight conditions of different photoelectrodes developed. (e) photoconversion efficiency in function of the bias potential. Reproduced from [202]. Copyright 2021 International Journal of Hydrogen Energy. (f) EIS Nyquist plots of the pristine ZnO, ZnSe—ZnO, CdSe—ZnO and CdSe—ZnSe—ZnO. (g) Charge transfer and process of PEC water splitting of CdSe—ZnS—ZnO photoanode. Reproduced from [204]. Copyright 2021 Colloids and Surfaces A: Physicochemical and Engineering Aspects. (h) Schematic representation of the preparation of $MoSe_2$—CdS—ZnO upon the Au paper electrode. (i) Charge transfer and process of PEC water splitting of $MoSe_2$—CdS—ZnO photoanode. Reproduced from [205]. Copyright 2021 Applied Catalysis B: Environmental. (j) Charge transfer process of ZnO/MoS_x heterostructure. Reproduced from [206]. Copyright 2020 International Journal of Hydrogen Energy. (k) Electron transfer pathway between C_3N_4 and ZnO. Reproduced from [207]. Copyright 2020 ACS Applied Nano Materials.

emphasizing the thermodynamics of the catalytic reaction for water reduction [205].

Sharma et al. [206], succeeded in decorating the surface of ZnO thin sheets using to form the ZnO/MoS_x heterojunction. In addition, the band alignment identified of MoS_x and ZnO was indicative of the creation of the type II heterojunction, which provided an easy separation of the charge- carrier (Fig. 19**j**); The carrier density and current density were 7.4 fold and 3 fold greater as compared to pristine ZnO, respectively. Moreover, the ZnO/MoS_x heterostructure displayed outstanding stability until 1000s in chopped lighting conditions [206]. In another work via electrodeposition method, Mahala et al. [207], reported that sensitizing ZnO nanosheets with carbon nitride (C_3N_4) quantum dots (QDs) led to higher PEC performances. The resulting photoanode (ZnO/C_3N_4-QDs) was made using electrodeposition technique followed by dip coating during varying time periods. The photoanode prepared during 15 min of immersion (ZnO/C_3N_4-15) favored obtaining a high PEC effectiveness with a current density of 0.952 mA/cm² at 0.5994 V. vs RHE and a top photoconversion-efficiency of 0.70 % which was 2.3-fold better compared to pristine ZnO. These enhancements were ascribed to the formation of the kind II heterojunction that facilitated separation of charges, limiting recombination (Fig. 19**k**), as well as the increased carrier density which was almost 2.2-fold better compared to pristine ZnO and the enhanced light absorption as a result of the addition of C_3N_4 [207].

2.5.3. *Doping technology*

In recent years doping technology has been regarded as one of the main approaches employed in order to have PEC-WS devices that are able to efficiently absorb and use the incident photons in order to eventually reach great photoelectrochemical performances. It has been studied in detail the doping of ZnO nanostructures to modify their electrical or optical characteristics [208,209]. Also, the dopants within ZnO have been taken advantage of either as donors or acceptors toward better conductivity as well as delaying carrier recombination, ultimately re-

sulting in an enhanced photocurrent [210]. Various metal elements, including copper, cobalt, iron, aluminum, and chromium, together with nonmetallic elements, like carbon, nitrogen, and chlorine, were successfully integrated in ZnO nanostructures[211]. Tanmoy et al. [212], published a paper on the synthesis of a carbon-doped ZnO core-shell nanorod photoanode via a hydrothermal technique on FTO substrates. The variation of glucose concentrations which was the source of carbon from 0.05 to 0.2 M has been studied. Following the carbon doping, a strong absorption in the UV (300–400 nm) as well as in the visible (400–550 nm) was observed. X-ray photoelectron spectroscopy (XPS) was used to confirm that the doped C mostly occupied the O sites as single C atoms without changing the crystal structure of the ZnO network, and as a consequence of the change in glucose concentrations, the atomic percentage of C doping in the nanorods varied from 5.2, 8.9 % to 16.9 % for the samples of C-ZnO1, C-ZnO2, and C-ZnO3 respectively. As depicted in Fig. 20**(a–f)** the C-ZnO NRs electrodes exhibited a greater photoconversion efficiency as well as improved photoresponse and IPCE relative to undoped nanorods. In particular, the ideal PEC properties were achieved for the prepared C-ZnO2 sample at a glucose concentration of 0.1 M with the achievement of a short circuit current (JSC) of 0.82 mA/cm² and a photoconversion efficiency of about 0.79 % as well as an IPCE under 350 nm illumination was found to be 59.4 %, besides a lower charge transfer resistance and a high stability to photocorrosion and electro-corrosion owing to the existence of a thin carbon film. These enhancements have been ascribed to the narrowing of the band gap and the adapted morphology of ZnO with the inclusion of C [212]. Furthermore, hierarchically porous C-doped ZnO nanoarchitectures have been elaborated using a chemical method on substrates coated with indium-doped tin oxide (ITO). They showed, compared to pristine ZnO, improved photoelectrochemical properties as well as the modification through carbon doping considerably enhances both the light usage and the conversion efficiency within the visible region [213]. Via a solvothermal process, C-doped ZnO ball-in-ball hollow microspheres were synthesized. The addition of ethylene glycol (EG) results in the creation of monolayered hollow spheres that are converted as a function of time into regular ball-in-ball hollow microspheres. This hollow structure and the doping achieved a better absorption and charge separation leading to enhanced photoelectrochemical performance regarding water splitting [214]. Beyond carbon, chlorine has also been employed to upgrade the conductivity and electron mobility of ZnO, also the Oxygen vacancies serve as centers of recombination, therefore *Cl* substituting oxygen vacancy will reduce the rate of charge carrier recombination [215,216]. Sahoo and his team [217], proved that increasing the concentration of chlorine doping on ZnO nanorods provides a surface roughness which assists in greater interaction of incident UV light to achieve significantly enhanced electric field production. Hence, compared to the virgin ZnO NRs, chlorine doping resulted in improved photoresponse and charge separation efficiency owing to the UV light interaction and free electron formation, as well as the reduction of oxygen vacancies. This leads to improved photocurrent density which was then reduced by increasing the concentration of the dopant leading to the decrease of the grain size and the growth of the grain boundaries that participate to the diffusion of the charge carriers. The optimal concentration of added Chlorine was 15 mM which gave a photocurrent density of 2.16 mA/cm² at 1.2 V relative to Ag/AgCl, and a photoconversion efficiency of 57.75 % with outstanding photostability during 12 h of illumination. Henni et al. [218], developed ZnO nanorods doped with Al through electrodeposition method and recorded a steady enhancement of photocurrent ranging of 21 μA up to 58 μA at 1.0 V vs. SCE, as a result of increasing the doping concentration from 0 at.% to 2.0 at.%. This enhancement has been assigned to the improved conductivity of the thin films doped with Al. According to Xu et al. [219], the performance improvement has been assigned to increasing the carrier rate, although defects generation and electron diffusion may decrease their mobility for greater concentrations of doping. The aluminium-doped zinc oxide (AZO) inverse opal shells (IOS) and tin disulfide (SnS_2) core-shell composite (AZO IOS/SnS_2) photoelectrode for PEC water splitting has been fabricated using atomic layer de-

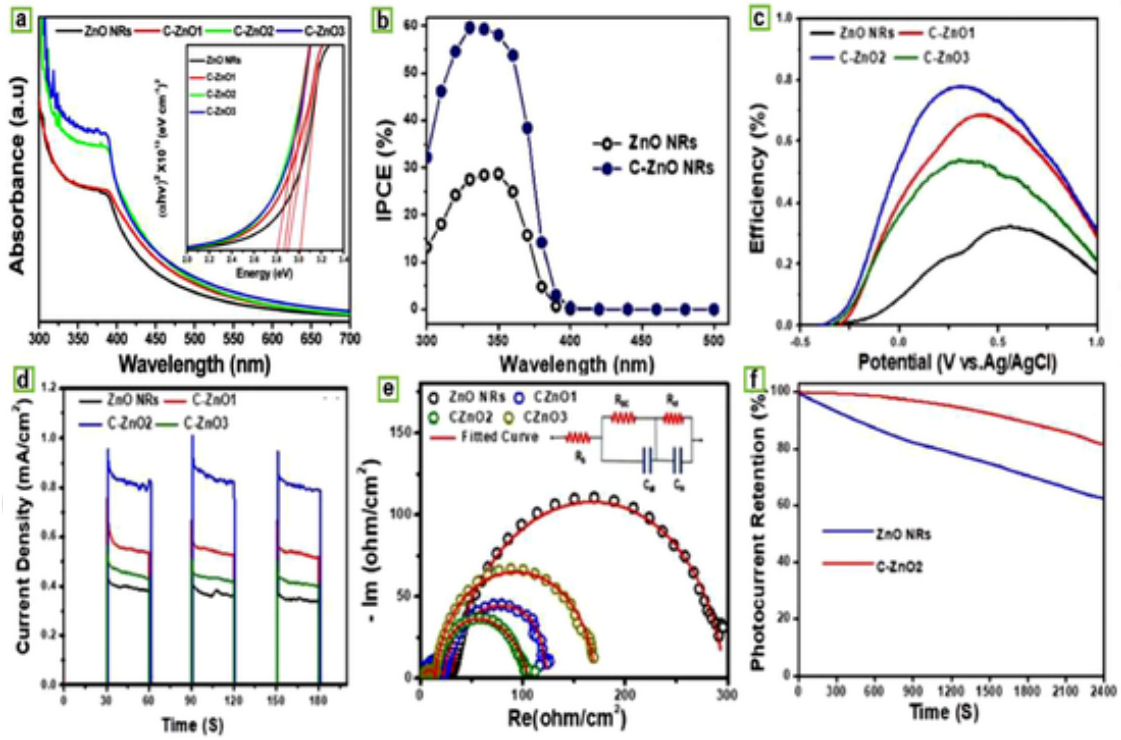

Fig. 20. (a) Spectra of optical absorption of virgin ZnO and C-ZnO nanorods. (b) Curves of IPCE (%) versus wavelength for both ZnO and C-ZnO_2 nanorods. (c) Representation of the photoconversion efficiency according to the applied polarization. (d)Transient photoresponse graphs. (e) Nyquist graphs of the virgin ZnO and C-ZnO nanorods. (f) The photocurrent retention has been evaluated at 0 V compared to Ag/AgCl. Reproduced from [212]. Copyright 2018 ChemistrySelect.

position. The resulting SnS_2/AZO IOS gave a photocurrent density of 1.05 mA/cm², about 19 fold greater than that of bare AZO IOS (0.054 mA/cm²). These findings demonstrate the synergistic action of AZO IOS in combination with narrow bandgap materials like SnS_2 to form a suitable heterojunction. This action leads to the accumulation of the majority of photoelectrons produced in the visible range of the solar spectrum, enhancing their PEC water splitting capability [220].

A number of details relating to the doping of the elements with ZnO are given in Table 2.

To better understand the mechanism of water separation by doping engineering Hoa et al. [221], have proposed a mechanism. As shown in Fig. 21, iron doping leads to impurity band levels and Zn vacancies induce an acceptor level, while oxygen vacancies induce a donor level. As a solar photon is scavenged by a ZnO material, valence band electrons (e^{-1}) are injected into the conduction band. At the same time, the respective holes are created in the valence band (Eq. (1)). The holes and electrons migrate separately on a Fe-doped ZnO under the internal electric field. H_2O is ionized and then O_2 and H_2 are formed by the reaction with electron/hole pairs (Eqs. (6), (7), (8)). In the Fe-doped ZnO, the Fe doping may induce a localization center that is able to inhibit the recombination of the photo-induced e^- and h^+. Thus, H_2 and O_2 may be produced more easily.

Table 2
Synthesis of doped ZnO and their PEC performance.

Photoanode	Synthesis method	Photocurrent density(mA/cm²)	IPCE (%)	Ref
ZnO—N NRs	Ion implantation process	0.160 at 1.1 V vs SCE	17.5	[222]
ZnO—N NWs	Hydrothermal process, with subsequent annealing in ammonia	0.4 at 1.0 V vs Ag/AgCl	14.6	[223]
ZnO—Cu NRs	Electrodeposition	0.083 at 1.0 V vs. SCE	–	[224]
ZnO—Cu	Spray pyrolysis	0.35 at 1.0 V vs. SCE	43	[225]
ZnO—Cu NRs decorated with Au NPs	Hydrothermal with Thermal evaporation	0.0102 at 0.581 V vs. Ag/AgCl	38	[226]
Pb-ZnO thin films	Spray pyrolysis	8 at 1.0 V vs Ag/AgCl)	30	[227]
ZnO-V NRs	Ion implantation	0.0105 at 0.8 V vs. Ag/AgCl	–	[228]
Co—ZnO flake-like	Radio Frequency and Direct current magnetron sputtering	8.7 10^{-4} at 0.4 V vs. Ag/AgCl	–	[229]
Co—ZnO@ Zeolitic imidazolate framework	Spin-coating with Chemical bath deposition	-	75	[230]
Ag/Co –ZnO NWs/ flake-like	Radio Frequency and Direct current magnetron sputtering	0.7 at 0.4 V vs. Ag/AgCl	–	[231]
Ni—ZnO	A high-energy planetary ball mill	4.6 at 1.23 V vs. RHE	–	[232]
Mg—ZnO NRs	Sol–gel and Hydrothermal	0.35 at 1.5 V	–	[233]

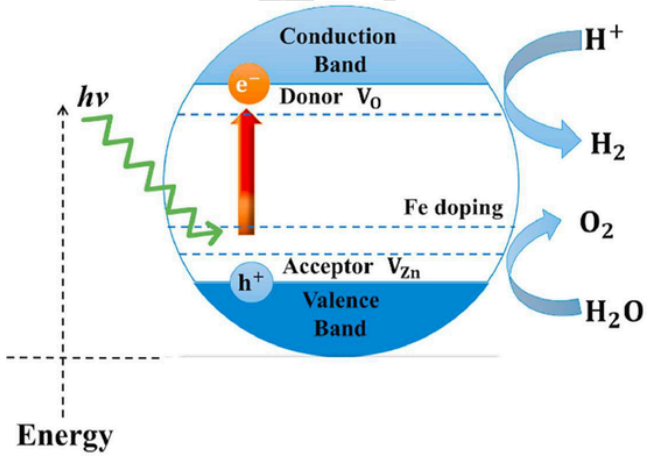

Fig. 21. (a) Mechanism of the water-splitting of Fe-doped ZnO monolayer. Reproduced from [221]. Copyright 2022 Physica E: Low-dimensional Systems and Nanostructures.

$$(Zn, Fe)\,O + h\nu \rightarrow h^+ + e^- \quad (1)$$
$$H_2O \rightarrow H^+ + OH^- \quad (2)$$
$$2e^- + 2H^+ \rightarrow H_2 \quad (3)$$
$$4h^+ + 2OH^- \rightarrow 2H^+ + O_2 \quad (4)$$

3. Challenges and opportunities

Photoelectrochemical water splitting technology opens up a wide range of opportunities in the field of sustainable energy. As hydrogen is recognized as a clean energy source, PEC represents a way to produce hydrogen free from fossil fuels, helping to create a more environmentally sustainable energy landscape. In contrast to steam methane reforming, a popular process for hydrogen generation, PEC does not generate carbon dioxide as a by-product, leading to a reduced carbon footprint and less greenhouse gas emissions. In addition to its contribution to decentralized hydrogen generation, PEC has the capacity to revolutionize energy storage, offering a carbon-neutral solution which is complementary to existing infrastructure. Hydrogen produced by PEC may be utilized in fuel cells for electricity generation, as a clean fuel source for industrial processes or transportation, providing a diverse approach that is fully compatible with current energy systems. As the field progresses, the incorporation of advanced materials and catalysts holds the promise of improved efficiency and profitability. To conclude, we reviewed the latest progress on a variety of metal oxide-based photoanodes and photocathodes (Fe_2O_3, ZnO, CuO, Co_3O_4) for PEC water splitting. The structure, operating principle and their pertinent performance computations of a PEC cell were briefly presented. Nanostructured materials based on metal oxides (Fe_2O_3, ZnO, CuO, Co_3O_4) are frequently employed as efficient photoelectrodes for water splitting and decomposition of organic pollutants. Nevertheless, their instability, resulting from photocorrosion, and their rapid recombination rates of charge carriers as well as their insufficient absorption capability of visible light limit considerably their use in photoconversion processes and their photoelectrocatalytic efficiency. For this reason, several strategies including morphological treatment and design of heterostructured hybrids using appropriate material compositions and doping or amending with inorganic metal elements, or heteroatoms are employed for the fabrication of different photoelectrodes with improved efficiency for water splitting. In this respect, the band positions of the semiconductors concerned should be appropriately placed and the photoelectrocatalytic responses provided by the various materials should be compatible, showing a synergistic effect. Despite the fact that doping with impurities or self-defects was developed to alter the optical/electronic characteristics of wide bandgap metal oxides, the total visible light photoactivity is always very low. Theoretical calculations predicted that co-doping with cations and anions is an appropriate way to adjust the metal oxide electronic band structures for PEC water oxidation, but experimental findings are not yet satisfactory. We are convinced that the challenge consists in improving the efficiency of doping and getting good control over the dopant content and the spatial arrangement of the dopants. Ion Implantation is a method that can selectively implant any element of choice in a SC electrode under depth conditions and controlled dose. Yet, the full benefits of ion implantation in addressing some of the biggest issues in PEC water splitting are not fully exploited. On the other hand, the writing of this review has allowed us to extract

the two main issues that can restrict the performance of a photoelectrode. Firstly, there is the question of charge transport between the particles and the back contact. The recombination loss and the interfacial resistance may be an important constraint on their PEC activity. Secondly, there is the question of the electrical conductivity of oxides since most of them cannot conduct very well, to solve this problem defect engineering and post growth chemical processing might also be necessary to boost the electrical conductivity. In addition, the challenge of providing low-cost surface coatings to protect photoelectrodes from photocorrosion remains challenging. Up to now atomic layer deposition remains the predominantly effective way to reach the protection goal, owing to its high coating value with no pinholes and manageable layer thickness. However, the high cost of this method should push the scientific community to develop low-cost chemical protection approaches. In addition to investigating photoelectrode materials, another formidable challenge will be to develop novel in situ spectroscopy/microscopy tools to better characterise the basic mechanism of PEC water splitting. Such techniques need high temporal resolution in order to examine reaction intermediates and charge dynamics onto the surface of photoelectrodes in working conditions. Recently, in situ transient absorption spectroscopy was used to examine the carrier dynamics in PEC water splitting giving insight into the yields of photoinduced charge and lifetime of these operations [234]. Moreover, in situ infrared spectroscopy was applied to explore the intermediates of water oxidation occurring on the photo-anode surface via exploring the photosensitive absorption behaviour of the photo-electrodes [235]. We strongly recommend that in-situ comprehensive investigations of MO for PECWS are crucial for a better understanding of the reaction mechanism and hold the key to improving and maximising the PEC efficiency of metal oxides photoelectrodes. Finally, the development of potential metal oxides based photoelectrodes for H_2 generation for commercial purposes still remained a major challenge, hence it is essential to use them in large-scale systems for the generation of hydrogen and to avoid the use of carbon-based energy sources. Therefore, collaboration between academia and industry plays a key role in fostering innovation, addressing challenges and unlocking the full potential of PEC water splitting as a major contributor to the shift towards a greener future.

CRediT authorship contribution statement

M. El ouardi: Writing – original draft, Formal analysis, Data curation. **A.El Idrissi:** Writing – original draft, Formal analysis. **H.Ait Ahsaine:** Writing – original draft, Validation, Supervision, Project administration. **A. BaQais:** Writing – original draft, Formal analysis. **M. Saadi:** Validation, Supervision, Project administration. **M. Arab:** Writing – original draft, Validation, Supervision, Project administration.

Declaration of competing interest

The authors declare that they have no known competing financial interests or personal relationships that could have appeared to influence the work reported in this paper.

Data availability

Data will be made available on request.

Acknowledgments

This work was supported by the faculty of sciences and the Mohammed V university in Rabat and Toulon University in France.

References

[1] M. El Ouardi, A. El aouni, H.A. Ahsaine, M. Zbair, A. BaQais, M. Saadi, ZIF-8 metal organic framework composites as hydrogen evolution reaction photocatalyst: a review of the current state, Chemosphere 308 (2022) 136483, https://doi.org/10.1016/j.chemosphere.2022.136483.

[2] M. El ouardi, A. El Idrissi, M. Arab, M. Zbair, H. Haspel, M. Saadi, H. Ait Ahsaine, Review of photoelectrochemical water splitting: from quantitative approaches to effect of sacrificial agents, oxygen vacancies, thermal and magnetic field on (photo)electrolysis, Int. J. Hydrogen Energy (2023), https://doi.org/10.1016/j.ijhydene.2023.09.111.

[3] Y. Li, Z. Liu, Z. Guo, M. Ruan, X. Li, Y. Liu, Efficient WO3 photoanode modified by Pt layer and plasmonic Ag for enhanced charge separation and transfer to promote photoelectrochemical performances, ACS Sustain. Chem. Eng. 7 (2019) 12582–12590, https://doi.org/10.1021/acssuschemeng.9b02450.

[4] G. Fang, Z. Liu, C. Han, Enhancing the PEC water splitting performance of BiVO4 co-modifying with NiFeOOH and Co-Pi double layer cocatalysts, Appl. Surf. Sci. 515 (2020) 146095, https://doi.org/10.1016/j.apsusc.2020.146095.

[5] B.-E. Channab, M.E. Ouardi, O.A. Layachi, S.E. Marrane, A.E. Idrissi, A.A. BaQais, H.A. Ahsaine, Recent trends on MIL-Fe Metal-Organic Frameworks: synthesis approaches, structural insights, and applications in organic pollutant adsorption and photocatalytic degradation: a review, Environ. Sci. Nano. (2023), https://doi.org/10.1039/D3EN00332A.

[6] Y. Chen, X. Feng, M. Liu, J. Su, S. Shen, Towards efficient solar-to-hydrogen conversion: fundamentals and recent progress in copper-based chalcogenide photocathodes, Nanophotonics 5 (2016) 524–547, https://doi.org/10.1515/nanoph-2016-0027.

[7] C.-H. Liao, C.-W. Huang, J.C.S. Wu, Hydrogen production from semiconductor-based photocatalysis via water splitting, Catalysts 2 (2012) 490–516, https://doi.org/10.3390/catal2040490.

[8] B. El Allaoui, H. Chakhtouna, N. Zari, H. Benzeid, A. el kacem Qaiss, R. Bouhfid, Superhydrophobic alkylsilane functionalized cellulose beads for efficient oil/water separation, J. Water Process Eng. 54 (2023) 04015, https://doi.org/10.1016/j.jwpe.2023.104015.

[9] P. Subramanyam, B. Meena, V. Biju, H. Misawa, S. Challapalli, Emerging materials for plasmon-assisted photoelectrochemical water splitting, J. Photochem. Photobiol. C Photochem. Rev. (2021) 100472, https://doi.org/10.1016/j.jphotochemrev.2021.100472.

[10] G. Wang, Y. Ling, H. Wang, L. Xihong, Y. Li, Chemically modified nanostructures for photoelectrochemical water splitting, J. Photochem. Photobiol. C Photochem. Rev. 19 (2014) 35–51, https://doi.org/10.1016/j.jphotochemrev.2013.10.006.

[11] X. Liu, H. Zheng, Z. Sun, A. Han, P. Du, Earth-abundant copper-based bifunctional electrocatalyst for both catalytic hydrogen production and water oxidation, ACS Catal 5 (2015) 1530–1538, https://doi.org/10.1021/cs501480s.

[12] N.S. Lewis, D.G. Nocera, Powering the planet: chemical challenges in solar energy utilization, Proc. Natl. Acad. Sci. 103 (2006) 15729–15735, https://doi.org/10.1073/pnas.0603395103.

[13] X. Gao, J. Wang, Q. Xue, Y.-Y. Ma, Y. Gao, AgBr/polyoxometalate/graphene oxide ternary composites for visible light-driven photocatalytic hydrogen production, ACS Appl. Nano Mater. 4 (2021) 2126–2135, https://doi.org/10.1021/acsanm.0c03406.

[14] L. Xiao, S.-Y. Wu, Y.-R. Li, Advances in solar hydrogen production via two-step water-splitting thermochemical cycles based on metal redox reactions, Renew. Energy 41 (2012) 1–12, https://doi.org/10.1016/j.renene.2011.11.023.

[15] X. Shi, Y. Qian, S. Yang, Fluctuation analysis of a complementary wind–solar energy system and integration for large scale hydrogen production, ACS Sustain. Chem. Eng. 8 (2020) 7097–7110, https://doi.org/10.1021/acssuschemeng.0c01054.

[16] S. Lotfi, M. El Ouardi, H. Ait Ahsaine, V. Madigou, A. BaQais, A. Assani, M. Saadi, M. Arab, Low-temperature synthesis, characterization and photocatalytic properties of lanthanum vanadate $LaVO_4$, Heliyon 9 (2023) e17255, https://doi.org/10.1016/j.heliyon.2023.e17255.

[17] S. Azmi, O.A. Layachi, M.E. Ouardi, E.M. Khoumri, A. Moujib, A.E. Brouzi, M. Nohair, L. Pezzato, M. Dabala, Growth of Cu_2ZnSnS_4 thin film absorber layer on transparent conductive oxides and molybdenum substrates by electrodeposition for photovoltaic application, Optik (Stuttg) 250 (2022) 168320, https://doi.org/10.1016/j.ijleo.2021.168320.

[18] Y. Bu, J.-P. Ao, A review on photoelectrochemical cathodic protection semiconductor thin films for metals, Green Energy Environ 2 (2017) 331–362, https://doi.org/10.1016/j.gee.2017.02.003.

[19] S. Bai, X. Yang, C. Liu, X. Xiang, R. Luo, J. He, A. Chen, An integrating photoanode of WO3/Fe_2O_3 heterojunction decorated with NiFe-LDH to improve PEC water splitting efficiency, ACS Sustain. Chem. Eng. 6 (2018) 12906–12913, https://doi.org/10.1021/acssuschemeng.8b02267.

[20] M.A. Marwat, M. Humayun, M.W. Afridi, H. Zhang, M.R. Abdul Karim, M. Ashtar, M. Usman, S. Waqar, H. Ullah, C. Wang, W. Luo, Advanced catalysts for photoelectrochemical water splitting, ACS Appl. Energy Mater. 4 (2021) 12007–12031, https://doi.org/10.1021/acsaem.1c02548.

[21] A. Wei, X. Xie, Z. Wen, H. Zheng, H. Lan, H. Shao, X. Sun, J. Zhong, S.-T. Lee, Triboelectric nanogenerator driven self-powered photoelectrochemical water splitting based on hematite photoanodes, ACS Nano 12 (2018) 8625–8632, https://doi.org/10.1021/acsnano.8b04363.

[22] K. Maeda, K. Domen, Photocatalytic water splitting: recent progress and future challenges, J. Phys. Chem. Lett. 1 (2010) 2655–2661, https://doi.org/10.1021/

jz1007966.
[23] K. Maeda, Photocatalytic water splitting using semiconductor particles: history and recent developments, J. Photochem. Photobiol. C Photochem. Rev. 12 (2011) 237–268, https://doi.org/10.1016/j.jphotochemrev.2011.07.001.
[24] R. Abe, Recent progress on photocatalytic and photoelectrochemical water splitting under visible light irradiation, J. Photochem. Photobiol. C Photochem. Rev. 11 (2010) 179–209, https://doi.org/10.1016/j.jphotochemrev.2011.02.003.
[25] J. Wu, Y. Zhang, J. Zhou, K. Wang, Y.-Z. Zheng, X. Tao, Uniformly assembling n-type metal oxide nanostructures (TiO_2 nanoparticles and SnO_2 nanowires) onto P doped g-C3N4 nanosheets for efficient photocatalytic water splitting, Appl. Catal. B Environ. 278 (2020) 119301, https://doi.org/10.1016/j.apcatb.2020.119301.
[26] I. Akkerman, M. Janssen, J. Rocha, R.H. Wijffels, Photobiological hydrogen production: photochemical efficiency and bioreactor design, Int. J. Hydrogen Energy 27 (2002) 1195–1208, https://doi.org/10.1016/S0360-3199(02)00071-X.
[27] S.I. Allakhverdiev, V. Thavasi, V.D. Kreslavski, S.K. Zharmukhamedov, V.V. Klimov, S. Ramakrishna, D.A. Los, M. Mimuro, H. Nishihara, R. Carpentier, Photosynthetic hydrogen production, J. Photochem. Photobiol. C Photochem. Rev. 11 (2010) 101–113, https://doi.org/10.1016/j.jphotochemrev.2010.07.002.
[28] J. Lédé, F. Lapicque, J. Villermaux, Production of hydrogen by direct thermal decomposition of water, Int. J. Hydrogen Energy 8 (1983) 675–679, https://doi.org/10.1016/0360-3199(83)90175-1.
[29] S.Z. Baykara, Hydrogen production by direct solar thermal decomposition of water, possibilities for improvement of process efficiency, Int. J. Hydrogen Energy 29 (2004) 1451–1458, https://doi.org/10.1016/j.ijhydene.2004.02.014.
[30] C.V. Reddy, K.R. Reddy, N.P. Shetti, J. Shim, T.M. Aminabhavi, D.D. Dionysiou, Hetero-nanostructured metal oxide-based hybrid photocatalysts for enhanced photoelectrochemical water splitting – a review, Int. J. Hydrogen Energy 45 (2020) 18331–18347, https://doi.org/10.1016/j.ijhydene.2019.02.109.
[31] Y.W. Phuan, W.-J. Ong, M.N. Chong, J.D. Ocon, Prospects of electrochemically synthesized hematite photoanodes for photoelectrochemical water splitting: a review, J. Photochem. Photobiol. C Photochem. Rev. 33 (2017) 54–82, https://doi.org/10.1016/j.jphotochemrev.2017.10.001.
[32] S. Chen, D. Huang, P. Xu, W. Xue, L. Lei, M. Cheng, R. Wang, X. Liu, R. Deng, Semiconductor-based photocatalysts for photocatalytic and photoelectrochemical water splitting: will we stop with photocorrosion? J. Mater. Chem. A 8 (2020) 2286–2322, https://doi.org/10.1039/C9TA12799B.
[33] A. Elaouni, M.E. Ouardi, A. BaQais, M. Arab, M. Saadi, H.A. Ahsaine, Bismuth tungstate Bi_2WO_6: a review on structural, photophysical and photocatalytic properties, RSC Adv. 13 (2023) 17476–17494, https://doi.org/10.1039/D3RA01987J.
[34] K. Maeda, K. Domen, Solid solution of GaN and ZnO as a stable photocatalyst for overall water splitting under visible light, Chem. Mater. 22 (2010) 612–623, https://doi.org/10.1021/cm901917a.
[35] C. Acar, I. Dincer, G.F. Naterer, Review of photocatalytic water-splitting methods for sustainable hydrogen production, Int. J. Energy Res. 40 (2016) 1449–1473, https://doi.org/10.1002/er.3549.
[36] P.-Y. Hsieh, J.-Y. Wu, T.-F.M. Chang, C.-Y. Chen, M. Sone, Y.-J. Hsu, Near infrared-driven photoelectrochemical water splitting: review and future prospects, Arab. J. Chem. 13 (2020) 8372–8387, https://doi.org/10.1016/j.arabjc.2020.05.025.
[37] A.S. Joshi, I. Dincer, B.V. Reddy, Exergetic assessment of solar hydrogen production methods, Int. J. Hydrogen Energy 35 (2010) 4901–4908, https://doi.org/10.1016/j.ijhydene.2009.09.067.
[38] G. Liu, Y. Sheng, J.W. Ager, M. Kraft, R. Xu, Research advances towards large-scale solar hydrogen production from water, EnergyChem. 1 (2019) 100014, https://doi.org/10.1016/j.enchem.2019.100014.
[39] J. Jia, L.C. Seitz, J.D. Benck, Y. Huo, Y. Chen, J.W.D. Ng, T. Bilir, J.S. Harris, T.F. Jaramillo, Solar water splitting by photovoltaic-electrolysis with a solar-to-hydrogen efficiency over 30%, Nat. Commun. 7 (2016) 13237, https://doi.org/10.1038/ncomms13237.
[40] J.H. Kim, D. Hansora, P. Sharma, J.-W. Jang, J.S. Lee, Toward practical solar hydrogen production – an artificial photosynthetic leaf-to-farm challenge, Chem. Soc. Rev. 48 (2019) 1908–1971, https://doi.org/10.1039/C8CS00699G.
[41] M. Grätzel, Photoelectrochemical cells, Nature 414 (2001) 338–344, https://doi.org/10.1038/35104607.
[42] K. Sivula, R. van de Krol, Semiconducting materials for photoelectrochemical energy conversion, Nat. Rev. Mater. 1 (2016) 1–16, https://doi.org/10.1038/natrevmats.2015.10.
[43] E. Amaterz, A. Tara, A. Bouddouch, A. Taoufyq, B. Bakiz, A. Benlhachemi, O. Jbara, Photo-electrochemical degradation of wastewaters containing organics catalysed by phosphate-based materials: a review, Rev. Environ. Sci. Biotechnol. 19 (2020) 843–872, https://doi.org/10.1007/s11157-020-09547-9.
[44] A. Hasani, M. Tekalgne, Q.V. Le, H.W. Jang, S.Y. Kim, Two-dimensional materials as catalysts for solar fuels: hydrogen evolution reaction and CO_2 reduction, J. Mater. Chem. A. 7 (2019) 430–454, https://doi.org/10.1039/C8TA09496A.
[45] S. Lotfi, M.E. Ouardi, H.A. Ahsaine, A. Assani, Recent progress on the synthesis, morphology and photocatalytic dye degradation of BiVO4 photocatalysts: a review, Catal. Rev. 0 (2022) 1–45, https://doi.org/10.1080/01614940.2022.2057044.
[46] A. Fujishima, X. Zhang, D.A. Tryk, TiO_2 photocatalysis and related surface phenomena, Surf. Sci. Rep. 63 (2008) 515–582, https://doi.org/10.1016/j.surfrep.2008.10.001.
[47] K.R. Reddy, M. Hassan, V.G. Gomes, Hybrid nanostructures based on titanium dioxide for enhanced photocatalysis, Appl. Catal. Gen. C (2015) 1–16, https://doi.org/10.1016/j.apcata.2014.10.001.
[48] B.-E. Channab, M.E. Ouardi, S.E. Marrane, O.A. Layachi, A.E. Idrissi, S. Farsad, D. Mazkad, A. BaQais, M. Lasri, H.A. Ahsaine, Alginate@$ZnCO_2O_4$ for efficient peroxymonosulfate activation towards effective rhodamine B degradation: optimization using response surface methodology, RSC Adv. 13 (2023) 20150–20163, https://doi.org/10.1039/D3RA02865H.
[49] Y. Yang, S. Niu, D. Han, T. Liu, G. Wang, Y. Li, Progress in developing metal oxide nanomaterials for photoelectrochemical water splitting, Adv. Energy Mater. 7 (2017) 1700555, https://doi.org/10.1002/aenm.201700555.
[50] G. Wang, Y. Yang, Y. Ling, H. Wang, X. Lu, Y.-C. Pu, J.Z. Zhang, Y. Tong, Y. Li, An electrochemical method to enhance the performance of metal oxides for photoelectrochemical water oxidation, J. Mater. Chem. A 4 (2016) 2849–2855, https://doi.org/10.1039/C5TA10477G.
[51] M. Xu, P. Da, H. Wu, D. Zhao, G. Zheng, Controlled Sn-doping in TiO_2 nanowire photoanodes with enhanced photoelectrochemical conversion, Nano Lett. 12 (2012) 1503–1508, https://doi.org/10.1021/nl2042968.
[52] T.K. Sung, J.H. Kang, D.M. Jang, Y. Myung, G.B. Jung, H.S. Kim, C.S. Jung, Y.J. Cho, J. Park, C.-L. Lee, CdSSe layer-sensitized TiO_2 nanowire arrays as efficient photoelectrodes, J. Mater. Chem. 21 (2011) 4553–4561, https://doi.org/10.1039/C0JM03818K.
[53] A. Walsh, Y. Yan, M.N. Huda, M.M. Al-Jassim, S.-H. Wei, Band edge electronic structure of $BiVO_4$: elucidating the role of the Bi s and V d orbitals, Chem. Mater. 21 (2009) 547–551, https://doi.org/10.1021/cm802894z.
[54] M. Desseigne, V. Chevallier, V. Madigou, M.-V. Coulet, O. Heintz, H. Ait Ahsaine, M. Arab, Plasmonic photocatalysts based on Au nanoparticles and WO_3 for visible light-induced photocatalytic activity, Catalysts 13 (2023) 1333, https://doi.org/10.3390/catal13101333.
[55] A. Kudo, Y. Miseki, Heterogeneous photocatalyst materials for water splitting, Chem. Soc. Rev. 38 (2009) 253–278, https://doi.org/10.1039/B800489G.
[56] S.C. Suman, A. Kumar, P. Kumar, Zn doped α-Fe_2O_3: an efficient material for UV driven photocatalysis and electrical conductivity, Crystals 10 (2020) 273, https://doi.org/10.3390/cryst10040273.
[57] L. Liao, Q. Zhang, Z. Su, Z. Zhao, Y. Wang, Y. Li, X. Lu, D. Wei, G. Feng, Q. Yu, X. Cai, J. Zhao, Z. Ren, H. Fang, F. Robles-Hernandez, S. Baldelli, J. Bao, Efficient solar water-splitting using a nanocrystalline CoO photocatalyst, Nat. Nanotechnol. 9 (2014) 69–73, https://doi.org/10.1038/nnano.2013.272.
[58] S.N.F. Moridon, M.N.I. Salehmin, K. Arifin, L.J. Minggu, M.B. Kassim, Synthesis of cobalt oxide on FTO by hydrothermal method for photoelectrochemical water splitting application, Appl. Sci. 11 (2021) 3031, https://doi.org/10.3390/app11073031.
[59] M. El Hanafi, A. BaQais, M. Saadi, H. Ait Ahsaine, Advances and outlook of metal–organic frameworks as high-performance electrocatalysts for hydrogen evolution reaction: a minireview, Energy Fuels 37 (2023) 10869–10885, https://doi.org/10.1021/acs.energyfuels.3c01533.
[60] M. El Ouardi, O. Ait Layachi, E. Amaterz, A. El Idrissi, A. Taoufyq, B. Bakiz, A. Benlhachemi, M. Arab, A. BaQais, H. Ait Ahsaine, Photo-electrochemical degradation of rhodamine B using electrodeposited $Mn_3(PO_4)_{2.3}H_2O$ thin films, J. Photochem. Photobiol. Chem. 444 (2023) 115011, https://doi.org/10.1016/j.jphotochem.2023.115011.
[61] M. Ahmed, I. Dincer, A review on photoelectrochemical hydrogen production systems: challenges and future directions, Int. J. Hydrogen Energy 44 (2019) 2474–2507, https://doi.org/10.1016/j.ijhydene.2018.12.037.
[62] D. Kang, J.L. Young, H. Lim, W.E. Klein, H. Chen, Y. Xi, B. Gai, T.G. Deutsch, J. Yoon, Printed assemblies of GaAs photoelectrodes with decoupled optical and reactive interfaces for unassisted solar water splitting, Nat. Energy 2 (2017) 1–5, https://doi.org/10.1038/nenergy.2017.43.
[63] W.-H. Cheng, M.H. Richter, M.M. May, J. Ohlmann, D. Lackner, F. Dimroth, T. Hannappel, H.A. Atwater, H.-J. Lewerenz, Monolithic photoelectrochemical device for direct water splitting with 19% efficiency, ACS Energy Lett. 3 (2018) 1795–1800, https://doi.org/10.1021/acsenergylett.8b00920.
[64] J.L. Young, M.A. Steiner, H. Döscher, R.M. France, J.A. Turner, T.G. Deutsch, Direct solar-to-hydrogen conversion via inverted metamorphic multi-junction semiconductor architectures, Nat. Energy 2 (2017) 1–8, https://doi.org/10.1038/nenergy.2017.28.
[65] D. Hong, G. Cao, X. Zhang, J. Qu, Y. Deng, H. Liang, J. Tang, Construction of a Pt-modified chestnut-shell-like ZnO photocatalyst for high-efficiency photochemical water splitting, Electrochim. Acta 283 (2018) 959–969, https://doi.org/10.1016/j.electacta.2018.05.051.
[66] S. Cao, Y. Li, B. Zhu, M. Jaroniec, J. Yu, Facet effect of Pd cocatalyst on photocatalytic CO_2 reduction over g-C3N4, J. Catal. 349 (2017) 208–217, https://doi.org/10.1016/j.jcat.2017.02.005.
[67] N.L. Reddy, S. Kumar, V. Krishnan, M. Sathish, M.V. Shankar, Multifunctional Cu/Ag quantum dots on TiO_2 nanotubes as highly efficient photocatalysts for enhanced solar hydrogen evolution, J. Catal. 350 (2017) 226–239, https://doi.org/10.1016/j.jcat.2017.02.032.
[68] J. Chen, J. Zhang, M. Ye, Z. Rao, T. Tian, L. Shu, P. Lin, X. Zeng, S. Ke, Flexible TiO_2/Au thin films with greatly enhanced photocurrents for photoelectrochemical water splitting, J. Alloys Compd. 815 (2020) 152471, https://doi.org/10.1016/j.jallcom.2019.152471.
[69] A. Meng, L. Zhang, B. Cheng, J. Yu, Dual cocatalysts in TiO_2 Photocatalysis, Adv. Mater. 31 (2019) 1807660, https://doi.org/10.1002/adma.201807660.
[70] N.N. Rosman, R.M. Yunus, L.J. Minggu, K. Arifin, M.N.I. Salehmin, M.A. Mohamed, M.B. Kassim, Photocatalytic properties of two-dimensional graphene and layered transition-metal dichalcogenides based photocatalyst for photoelectrochemical hydrogen generation: an overview, Int. J. Hydrogen Energy 43 (2018) 18925–18945, https://doi.org/10.1016/j.ijhydene.2018.08.126.

[71] S.S. Patil, M.A. Johar, M.A. Hassan, A. Waseem, I.V. Bagal, D.E. Shinde, S.-W. Ryu, Synergic effect of ZnO nanostructures and cobalt phosphate co-catalyst on photoelectrochemical properties of GaN, Mater. Chem. Phys. 260 (2021) 124141, https://doi.org/10.1016/j.matchemphys.2020.124141.

[72] C. Lo Vecchio, S. Trocino, S. Campagna Zignani, V. Baglio, A. Carbone, M.I. Díez García, M. Contreras, R. Gómez, A.S. Aricò, Enhanced photoelectrochemical water splitting at hematite photoanodes by effect of a NiFe-oxide co-catalyst, Catalysts 10 (2020) 525, https://doi.org/10.3390/catal10050525.

[73] A. Singh, R. Tejasvi, S. Karmakar, S. Basu, α-Fe_2O_3 nanorods decorated with $NiMnO_3$ co-catalyst as photoanode for enhanced oxygen evolution reaction in photoelectrochemical water splitting, Mater. Today Commun. 27 (2021) 102231, https://doi.org/10.1016/j.mtcomm.2021.102231.

[74] P. Zhang, T. Wang, X. Chang, L. Zhang, J. Gong, Synergistic cocatalytic effect of carbon nanodots and Co_3O_4 nanoclusters for the photoelectrochemical water oxidation on hematite, Angew. Chem. 128 (2016) 5945–5949, https://doi.org/10.1002/ange.201600918.

[75] P. Wang, Z. Liu, C. Han, X. Ma, Z. Tong, B. Tan, Cu_2O/CuO heterojunction formed by thermal oxidation and decorated with Pt co-catalyst as an efficient photocathode for photoelectrochemical water splitting, J. Nanopart. Res. 23 (2021) 268, https://doi.org/10.1007/s11051-021-05383-2.

[76] H.L.S. Santos, P.G. Corradini, M.A.S. Andrade, L.H. Mascaro, CuO/NiOx thin film–based photocathodes for photoelectrochemical water splitting, J. Solid State Electrochem. 24 (2020) 1899–1908, https://doi.org/10.1007/s10008-020-04513-5.

[77] Z. Liu, Q. Song, M. Zhou, Z. Guo, J. Kang, H. Yan, Synergistic enhancement of charge management and surface reaction kinetics by spatially separated cocatalysts and p-n heterojunctions in Pt/$CuWO_4$/Co_3O_4 photoanode, Chem. Eng. J. 374 (2019) 554–563, https://doi.org/10.1016/j.cej.2019.05.191.

[78] Z. Yu, Y. Li, J. Qu, R. Zheng, J.M. Cairney, J. Zhang, M. Zhu, A. Khan, W. Li, Enhanced photoelectrochemical water-splitting performance with a hierarchical heterostructure: Co_3O_4 nanodots anchored TiO_2@P-C3N4 core-shell nanorod arrays, Chem. Eng. J. 404 (2021) 126458, https://doi.org/10.1016/j.cej.2020.126458.

[79] C. Zhong, Z. Shang, C. Zhao, H. Luo, Y. Cao, D. Yan, K. You, Co-catalyst Ti3C2TX MXene-modified ZnO nanorods photoanode for enhanced photoelectrochemical water splitting, Top. Catal. 66 (2023) 12–21, https://doi.org/10.1007/s11244-022-01619-0.

[80] S.J.A. Moniz, S.A. Shevlin, D.J. Martin, Z.-X. Guo, J. Tang, Visible-light driven heterojunction photocatalysts for water splitting – a critical review, Energy Environ. Sci. 8 (2015) 731–759, https://doi.org/10.1039/C4EE03271C.

[81] J. Rohilla, P.P. Ingole, Optimizing hematite nanostructures for electrochemical and photoelectrochemical water splitting applications, Curr. Opin. Green Sustain. Chem. 29 (2021) 100455, https://doi.org/10.1016/j.cogsc.2021.100455.

[82] D. Zhou, K. Fan, Recent strategies to enhance the efficiency of hematite photoanodes in photoelectrochemical water splitting, Chin. J. Catal. 42 (2021) 904–919, https://doi.org/10.1016/S1872-2067(20)63712-3.

[83] K. Sivula, F.Le Formal, M. Grätzel, Solar water splitting: progress using hematite (α-Fe_2O_3) photoelectrodes, ChemSusChem 4 (2011) 432–449, https://doi.org/10.1002/cssc.201000416.

[84] S.D. Tilley, M. Cornuz, K. Sivula, M. Grätzel, Light-Induced water splitting with hematite: improved nanostructure and iridium oxide catalysis, Angew. Chem. Int. Ed. 49 (2010) 6405–6408, https://doi.org/10.1002/anie.201003110.

[85] A. Pu, J. Deng, M. Li, J. Gao, H. Zhang, Y. Hao, J. Zhong, X. Sun, Coupling Ti-doping and oxygen vacancies in hematite nanostructures for solar water oxidation with high efficiency, J. Mater. Chem. A 2 (2014) 2491–2497, https://doi.org/10.1039/C3TA14575A.

[86] M. Li, Z. Zhang, F. Lyu, X. He, Z. Liang, M.-S. Balogun, X. Lu, P.-P. Fang, Y. Tong, Facile hydrothermal synthesis of three dimensional hematite nanostructures with enhanced water splitting performance, Electrochim. Acta 186 (2015) 95–100, https://doi.org/10.1016/j.electacta.2015.10.048.

[87] A. Tofanello, S. Shen, F.L. de Souza, L. Vayssieres, Strategies to improve the photoelectrochemical performance of hematite nanorod-based photoanodes, APL Mater. 8 (2020) 040905, https://doi.org/10.1063/5.0003146.

[88] J. Wang, M. Wang, T. Zhang, Z. Wang, P. Guo, J. Su, L. Guo, Facile synthesis of ultrafine hematite nanowire arrays in mixed water–ethanol–acetic acid solution for enhanced charge transport and separation, ACS Appl. Mater. Interfaces 10 (2018) 12594–12602, https://doi.org/10.1021/acsami.7b18534.

[89] N.A. Arzaee, M.F. Mohamad Noh, A. Ab Halim, M.A.F. Abdul Rahim, N.A. Mohamed, J. Safaei, A. Aadenan, S.N. Syed Nasir, A.F. Ismail, M.A. Mat Teridi, Aerosol-assisted chemical vapour deposition of α-Fe_2O_3 nanoflowers for photoelectrochemical water splitting, Ceram. Int. 45 (2019) 16797–16802, https://doi.org/10.1016/j.ceramint.2019.05.219.

[90] L. Wang, H. Hu, N.T. Nguyen, Y. Zhang, P. Schmuki, Y. Bi, Plasmon-induced hole-depletion layer on hematite nanoflake photoanodes for highly efficient solar water splitting, Nano Energy 35 (2017) 171–178, https://doi.org/10.1016/j.nanoen.2017.03.035.

[91] A. Mao, K. Shin, J.K. Kim, D.H. Wang, G.Y. Han, J.H. Park, Controlled synthesis of vertically aligned hematite on conducting substrate for photoelectrochemical cells: nanorods versus nanotubes, ACS Appl. Mater. Interfaces 3 (2011) 1852–1858, https://doi.org/10.1021/am200407t.

[92] G. Rahman, Z. Najaf, A. ul H.A. Shah, S.A. Mian, Investigation of the structural, optical, and photoelectrochemical properties of α-Fe_2O_3 nanorods synthesized via a facile chemical bath deposition, Optik (Stuttg) 200 (2020) 163454, https://doi.org/10.1016/j.ijleo.2019.163454.

[93] H. Bazrafshan, Z. Alipour Tesieh, S. Dabirnia, R. Shajareh Touba, H. Manghabati, B. Nasernejad, Synthesis of novel α-Fe_2O_3 nanorods without surfactant and its electrochemical performance, Powder Technol. 308 (2017) 266–272, https://doi.org/10.1016/j.powtec.2016.12.015.

[94] C. Feng, S. Fu, W. Wang, Y. Zhang, Y. Bi, High-crystalline and high-aspect-ratio hematite nanotube photoanode for efficient solar water splitting, Appl. Catal. B Environ. 257 (2019) 117900, https://doi.org/10.1016/j.apcatb.2019.117900.

[95] N. Mouchani, A.H. Farahmand-Dashtarjandi, A. Yourdkhani, R. Poursalehi, N.B. Simhachalam, Oxygen vacancy modulation of hematite thin films using annealing in graphite bed for photoelectrochemical applications, Surf. Interfaces 42 (2023) 103456, https://doi.org/10.1016/j.surfin.2023.103456.

[96] Y. Qiu, S.-F. Leung, Q. Zhang, B. Hua, Q. Lin, Z. Wei, K.-H. Tsui, Y. Zhang, S. Yang, Z. Fan, Efficient photoelectrochemical water splitting with ultrathin films of hematite on three-dimensional nanophotonic structures, Nano Lett. 14 (2014) 2123–2129, https://doi.org/10.1021/nl500359e.

[97] M. Matsuhisa, S. Tsubaki, F. Kishimoto, S. Fujii, I. Hirano, M. Horibe, E. Suzuki, R. Shimizu, T. Hitosugi, Y. Wada, Hole accumulation at the grain boundary enhances water oxidation at α-Fe_2O_3 electrodes under a microwave electric field, J. Phys. Chem. C 124 (2020) 7749–7759, https://doi.org/10.1021/acs.jpcc.9b11179.

[98] F. Leandro Souza, K. Pimenta Lopes, E. Longo, E. Roberto Leite, The influence of the film thickness of nanostructured α-Fe_2O_3 on water photooxidation, Phys. Chem. Chem. Phys. 11 (2009) 1215–1219, https://doi.org/10.1039/B811946E.

[99] Y. Ling, G. Wang, D.A. Wheeler, J.Z. Zhang, Y. Li, Sn-doped hematite nanostructures for photoelectrochemical water splitting, Nano Lett. 11 (2011) 2119–2125, https://doi.org/10.1021/nl200708y.

[100] S.K. Mohapatra, S.E. John, S. Banerjee, M. Misra, Water photooxidation by smooth and ultrathin α-Fe_2O_3 nanotube arrays, Chem. Mater. 21 (2009) 3048–3055, https://doi.org/10.1021/cm8030208.

[101] P.S. Shinde, G.H. Go, W.J. Lee, Facile growth of hierarchical hematite (α-Fe_2O_3) nanopetals on FTO by pulse reverse electrodeposition for photoelectrochemical water splitting, J. Mater. Chem. 22 (2012) 10469–10471, https://doi.org/10.1039/C2JM31254A.

[102] L. Fu, H. Yu, Y. Li, C. Zhang, X. Wang, Z. Shao, B. Yi, Ethylene glycol adjusted nanorod hematite film for active photoelectrochemical water splitting, Phys. Chem. Chem. Phys. 16 (2014) 4284–4290, https://doi.org/10.1039/C3CP54240H.

[103] D. Wang, G. Chang, Y. Zhang, J. Chao, J. Yang, S. Su, L. Wang, C. Fan, L. Wang, Hierarchical three-dimensional branched hematite nanorod arrays with enhanced mid-visible light absorption for high-efficiency photoelectrochemical water splitting, Nanoscale 8 (2016) 12697–12701, https://doi.org/10.1039/C6NR03855G.

[104] P. Peerakiatkhajohn, J.-H. Yun, H. Chen, M. Lyu, T. Butburee, L. Wang, Stable hematite nanosheet photoanodes for enhanced photoelectrochemical water splitting, Adv. Mater. 28 (2016) 6405–6410, https://doi.org/10.1002/adma.201601525.

[105] K. Sivula, R. Zboril, F.L. Formal, R. Robert, A. Weidenkaff, J. Tucek, J. Frydrych, M. Grätzel, Photoelectrochemical water splitting with mesoporous hematite prepared by a solution-based colloidal approach, J. Am. Chem. Soc. 132 (2010) 7436–7444, https://doi.org/10.1021/ja101564f.

[106] J.Y. Zheng, M.J. Kang, G. Song, S.I. Son, S.P. Suh, C.W. Kim, Y.S. Kang, Morphology evolution of dendritic Fe wire array by electrodeposition, and photoelectrochemical properties of α-Fe_2O_3 dendritic wire array, CrystEngComm 14 (2012) 6957–6961, https://doi.org/10.1039/C2CE26046H.

[107] P.S. Shinde, H.H. Lee, S.Y. Lee, Y.M. Lee, J.S. Jang, PRED treatment mediated stable and efficient water oxidation performance of the Fe_2O_3 nano-coral structure, Nanoscale 7 (2015) 14906–14913, https://doi.org/10.1039/C5NR04475H.

[108] M.T. Mayer, Y. Lin, G. Yuan, D. Wang, Forming heterojunctions at the nanoscale for improved photoelectrochemical water splitting by semiconductor materials: case studies on hematite, Acc. Chem. Res. 46 (2013) 1558–1566, https://doi.org/10.1021/ar300302z.

[109] K.-H. Ye, H. Li, D. Huang, S. Xiao, W. Qiu, M. Li, Y. Hu, W. Mai, H. Ji, S. Yang, Enhancing photoelectrochemical water splitting by combining work function tuning and heterojunction engineering, Nat. Commun. 10 (2019) 3687, https://doi.org/10.1038/s41467-019-11586-y.

[110] Z. Najaf, D.L.T. Nguyen, S.Y. Chae, O.-S. Joo, A.U.H.A. Shah, D.-V.N. Vo, V.-H. Nguyen, Q.V. Le, G. Rahman, Recent trends in development of hematite (α-Fe2O3) as an efficient photoanode for enhancement of photoelectrochemical hydrogen production by solar water splitting, Int. J. Hydrogen Energy 46 (2021) 23334–23357, https://doi.org/10.1016/j.ijhydene.2020.07.111.

[111] S. Hussain, M.M. Tavakoli, A. Waleed, U.S. Virk, S. Yang, A. Waseem, Z. Fan, M.A. Nadeem, Nanotextured Spikes of α-Fe_2O_3/$NiFe_2O_4$ composite for efficient photoelectrochemical oxidation of water, Langmuir 34 (2018) 3555–3564, https://doi.org/10.1021/acs.langmuir.7b02786.

[112] S. Hussain, S. Hussain, A. Waleed, M.M. Tavakoli, Z. Wang, S. Yang, Z. Fan, M.A. Nadeem, Fabrication of $CuFe_2O_4$/α-Fe_2O_3 composite thin films on FTO coated glass and 3-D nanospike structures for efficient photoelectrochemical water splitting, ACS Appl. Mater. Interfaces 8 (2016) 35315–35322, https://doi.org/10.1021/acsami.6b12460.

[113] Q. Liu, F. Cao, F. Wu, W. Tian, L. Li, Interface reacted $ZnFe_2O_4$ on α-Fe_2O_3 nanoarrays for largely improved photoelectrochemical activity, RSC Adv. 5 (2015) 79440–79446, https://doi.org/10.1039/C5RA15596G.

[114] P.I. Kyesmen, N. Nombona, M. Diale, Heterojunction of nanostructured α-Fe_2O_3/CuO for enhancement of photoelectrochemical water splitting, J. Alloys Compd. 863 (2021) 158724, https://doi.org/10.1016/j.jallcom.2021.158724.

[115] L. Zhang, P. Cui, H. Yang, J. Chen, F. Xiao, Y. Guo, Y. Liu, W. Zhang, F. Huo, B. Liu, Metal–organic frameworks as promising photosensitizers for

photoelectrochemical water splitting, Adv. Sci. 3 (2016) 1500243, https://doi.org/10.1002/advs.201500243.
[116] W. Wang, X. Xu, W. Zhou, Z. Shao, Recent progress in metal-organic frameworks for applications in electrocatalytic and photocatalytic water splitting, Adv. Sci. 4 (2017) 1600371, https://doi.org/10.1002/advs.201600371.
[117] J. Wu, P. Huang, H. Fan, G. Wang, W. Liu, Metal–organic framework-derived p-Cu2O/n-Ce-Fe2O3 heterojunction nanorod photoanode coupling with a FeOOH cocatalyst for high-performance photoelectrochemical water oxidation, ACS Appl. Mater. Interfaces 12 (2020) 30304–30312, https://doi.org/10.1021/acsami.0c03929.
[118] G. Kaur, S.A.Khan Divya, V.R. Satsangi, S. Dass, R. Shrivastav, Nano-hetero-structured thin films, ZnO/Ag-(α)Fe2O3, with n/n junction, as efficient photoanode for renewable hydrogen generation via photoelectrochemical water splitting, Renew. Energy 164 (2021) 156–170, https://doi.org/10.1016/j.renene.2020.09.060.
[119] Y.W. Phuan, M.N. Chong, J.D. Ocon, E.S. Chan, A novel ternary nanostructured carbonaceous-metal-semiconductor eRGO/NiO/α-Fe2O3 heterojunction photoanode with enhanced charge transfer properties for photoelectrochemical water splitting, Sol. Energy Mater. Sol. Cells 169 (2017) 236–244, https://doi.org/10.1016/j.solmat.2017.05.028.
[120] W. Yang, R.R. Prabhakar, J. Tan, S.D. Tilley, J. Moon, Strategies for enhancing the photocurrent, photovoltage, and stability of photoelectrodes for photoelectrochemical water splitting, Chem. Soc. Rev. 48 (2019) 4979–5015, https://doi.org/10.1039/C8CS00997J.
[121] S. Zhang, Z. Liu, D. Chen, W. Yan, An efficient hole transfer pathway on hematite integrated by ultrathin Al2O3 interlayer and novel CuCoOx cocatalyst for efficient photoelectrochemical water oxidation, Appl. Catal. B Environ. 277 (2020) 119197, https://doi.org/10.1016/j.apcatb.2020.119197.
[122] D. Chen, Z. Liu, S. Zhang, Enhanced PEC performance of hematite photoanode coupled with bimetallic oxyhydroxide NiFeOOH through a simple electroless method, Appl. Catal. B Environ. 265 (2020) 118580, https://doi.org/10.1016/j.apcatb.2019.118580.
[123] S. Saremi-Yarahmadi, K.G.U. Wijayantha, A.A. Tahir, B. Vaidhyanathan, Nanostructured α-Fe_2O_3 electrodes for solar driven water splitting: effect of doping agents on preparation and performance, J. Phys. Chem. C 113 (2009) 4768–4778, https://doi.org/10.1021/jp808453z.
[124] A.M. Huerta-Flores, G. Chávez-Angulo, O.A. Carrasco-Jaim, L.M. Torres-Martínez, M.A. Garza-Navarro, Enhanced photoelectrochemical water splitting on heterostructured α-Fe2O3-TiO2:x (X = Co, Cu, Bi) photoanodes: role of metal doping on charge carrier dynamics improvement, J. Photochem. Photobiol. Chem. 410 (2021) 113077, https://doi.org/10.1016/j.jphotochem.2020.113077.
[125] N. Duc Quang, P. Cao Van, S. Majumder, J.-R. Jeong, D. Kim, C. Kim, Rational construction of S-doped FeOOH onto Fe_2O_3 nanorods for enhanced water oxidation, J. Colloid Interface Sci. 616 (2022) 749–758, https://doi.org/10.1016/j.jcis.2022.02.117.
[126] N.D. Quang, P.C. Van, D.D. Le, S. Majumder, N.D. Chinh, J.-R. Jeong, C. Kim, D. Kim, Fluorine-surface-modified tin-doped hematite nanorod array photoelectrodes with enhanced water oxidation activity, Appl. Surf. Sci. 558 (2021) 149898, https://doi.org/10.1016/j.apsusc.2021.149898.
[127] Z. Fu, T. Jiang, Z. Liu, D. Wang, L. Wang, T. Xie, Highly photoactive Ti-doped α-Fe2O3 nanorod arrays photoanode prepared by a hydrothermal method for photoelectrochemical water splitting, Electrochim. Acta 129 (2014) 358–363, https://doi.org/10.1016/j.electacta.2014.02.132.
[128] D. Ding, B. Dong, J. Liang, H. Zhou, Y. Pang, S. Ding, Solvothermal-etching process induced Ti-doped Fe_2O_3 thin film with low turn-on voltage for water splitting, ACS Appl. Mater. Interfaces 8 (2016) 24573–24578, https://doi.org/10.1021/acsami.6b06795.
[129] M.H. Lee, J.H. Park, H.S. Han, H.J. Song, I.S. Cho, J.H. Noh, K.S. Hong, Nanostructured Ti-doped hematite (α-Fe2O3) photoanodes for efficient photoelectrochemical water oxidation, Int. J. Hydrogen Energy 39 (2014) 17501–17507, https://doi.org/10.1016/j.ijhydene.2013.10.031.
[130] Z. Liu, Q. Cai, C. Ma, J. Zhang, J. Liu, Photoelectrochemical properties and growth mechanism of varied ZnO nanostructures, New J. Chem. 41 (2017) 7947–7952, https://doi.org/10.1039/C7NJ01725A.
[131] A. Samanta, S. Jana, Ni-, Co-, and Mn-Doped Fe2O3 nano-parallelepipeds for oxygen evolution, ACS Appl. Nano Mater. 4 (2021) 5131–5140, https://doi.org/10.1021/acsanm.1c00581.
[132] J. Cai, S. Li, Z. Li, J. Wang, Y. Ren, G. Qin, Electrodeposition of Sn-doped hollow α-Fe2O3 nanostructures for photoelectrochemical water splitting, J. Alloys Compd. 574 (2013) 421–426, https://doi.org/10.1016/j.jallcom.2013.05.152.
[133] T.T. Hien, N.D. Quang, N.M. Hung, H. Yang, N.D. Chinh, S. Hong, N.M. Hieu, S. Majumder, C. Kim, D. Kim, Sn doping into hematite nanorods for high-performance photoelectrochemical water splitting, J. Electrochem. Soc. 166 (2019) H743, https://doi.org/10.1149/2.0621914jes.
[134] X. Qi, G. She, M. Wang, L. Mu, W. Shi, Electrochemical synthesis of p-type Zn-doped α-Fe2O3 nanotube arrays for photoelectrochemical water splitting, Chem. Commun. 49 (2013) 5742–5744, https://doi.org/10.1039/C3CC40599K.
[135] J. Simfukwe, R.E. Mapasha, A. Braun, M. Diale, Exploring the stability and electronic properties of Zn-doped hematite surfaces for photoelectrochemical water splitting, J. Phys. Chem. Solids 136 (2020) 109159, https://doi.org/10.1016/j.jpcs.2019.109159.
[136] J. Huang, G. Hu, Y. Ding, M. Pang, B. Ma, Mn-doping and NiFe layered double hydroxide coating: effective approaches to enhancing the performance of α-Fe2O3 in photoelectrochemical water oxidation, J. Catal. 340 (2016) 261–269, https://doi.org/10.1016/j.jcat.2016.05.007.
[137] C.V. Reddy, I.N. Reddy, B. Akkinepally, K.R. Reddy, J. Shim, Synthesis and photoelectrochemical water oxidation of (Y, Cu) codoped α-Fe2O3 nanostructure photoanode, J. Alloys Compd. 814 (2020) 152349, https://doi.org/10.1016/j.jallcom.2019.152349.
[138] K. Nagaveni, M.S. Hegde, G. Madras, Structure and photocatalytic activity of Ti1-xMxO2 ± δ (M = W, V, Ce, Zr, Fe, and Cu) synthesized by solution combustion method, J. Phys. Chem. B 108 (2004) 20204–20212, https://doi.org/10.1021/jp047917v.
[139] H. Pan, X. Meng, D. Liu, S. Li, G. Qin, Ti/Zr,N) codoped hematite for enhancing the photoelectrochemical activity of water splitting, Phys. Chem. Chem. Phys. 17 (2015) 22179–22186, https://doi.org/10.1039/C5CP01489A.
[140] Q. Zhu, C. Yu, X. Zhang, Ti, Zn co-doped hematite photoanode for solar driven photoelectrochemical water oxidation, J. Energy Chem. 35 (2019) 30–36, https://doi.org/10.1016/j.jechem.2018.10.012.
[141] H. Zhang, J. Hyun Park, W. Jin Byun, M. Hoon Song, J. Sung Lee, Activating the surface and bulk of hematite photoanodes to improve solar water splitting, Chem. Sci. 10 (2019) 10436–10444, https://doi.org/10.1039/C9SC04110A.
[142] T.K. Sahu, A.K. Shah, A. Banik, M. Qureshi, Enhanced surface and bulk recombination kinetics by virtue of sequential metal and nonmetal incorporation in hematite-based photoanode for superior photoelectrochemical water oxidation, ACS Appl. Energy Mater. 2 (2019) 4325–4334, https://doi.org/10.1021/acsaem.9b00548.
[143] H. Lan, Y. Xia, K. Feng, A. Wei, Z. Kang, J. Zhong, Co-doped carbon layer to lower the onset potential of hematite for solar water oxidation, Appl. Catal. B Environ. 258 (2019) 117962, https://doi.org/10.1016/j.apcatb.2019.117962.
[144] S. Shen, J. Zhou, C.-L. Dong, Y. Hu, E.N. Tseng, P. Guo, L. Guo, S.S. Mao, Surface engineered doping of hematite nanorod arrays for improved photoelectrochemical water splitting, Sci. Rep. 4 (2014) 6627, https://doi.org/10.1038/srep06627.
[145] A. Kushwaha, R.S. Moakhar, G.K.L. Goh, G.K. Dalapati, Morphologically tailored CuO photocathode using aqueous solution technique for enhanced visible light driven water splitting, J. Photochem. Photobiol. Chem. 337 (2017) 54–61, https://doi.org/10.1016/j.jphotochem.2017.01.014.
[146] J. Liu, X. Huang, Y. Li, K.M. Sulieman, X. He, F. Sun, Self-assembled CuO monocrystalline nanoarchitectures with controlled dimensionality and morphology, Cryst. Growth Des. 6 (2006) 1690–1696, https://doi.org/10.1021/cg060198k.
[147] S. Masudy-Panah, R. Siavash Moakhar, C.S. Chua, H.R. Tan, T.I. Wong, D. Chi, G.K. Dalapati, Nanocrystal engineering of sputter-grown CuO photocathode for visible-light-driven electrochemical water splitting, ACS Appl. Mater. Interfaces 8 (2016) 1206–1213, https://doi.org/10.1021/acsami.5b09613.
[148] T.H. Tran, V.T. Nguyen, Copper oxide nanomaterials prepared by solution methods, some properties, and potential applications: a brief review, Int. Sch. Res. Not. (2014) (2014) 1–14, https://doi.org/10.1155/2014/856592.
[149] S. Masudy-Panah, R. Siavash Moakhar, C. Sheng Chua, A. Kushwaha, T. It Wong, G. Kumar Dalapati, Rapid thermal annealing assisted stability and efficiency enhancement in a sputter deposited CuO photocathode, RSC Adv. 6 (2016) 29383–29390, https://doi.org/10.1039/C6RA03383K.
[150] Y.J. Jang, J.-W. Jang, S.H. Choi, J.Y. Kim, J.H. Kim, D.H. Youn, W.Y. Kim, S. Han, J.S. Lee, Tree branch-shaped cupric oxide for highly effective photoelectrochemical water reduction, Nanoscale 7 (2015) 7624–7631, https://doi.org/10.1039/C5NR00208G.
[151] J. Li, X. Jin, R. Li, Y. Zhao, X. Wang, X. Liu, H. Jiao, Copper oxide nanowires for efficient photoelectrochemical water splitting, Appl. Catal. B Environ. 240 (2019) 1–8, https://doi.org/10.1016/j.apcatb.2018.08.070.
[152] A. Jung, S. Cho, W.J. Cho, K.-H. Lee, Morphology-controlled synthesis of CuO nano- and microparticles using microwave irradiation, Korean J. Chem. Eng. 29 (2012) 243–248, https://doi.org/10.1007/s11814-011-0168-4.
[153] Q. Zhang, K. Zhang, D. Xu, G. Yang, H. Huang, F. Nie, C. Liu, S. Yang, CuO nanostructures: synthesis, characterization, growth mechanisms, fundamental properties, and applications, Prog. Mater. Sci. 60 (2014) 208–337, https://doi.org/10.1016/j.pmatsci.2013.09.003.
[154] R. Bagtache, F. Saib, K. Abdmeziem, M. Trari, A new hetero-junction p-CuO/Al_2O_3 for the H2 evolution under visible light, Int. J. Hydrogen Energy 44 (2019) 22419–22424, https://doi.org/10.1016/j.ijhydene.2019.01.109.
[155] Y.-H. Yu, Y.-P. Chen, Z. Cheng, Microwave-assisted synthesis of rod-like CuO/TiO_2 for high-efficiency photocatalytic hydrogen evolution, Int. J. Hydrogen Energy 40 (2015) 15994–16000, https://doi.org/10.1016/j.ijhydene.2015.09.115.
[156] R.S. Moakhar, S.M. Hosseini-Hosseinabad, S. Masudy-Panah, A. Seza, M. Jalali, H. Fallah-Arani, F. Dabir, S. Gholipour, Y. Abdi, M. Bagheri-Hariri, N. Riahi-Noori, Y.-F. Lim, A. Hagfeldt, M. Saliba, Photoelectrochemical water-splitting using CuO-based electrodes for hydrogen production: a review, Adv. Mater. 33 (2021) 2007285, https://doi.org/10.1002/adma.202007285.
[157] S. John, S.C. Roy, CuO/Cu_2O nanoflake/nanowire heterostructure photocathode with enhanced surface area for photoelectrochemical solar energy conversion, Appl. Surf. Sci. 509 (2020) 144703, https://doi.org/10.1016/j.apsusc.2019.144703.
[158] E.L. Tsege, S.K. Cho, L.T. Tufa, V.T. Tran, J. Lee, H.-K. Kim, Y.-H. Hwang, Scalable and inexpensive strategy to fabricate CuO/ZnO nanowire heterojunction for efficient photoinduced water splitting, J. Mater. Sci. 53 (2018) 2725–2734, https://doi.org/10.1007/s10853-017-1711-4.
[159] U. Shaislamov, H. Kim, J.M. Yang, B.L. Yang, $CuO/ZnO/TiO_2$ photocathodes for a self-sustaining photocell: efficient solar energy conversion without external bias and under visible light, Int. J. Hydrog. Energy 45 (2020) 6148–6158, https://doi.org/10.1016/j.ijhydene.2019.12.052.
[160] Q. Zhang, B. Zhai, Z. Lin, X. Zhao, P. Diao, $CuO/CuBi_2O_4$ bilayered

heterojunction as an efficient photocathode for photoelectrochemical hydrogen evolution reaction, Int. J. Hydrogen Energy 46 (2021) 11607–11620, https://doi.org/10.1016/j.ijhydene.2021.01.050.
[161] C.-Y. Chiang, Y. Shin, S. Ehrman, Dopant effects on conductivity in copper oxide photoelectrochemical cells, Appl. Energy 164 (2016) 1039–1042, https://doi.org/10.1016/j.apenergy.2015.01.116.
[162] J. Ha, J. Oh, H. Choi, H. Ryu, W.-J. Lee, J.-S. Bae, Photoelectrochemical properties of Ni-doped CuO nanorods grown using the modified chemical bath deposition method, J. Ind. Eng. Chem. 58 (2018) 38–44, https://doi.org/10.1016/j.jiec.2017.09.004.
[163] J. Oh, H. Ryu, W.-J. Lee, J.-S. Bae, Improved photostability of a CuO photoelectrode with Ni-doped seed layer, Ceram. Int. 44 (2018) 89–95, https://doi.org/10.1016/j.ceramint.2017.09.129.
[164] A.M. Ahmed, E.M. Abdalla, M. Shaban, Simple and low-cost synthesis of Ba-doped CuO thin films for highly efficient solar generation of hydrogen, J. Phys. Chem. C 124 (2020) 22347–22356, https://doi.org/10.1021/acs.jpcc.0c04760.
[165] J. Ma, H. Wei, Y. Liu, X. Ren, Y. Li, F. Wang, X. Han, E. Xu, X. Cao, G. Wang, F. Ren, S. Wei, Application of Co_3O_4-based materials in electrocatalytic hydrogen evolution reaction: a review, Int. J. Hydrogen Energy 45 (2020) 21205–21220, https://doi.org/10.1016/j.ijhydene.2020.05.280.
[166] S. Du, Z. Ren, J. Zhang, J. Wu, W. Xi, J. Zhu, H. Fu, Co_3O_4 nanocrystal ink printed on carbon fiber paper as a large-area electrode for electrochemical water splitting, Chem. Commun. 51 (2015) 8066–8069, https://doi.org/10.1039/C5CC01080B.
[167] G. George, L. Elias, A.C. Hegde, S. Anandhan, Morphological and structural characterisation of sol–gel electrospun Co_3O_4 nanofibres and their electrocatalytic behaviour, RSC Adv. 5 (2015) 40940–40949, https://doi.org/10.1039/C5RA06368J.
[168] H. Zhang, J. Zhang, Y. Li, H. Jiang, H. Jiang, C. Li, Continuous oxygen vacancy engineering of the Co_3O_4 layer for an enhanced alkaline electrocatalytic hydrogen evolution reaction, J. Mater. Chem. A 7 (2019) 13506–13510, https://doi.org/10.1039/C9TA03652K.
[169] R. Li, D. Zhou, J. Luo, W. Xu, J. Li, S. Li, P. Cheng, D. Yuan, The urchin-like sphere arrays Co_3O_4 as a bifunctional catalyst for hydrogen evolution reaction and oxygen evolution reaction, J. Power Sources 341 (2017) 250–256, https://doi.org/10.1016/j.jpowsour.2016.10.096.
[170] J. Du, C. Li, Q. Tang, Oxygen vacancies enriched Co_3O_4 nanoflowers with single layer porous structures for water splitting, Electrochim. Acta 331 (2020) 135456, https://doi.org/10.1016/j.electacta.2019.135456.
[171] Q. Zhou, T.-T. Li, J. Qian, Y. Hu, F. Guo, Y.-Q. Zheng, Self-supported hierarchical CuOx@Co3O4 heterostructures as efficient bifunctional electrocatalysts for water splitting, J. Mater. Chem. A 6 (2018) 14431–14439, https://doi.org/10.1039/C8TA03120G.
[172] A. QayoomMugheri, U.A. AneelaTahira, M. IshaqAbro, S.R. Chaudhry, L. Amaral, Z.H. Ibupoto, Co3O4/NiO bifunctional electrocatalyst for water splitting, Electrochim. Acta 306 (2019) 9–17, https://doi.org/10.1016/j.electacta.2019.03.092.
[173] T.V. Vineesh, A. Sekar, S. Rajappa, S. Pal, S. Alwarappan, T.N. Narayanan, Non-precious metal/metal oxides and nitrogen-doped reduced graphene oxide based alkaline water-electrolysis cell, ChemCatChem 9 (2017) 4295–4300, https://doi.org/10.1002/cctc.201701018.
[174] U.P. Azad, S. Kumar, A.K. Singh, R. Prakash, A.K. Singh, MOF derived Co/C and Co3O4/C polyhedron for hydrogen evolution reaction, AIP Conf. Proc. 2142 (2019) 180006, https://doi.org/10.1063/1.5122629.
[175] L. Chen, X. Xie, T. Su, H. Ji, Z. Qin, Co3O4/CdS p-n heterojunction for enhancing photocatalytic hydrogen production: co-S bond as a bridge for electron transfer, Appl. Surf. Sci. 567 (2021) 150849, https://doi.org/10.1016/j.apsusc.2021.150849.
[176] M. Tahir, N. Mahmood, X. Zhang, T. Mahmood, F.K. Butt, I. Aslam, M. Tanveer, F. Idrees, S. Khalid, I. Shakir, Y. Yan, J. Zou, C. Cao, Y. Hou, Bifunctional catalysts of Co3O4@GCN tubular nanostructured (TNS) hybrids for oxygen and hydrogen evolution reactions, Nano Res. 8 (2015) 3725–3736, https://doi.org/10.1007/s12274-015-0872-1.
[177] H. Begum, S. Jeon, Highly efficient and stable bifunctional electrocatalyst for water splitting on Fe–Co_3O_4/carbon nanotubes, Int. J. Hydrogen Energy 43 (2018) 5522–5529, https://doi.org/10.1016/j.ijhydene.2018.01.053.
[178] A. Tahira, Z.H. Ibupoto, M. Willander, O. Nur, Advanced Co_3O_4–CuO nanocomposite based electrocatalyst for efficient hydrogen evolution reaction in alkaline media, Int. J. Hydrogen Energy 44 (2019) 26148–26157, https://doi.org/10.1016/j.ijhydene.2019.08.120.
[179] C.D. Nguyen, V.-H. Nguyen, P.N.K. Tuyen, L.M.T. Pham, Snowflake Co_3O_4-CuO heteroanode arrays supported on three-dimensional framework for enhanced oxygen evolution, J. Electroanal. Chem. 871 (2020) 114235, https://doi.org/10.1016/j.jelechem.2020.114235.
[180] N.D. Quang, S. Majumder, P.C. Van, J.-R. Jeong, C. Kim, D. Kim, Co_3O_4/reduced graphene oxide/$BiVO_4$ nanorod as high performance photoanode for water oxidation, Electrochim. Acta 364 (2020) 137283, https://doi.org/10.1016/j.electacta.2020.137283.
[181] Z. Wang, H. Liu, R. Ge, X. Ren, J. Ren, D. Yang, L. Zhang, X. Sun, Phosphorus-doped Co_3O_4 nanowire array: a highly efficient bifunctional electrocatalyst for overall water splitting, ACS Catal. 8 (2018) 2236–2241, https://doi.org/10.1021/acscatal.7b03594.
[182] S.V.S. Mers, V. Maruthapandian, V. Ganesh, Highly efficient bifunctional electrocatalyst using structurally architectured N-doped cobalt oxide, ChemistrySelect 3 (2018) 8752–8762, https://doi.org/10.1002/slct.201802126.
[183] S. Xiong, S. Weng, Y. Tang, L. Qian, Y. Xu, X. Li, H. Lin, Y. Xu, Y. Jiao, J. Chen, Mo-doped Co_3O_4 ultrathin nanosheet arrays anchored on nickel foam as a bifunctional electrode for supercapacitor and overall water splitting, J. Colloid Interface Sci. 602 (2021) 355–366, https://doi.org/10.1016/j.jcis.2021.06.019.
[184] L. Li, Q. Xu, Y. Zhang, J. Li, J. Fang, Y. Dai, X. Cheng, Y. You, X. Li, Low Ni-doped Co_3O_4 porous nanoplates for enhanced hydrogen and oxygen evolution reaction, J. Alloys Compd. 823 (2020) 153750, https://doi.org/10.1016/j.jallcom.2020.153750.
[185] Y. Tian, L. Cao, P. Qin, Bimetal–organic framework derived high-valence-state Cu-doped Co_3O_4 porous nanosheet arrays for efficient oxygen evolution and water splitting, ChemCatChem 11 (2019) 4420–4426, https://doi.org/10.1002/cctc.201900834.
[186] X. Zhao, F. Yin, X. He, B. Chen, G. Li, Efficient overall water splitting over a Mo (IV)-doped Co3O4/NC electrocatalyst, Int. J. Hydrogen Energy 46 (2021) 20905–20918, https://doi.org/10.1016/j.ijhydene.2021.03.187.
[187] A. Abdelmoneim, A. Naji, E. Wagenaars, M. Shaban, Outstanding stability and photoelectrochemical catalytic performance of (Fe, Ni) co-doped Co3O4 photoelectrodes for solar hydrogen production, Int. J. Hydrogen Energy 46 (2021) 12915–12935, https://doi.org/10.1016/j.ijhydene.2021.01.113.
[188] X.H. Wang, Chemical characterization of mesoporous material supported ZnO nanoparticles for hydrogen sulfide capture from gas streams, Adv. Mater. Res. 129–131 (2010) 143–148, https://doi.org/10.4028/www.scientific.net/AMR.129-131.143.
[189] S. Zhang, Z. Liu, M. Ruan, Z. Guo, E. L, W. Zhao, D. Zhao, X. Wu, D. Chen, Enhanced piezoelectric-effect-assisted photoelectrochemical performance in ZnO modified with dual cocatalysts, Appl. Catal. B Environ. 262 (2020) 118279, https://doi.org/10.1016/j.apcatb.2019.118279.
[190] S. Zhang, Z. Liu, D. Chen, Z. Guo, M. Ruan, Oxygen vacancies engineering in TiO_2 homojunction/ZnFe-LDH for enhanced photoelectrochemical water oxidation, Chem. Eng. J. 395 (2020) 125101, https://doi.org/10.1016/j.cej.2020.125101.
[191] A. Wolcott, W.A. Smith, T.R. Kuykendall, Y. Zhao, J.Z. Zhang, Photoelectrochemical study of nanostructured ZnO thin films for hydrogen generation from water splitting, Adv. Funct. Mater. 19 (2009) 1849–1856, https://doi.org/10.1002/adfm.200801363.
[192] S. Sohila, R. Rajendran, Z. Yaakob, M.A.M. Teridi, K. Sopian, Photoelectrochemical water splitting performance of flower like ZnO nanostructures synthesized by a novel chemical method, J. Mater. Sci. Mater. Electron. 27 (2016) 2846–2851, https://doi.org/10.1007/s10854-015-4100-2.
[193] R. Gill, S. Ghosh, A. Sharma, D. Kumar, V.-H. Nguyen, D.-V.N. Vo, T.-D. Pham, P. Kumar, Vertically aligned ZnO nanorods for photoelectrochemical water splitting application, Mater. Lett. 277 (2020) 128295, https://doi.org/10.1016/j.matlet.2020.128295.
[194] M. Fu, X. Wang, H. Zhao, D. He, Y. Wang, Synthesis of ZnO inverse opals with high crystalline quality by a three-dimensional colloidal crystal template-assisted hydrothermal method over a seed layer, CrystEngComm 18 (2016) 7780–7786, https://doi.org/10.1039/C6CE01597B.
[195] Q. Li, X. Sun, K. Lozano, Y. Mao, Facile and scalable synthesis of "Caterpillar-like" ZnO nanostructures with enhanced photoelectrochemical water-splitting effect, J. Phys. Chem. C 118 (2014) 13467–13475, https://doi.org/10.1021/jp503155c.
[196] T.-F. Hou, R. Boppella, A. Shanmugasundaram, D.H. Kim, D.-W. Lee, Hierarchically self-assembled ZnO architectures: establishing light trapping networks for effective photoelectrochemical water splitting, Int. J. Hydrogen Energy 42 (2017) 15126–15139, https://doi.org/10.1016/j.ijhydene.2017.04.121.
[197] Z. Li, W. Luo, M. Zhang, J. Feng, Z. Zou, Photoelectrochemical cells for solar hydrogen production: current state of promising photoelectrodes, methods to improve their properties, and outlook, Energy Environ. Sci. 6 (2013) 347–370, https://doi.org/10.1039/C2EE22618A.
[198] Z. Kang, H. Si, S. Zhang, J. Wu, Y. Sun, Q. Liao, Z. Zhang, Y. Zhang, Interface engineering for modulation of charge carrier behavior in ZnO photoelectrochemical water splitting, Adv. Funct. Mater. 29 (2019) 1808032, https://doi.org/10.1002/adfm.201808032.
[199] P. Salvador, Hole diffusion length in n-TiO2 single crystals and sintered electrodes: photoelectrochemical determination and comparative analysis, J. Appl. Phys. 55 (1984) 2977–2985, https://doi.org/10.1063/1.333358.
[200] D. Maity, K. Karmakar, D. Pal, S. Saha, G.G. Khan, K. Mandal, One-dimensional p-ZnCo2O4/n-ZnO nanoheterojunction photoanode enabling photoelectrochemical water splitting, ACS Appl. Energy Mater. 4 (2021) 11599–11608, https://doi.org/10.1021/acsaem.1c02351.
[201] Y. Li, Z. Liu, J. Li, M. Ruan, Z. Guo, An effective strategy of constructing a multi-junction structure by integrating a heterojunction and a homojunction to promote the charge separation and transfer efficiency of WO3, J. Mater. Chem. A 8 (2020) 6256–6267, https://doi.org/10.1039/D0TA00452A.
[202] J. Cai, J. Cao, H. Tao, R. Li, M. Huang, Three-dimensional ZnO@TiO_2 core-shell nanostructures decorated with plasmonic Au nanoparticles for promoting photoelectrochemical water splitting, Int. J. Hydrogen Energy 46 (2021) 36201–36209, https://doi.org/10.1016/j.ijhydene.2021.08.140.
[203] H. Jiang, Y. Chen, L. Li, H. Liu, C. Ren, X. Liu, G. Tian, Hierarchical ZnO nanorod/$ZnFe_2O_4$ nanosheet core/shell nanoarray decorated with PbS quantum dots for efficient photoelectrochemical water splitting, J. Alloys Compd. 828 (2020) 154449, https://doi.org/10.1016/j.jallcom.2020.154449.
[204] M. Lin, W. Wang, Passivation of ZnSe nanoparticles in sandwiched CdSe/ZnSe/ZnO nanotube array photoanode to substantially enhance solar photoelectrochemical water splitting for hydrogen evolution, Colloids Surf. Physicochem. Eng. Asp. 614 (2021) 126206, https://doi.org/10.1016/

j.colsurfa.2021.126206.
[205] L. Li, H. Shi, H. Yu, X. Tan, Y. Wang, S. Ge, A. Wang, K. Cui, L. Zhang, J. Yu, Ultrathin MoSe2 nanosheet anchored CdS-ZnO functional paper chip as a highly efficient tandem Z-scheme heterojunction photoanode for scalable photoelectrochemical water splitting, Appl. Catal. B Environ. 292 (2021) 120184, https://doi.org/10.1016/j.apcatb.2021.120184.
[206] M.D. Sharma, C. Mahala, M. Basu, Sensitization of vertically grown ZnO 2D thin sheets by MoSx for efficient charge separation process towards photoelectrochemical water splitting reaction, Int. J. Hydrog. Energy 45 (2020) 12272–12282, https://doi.org/10.1016/j.ijhydene.2020.02.190.
[207] C. Mahala, M.D. Sharma, M. Basu, ZnO nanosheets decorated with graphite-like carbon nitride quantum dots as photoanodes in photoelectrochemical water splitting, ACS Appl. Nano Mater 3 (2020) 1999–2007, https://doi.org/10.1021/acsanm.0c00081.
[208] Y.-H. Lu, W.-H. Lin, C.-Y. Yang, Y.-H. Chiu, Y.-C. Pu, M.-H. Lee, Y.-C. Tseng, Y.-J. Hsu, A facile green antisolvent approach to Cu^{2+}-doped ZnO nanocrystals with visible-light-responsive photoactivities, Nanoscale 6 (2014) 8796–8803, https://doi.org/10.1039/C4NR01607F.
[209] J. bo Zhong, J. zhang Li, Y. Lu, X. yang He, J. Zeng, W. Hu, Y. cheng Shen, Fabrication of Bi^{3+}-doped ZnO with enhanced photocatalytic performance, Appl. Surf. Sci. 258 (2012) 4929–4933, https://doi.org/10.1016/j.apsusc.2012.01.121.
[210] V. Kumar, M. Gohain, R. Kant, O.M. Ntwaeaborwa, P. Hari, H.C. Swart, V. Dutta, Annealing induced oxygen defects on green sonochemically synthesized ZnO nanoparticles for photoelectrochemical water splitting, ChemistrySelect 3 (2018) 11914–11921, https://doi.org/10.1002/slct.201802668.
[211] J.Z. Zhang, Metal oxide nanomaterials for solar hydrogen generation from photoelectrochemical water splitting, MRS Bull. 36 (2011) 48–55, https://doi.org/10.1557/mrs.2010.9.
[212] T. Majumder, S. Dhar, P. Chakraborty, S.P. Mondal, Growth of carbon-functionalized, carbon-doped ZnO/C core-shell nanorods for photoelectrochemical solar energy conversion, ChemistrySelect 3 (2018) 4082–4094, https://doi.org/10.1002/slct.201702750.
[213] Y.-G. Lin, Y.-K. Hsu, Y.-C. Chen, L.-C. Chen, S.-Y. Chen, K.-H. Chen, Visible-light-driven photocatalytic carbon-doped porous ZnO nanoarchitectures for solar water-splitting, Nanoscale 4 (2012) 6515–6519, https://doi.org/10.1039/C2NR31800H.
[214] S. Wang, X. Zhang, S. Li, Y. Fang, L. Pan, J.-J. Zou, C-doped ZnO ball-in-ball hollow microspheres for efficient photocatalytic and photoelectrochemical applications, J. Hazard. Mater. 331 (2017) 235–245, https://doi.org/10.1016/j.jhazmat.2017.02.049.
[215] F. Wang, J.-H. Seo, Z. Li, A.V. Kvit, Z. Ma, X. Wang, Cl-doped ZnO nanowires with metallic conductivity and their application for high-performance photoelectrochemical electrodes, ACS Appl. Mater. Interfaces 6 (2014) 1288–1293, https://doi.org/10.1021/am405141s.
[216] K. Gautam, I. Singh, P.K. Bhatnagar, K.R. Peta, Role of Cl doping on the growth and relaxation dynamics of ZnO nanorods synthesized by hydrothermal method, Chem. Phys. Lett. 662 (2016) 196–200, https://doi.org/10.1016/j.cplett.2016.09.026.
[217] P. Sahoo, A. Sharma, S. Padhan, G. Udayabhanu, R. Thangavel, UV-assisted water splitting of stable Cl-doped ZnO nanorod photoanodes grown via facile sol-gel hydrothermal technique for enhanced solar energy harvesting applications, Sol. Energy 193 (2019) 148–163, https://doi.org/10.1016/j.solener.2019.09.045.
[218] A. Henni, A. Merrouche, L. Telli, A. Karar, Studies on the structural, morphological, optical and electrical properties of Al-doped ZnO nanorods prepared by electrochemical deposition, J. Electroanal. Chem. 763 (2016) 149–154, https://doi.org/10.1016/j.jelechem.2015.12.037.
[219] Y.-F. Xu, H.-S. Rao, X.-D. Wang, H.-Y. Chen, D.-B. Kuang, C.-Y. Su, In situ formation of zinc ferrite modified Al-doped ZnO nanowire arrays for solar water splitting, J. Mater. Chem. A 4 (2016) 5124–5129, https://doi.org/10.1039/C5TA10563C.
[220] W. Hu, N.D. Quang, S. Majumder, E. Park, D. Kim, H.-S. Choi, H.S. Chang, Efficient photo charge transfer of Al-doped ZnO inverse opal shells in SnS2 photoanodes prepared by atomic layer deposition, J. Alloys Compd. 819 (2020) 153349, https://doi.org/10.1016/j.jallcom.2019.153349.
[221] L. Hao, M.A. Kamboh, Y. Su, L. Wang, M. Zhang, J. Zhang, Q. Wang, Ab initio study of the electronic, optical, and water-splitting properties of Fe-doped ZnO monolayer, Phys. E Low-Dimens. Syst. Nanostruct. 137 (2022) 115059, https://doi.org/10.1016/j.physe.2021.115059.
[222] M. Wang, F. Ren, J. Zhou, G. Cai, L. Cai, Y. Hu, D. Wang, Y. Liu, L. Guo, S. Shen, N doping to ZnO nanorods for photoelectrochemical water splitting under visible light: engineered impurity distribution and terraced band structure, Sci. Rep. 5 (2015) 12925, https://doi.org/10.1038/srep12925.
[223] X. Yang, A. Wolcott, G. Wang, A. Sobo, R.C. Fitzmorris, F. Qian, J.Z. Zhang, Y. Li, Nitrogen-doped ZnO nanowire arrays for photoelectrochemical water splitting, Nano Lett 9 (2009) 2331–2336, https://doi.org/10.1021/nl900772q.
[224] F. Rasouli, A. Rouhollahi, F. Ghahramanifard, Gradient doping of copper in ZnO nanorod photoanode by electrodeposition for enhanced charge separation in photoelectrochemical water splitting, Superlattices Microstruct. 125 (2019) 177–189, https://doi.org/10.1016/j.spmi.2018.08.026.
[225] R. Dom, L.R. Baby, H.G. Kim, P.H. Borse, Enhanced solar photoelectrochemical conversion efficiency of ZnO:Cu electrodes for water-splitting application, Int. J. Photoenergy. 2013 (2013) e928321, https://doi.org/10.1155/2013/928321.
[226] H.Q. Huynh, K.N. Pham, B.T. Phan, C.K. Tran, H. Lee, V.Q. Dang, Enhancing visible-light-driven water splitting of ZnO nanorods by dual synergistic effects of plasmonic Au nanoparticles and Cu dopants, J. Photochem. Photobiol. Chem. 399 (2020) 112639, https://doi.org/10.1016/j.jphotochem.2020.112639.
[227] A.A. Aboud, M. Shaban, N. Revaprasadu, Effect of Cu, Ni and Pb doping on the photo-electrochemical activity of ZnO thin films, RSC Adv. 9 (2019) 7729–7736, https://doi.org/10.1039/C8RA10599E.
[228] L. Cai, F. Ren, M. Wang, G. Cai, Y. Chen, Y. Liu, S. Shen, L. Guo, V ions implanted ZnO nanorod arrays for photoelectrochemical water splitting under visible light, Int. J. Hydrog. Energy 40 (2015) 1394–1401, https://doi.org/10.1016/j.ijhydene.2014.11.114.
[229] A. Sreedhar, I.N. Reddy, Q.T. Hoai Ta, E. Cho, J.-S. Noh, Insight into anions and cations effect on charge carrier generation and transportation of flake-like Co-doped ZnO thin films for stable PEC water splitting activity, J. Electroanal. Chem. 855 (2019) 113583, https://doi.org/10.1016/j.jelechem.2019.113583.
[230] A. Galán-González, A.K. Sivan, J. Hernández-Ferrer, L. Bowen, L. Di Mario, F. Martelli, A.M. Benito, W.K. Maser, M.U. Chaudhry, A. Gallant, D.A. Zeze, D. Atkinson, Cobalt-doped ZnO nanorods coated with nanoscale metal–organic framework shells for water-splitting photoanodes, ACS Appl. Nano Mater. 3 (2020) 7781–7788, https://doi.org/10.1021/acsanm.0c01325.
[231] A. Sreedhar, I.N. Reddy, Q.T. Hoai Ta, G. Namgung, E. Cho, J.-S. Noh, Facile growth of novel morphology correlated Ag/Co-doped ZnO nanowire/flake-like composites for superior photoelectrochemical water splitting activity, Ceram. Int. 45 (2019) 6985–6993, https://doi.org/10.1016/j.ceramint.2018.12.198.
[232] I. Neelakanta Reddy, Ch.V. Reddy, A. Sreedhar, J. Shim, M. Cho, K. Yoo, D. Kim, Structural, optical, and bifunctional applications: supercapacitor and photoelectrochemical water splitting of Ni-doped ZnO nanostructures, J. Electroanal. Chem. 828 (2018) 124–136, https://doi.org/10.1016/j.jelechem.2018.09.048.
[233] P. Sahoo, A. Sharma, S. Padhan, R. Thangavel, Visible light driven photosplitting of water using one dimensional Mg doped ZnO nanorod arrays, Int. J. Hydrogen Energy 45 (2020) 22576–22588, https://doi.org/10.1016/j.ijhydene.2020.06.173.
[234] M. Barroso, C.A. Mesa, S.R. Pendlebury, A.J. Cowan, T. Hisatomi, K. Sivula, M. Grätzel, D.R. Klug, J.R. Durrant, Dynamics of photogenerated holes in surface modified α-Fe_2O_3 photoanodes for solar water splitting, Proc. Natl. Acad. Sci 109 (2012) 15640–15645, https://doi.org/10.1073/pnas.1118326109.
[235] O. Zandi, T.W. Hamann, Determination of photoelectrochemical water oxidation intermediates on haematite electrode surfaces using operando infrared spectroscopy, Nat. Chem. 8 (2016) 778–783, https://doi.org/10.1038/nchem.2557.